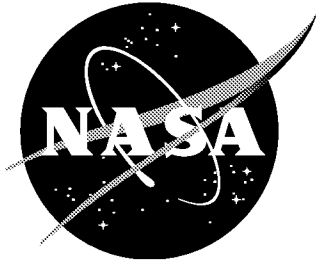NASA/CR-1999-209842

Effects of Jet Swirl on Mixing of a Light Gas Jet in a Supersonic Airstream

Steven E. Doerner and Andrew D. Cutler
Joint Institute for Advancement of Flight Sciences
The George Washington University
Langley Research Center, Hampton, Virginia

The NASA STI Program Office ... in Profile

Since its founding, NASA has been dedicated to the advancement of aeronautics and space science. The NASA Scientific and Technical Information (STI) Program Office plays a key part in helping NASA maintain this important role.

The NASA STI Program Office is operated by Langley Research Center, the lead center for NASA's scientific and technical information. The NASA STI Program Office provides access to the NASA STI Database, the largest collection of aeronautical and space science STI in the world. The Program Office is also NASA's institutional mechanism for disseminating the results of its research and development activities. These results are published by NASA in the NASA STI Report Series, which includes the following report types:

- TECHNICAL PUBLICATION. Reports of completed research or a major significant phase of research that present the results of NASA programs and include extensive data or theoretical analysis. Includes compilations of significant scientific and technical data and information deemed to be of continuing reference value. NASA counterpart of peer-reviewed formal professional papers, but having less stringent limitations on manuscript length and extent of graphic presentations.

- TECHNICAL MEMORANDUM. Scientific and technical findings that are preliminary or of specialized interest, e.g., quick release reports, working papers, and bibliographies that contain minimal annotation. Does not contain extensive analysis.

- CONTRACTOR REPORT. Scientific and technical findings by NASA-sponsored contractors and grantees.
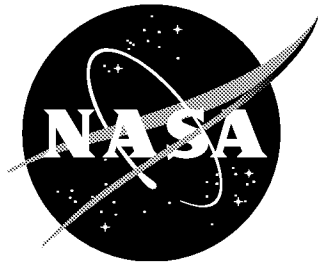
- CONFERENCE PUBLICATION. Collected papers from scientific and technical conferences, symposia, seminars, or other meetings sponsored or co-sponsored by NASA.

- SPECIAL PUBLICATION. Scientific, technical, or historical information from NASA programs, projects, and missions, often concerned with subjects having substantial public interest.

- TECHNICAL TRANSLATION. English-language translations of foreign scientific and technical material pertinent to NASA's mission.

Specialized services that complement the STI Program Office's diverse offerings include creating custom thesauri, building customized databases, organizing and publishing research results ... even providing videos.

For more information about the NASA STI Program Office, see the following:

- Access the NASA STI Program Home Page at *http://www.sti.nasa.gov*

- E-mail your question via the Internet to help@sti.nasa.gov

- Fax your question to the NASA STI Help Desk at (301) 621-0134

- Phone the NASA STI Help Desk at (301) 621-0390

- Write to:
  NASA STI Help Desk
  NASA Center for AeroSpace Information
  7121 Standard Drive
  Hanover, MD 21076-1320

Effects of Jet Swirl on Mixing of a Light Gas Jet in a Supersonic Airstream

Steven E. Doerner and Andrew D. Cutler
Joint Institute for Advancement of Flight Sciences
The George Washington University
Langley Research Center, Hampton, Virginia

December 1999

ABSTRACT

A nonreacting experiment was performed to investigate the effects of jet swirl on mixing of a light gas jet in a supersonic airstream. The experiment consisted essentially of two parts. The first part was an investigation of the effects of jet swirl and skew on the mixing and penetration of a 25° supersonic jet injected from a flat surface (flush wall injection) into a supersonic ducted airflow. Specifically, the objective was to determine whether the jet would mix more rapidly if the jet were swirling, and whether swirl, with and without skew, causes the injectant-air plume to have a net circulation (i.e., a single or dominant vortex). The second part was a preliminary study of the mixing of swirling jets injected from the base of a skewed ramp. The hypothesis was that favorable interactions between vorticity generated by the swirling jet and vortices generated by the ramp can produce mixing enhancements. Both parts of the experiment were conducted at equal injectant mass flow rate and total pressure.

The results for the flush wall injection cases indicate that, except relatively close to the injection point, swirl, with or without skew, does not enhance the mixing of the jet, and can in fact reduce penetration. In addition, a plume with significant net circulation is not generated, as had previously been believed. The results for the ramp cases indicated no improvements in mixing in comparison with the baseline (swept ramp injector) case. However, it was not possible to determine the vorticity mechanisms underlying the poor performance, since no measurements of vorticity were made. Thus, since many geometric parameters were chosen arbitrarily, the results are inconclusive for this class of injector.

TABLE OF CONTENTS

LIST OF SYMBOLS

a	speed of sound
A	area
Cf	flow meter correction factor
c	mass fraction
c_p	specific heat at constant pressure
c_v	specific heat at constant volume
d	nozzle diameter
E	hot-film voltage
f	stoichiometric mass fraction of hydrogen in air for complete reaction of all H_2 and $O_2 \rightarrow H_2O$
h	height of duct interior in y direction; $= 38.61$ mm
K	nozzle coefficient
M	Mach number
$\dot{m}$	mass flow rate
MW	molecular weight
p	pressure
r	radial position
R	gas constant
t	time
T	temperature
U	flow velocity
u	velocity component in the x-direction

V volume

$\dot{V}$ volumetric flow rate

v velocity component in the y-direction

x distance in axial direction

y distance normal to injector wall, measured from this wall

z distance from injector wall centerline, orthogonal to x, y

Z local injectant mass fraction which would react were it H_2

Greek Symbols

α pitch angle of jet

β skew angle of jet

χ mole fraction injectant

δ uncertainty

γ ratio of specific heats

ϕ total angle of jet

Φ equivalence ratio

η mixing efficiency

μ Mach wave angle

ρ density

Subscripts

c	cone static
cm	center of mass
inj	injectant, injection
j	injector jet
pit	pitot
t	total
w	wall
θ	tangential component, tangential direction
∞	freestream

Superscripts

*	choked condition ($M = 1$)
~	mass flux weighted mean
‾	mean
'	fluctuating

Test Cases

N0, N25, S0, S25, S-25, S25X, N0S, N25R, S25R, S-25R

See Table 3-1 for definitions.

1.0   INTRODUCTION

1.1   Motivation

One of America's most ambitious aerospace goals is to have a hypersonic airbreathing space delivery vehicle. Airbreathing propulsion has the potential of offering a significant weight savings over rocket propulsion, because the vehicle does not need to carry oxidizer along with its fuel. This allows for larger aircraft payloads or smaller aircraft than those powered by rocket propulsion. The supersonic combustion ramjet (scramjet) is the engine of choice for proposed hypersonic vehicles. In a scramjet, air remains supersonic as it passes through the combustion chamber, unlike the ramjet, which slows incoming air to subsonic speeds during combustion. In a ramjet combustor, fuel injection schemes, such as multiple inflow injectors and recirculating regions, are used which are optimized for efficient mixing. Losses in total pressure (rises in entropy) associated with such schemes are low due to the low Mach number, contrary to those of a scramjet. Thus, scramjet fuel injection and mixing schemes must be conceived which provide the required degree of fuel mixing while minimizing losses.

Previous studies have indicated that the mixing of an angled (pitched) supersonic jet into a supersonic duct flow is improved by a swirling jet.[1,2] These studies also indicated that a swirling jet acts as a vortex generator, generating an injectant-air plume containing a single or dominant vortex. If it does act as a vortex generator, then there are several additional possibilities for further increasing fuel jet mixing and penetration. Bushnell[3] discusses many of these for application in the hypervelocity flight regime $\left(M \underset{\sim}{>} 10 \right)$, but they are equally relevant for the lower hypersonic flight numbers of M ≈ 6-7 (the flight speeds of interest in this study), where flow speeds in the combustor are M

$\approx$ 2. These include interaction of a counterrotating pair of vortices (with common flow away from the wall) to increase penetration. In the present case, a counterrotating pair of vortex plumes would be interacted, generated by a counterrotating pair of swirling jets. Other interactions might induce instabilities which could enhance turbulent generation and mixing. Favorable effects might also be found by interacting vortices produced by ramps with vortex plumes. Bushnell also noted that skewed wall jets act as vortex generators in subsonic flow and might also be effective in supersonic. In the present context, skewing the swirling jet (in the correct direction) might increase its effectiveness as a vortex generator.

1.2   Background

Scramjet fuel injectors can be loosely organized into three types: (a) flush-wall injectors, in which fuel is injected into the scramjet duct flow from an orifice in the wall and the duct wall shape is not altered (except for the presence of the orifice itself) by the injector; (b) ramp injectors, in which fuel is injected from an orifice at the base or other parts of a protuberance in the wall which has been contoured to improve mixing and/or penetration of the fuel; (c) strut injectors, in which the injector orifice is suspended in the flow away from a wall by a strut. This investigation will focus on flush wall and ramp injectors.

Flush wall injectors depend primarily upon their cross-stream momentum rate to achieve penetration and mixing with the air stream. The pressure felt at the exit of these injectors (the duct wall orifice) is that behind the bow shock formed as a result of the blockage created by the fuel jet as it enters the duct flow. This pressure depends on the

2

angle of the fuel jet to the duct flow. Cases where the pressure at the exit of the injector is matched to the pressure behind the bow shock (assuming that the jet axis is initially aligned with the injector nozzle exit) are called matched pressure. If the injector exit pressure is greater than this matched pressure (underexpanded), the jet turns outwards in relation to the nozzle axis in an expansion turn (Mach number increases), thereby simultaneously raising the pressure behind the bow shock and reducing the pressure in the jet until these are brought into balance. McClinton[4] investigated flush wall injectors at various angles to the flow in a nonreacting experiment. He investigated injectors at 30°, 45°, 60° and 90° to the duct wall, and found the mixing region concentration decay rate was higher for lower injection angles. It is noteworthy, however, that all cases were conducted at a constant total pressure of the jet. Consequently, the lower injection angle jets probably turned outward, as described above, to match the jet pressure with the pressure behind the bow shock. This behavior and its associated systems of shock waves may account for the improved mixing in these low angle cases. Mays, Thomas and Schetz[5] investigated 15° and 30° injection into a supersonic flow with both pressure matched and underexpanded cases. Their conclusions were that the angle of the injector had little effect on penetration and mixing but an under expanded jet produced greater mixing.

Swithenbank and Chigier[6] were early pioneers of the idea of mixing enhancement in a supersonic flow by swirling the fuel jet. Swirl was generated by tangential injection into the plenum and the swirling flow was accelerated in a nozzle. Vortex breakdown occurred in the jet, leading to increased entrainment of air by the jet. In their combustion tests, the combustion intensity was increased indicating a higher mixing efficiency.

Although their tests were mainly subsonic, it was shown that a reverse flow zone could be found in a transonic swirling jet, which suggests that these effects could also be achieved in a supersonic jet.

The flow of supersonic swirling jets in a stagnant atmosphere was further investigated by Cutler, Levey and Kraus.[7,8,9] The jet was created by tangential injection into a swirl chamber and accelerated through a convergent-divergent nozzle. They observed higher peak helix angles than previous studies as well as lower densities and pressures along the jet axis. They found that mixing layer growth rates increased considerably with swirl and when operated overexpanded, unstable shock interactions produced vortex breakdown.

Kraus and Cutler[1,2,10] investigated the effects of swirl on mixing of a 30° flush wall injector into a Mach 2 flow. Two swirling cases and a nonswirling case were investigated which utilized the same convergent-divergent nozzle. For matched exit pressures this led to a higher injectant total pressure and lower mass flow rate with swirl than without. An analysis was performed to bring the results to an equal mass flow rate basis, and suggested that addition of swirl would result in better mixing. Note that the comparison was still on the basis of unequal injectant total pressures. It is possible that if the total pressure of the nonswirling case were raised to make it equal with one of the swirling cases (same mass flow rate and exit pressure), penetration and mixing would be improved. (In practice this would have involved resizing of the convergent-divergent nozzle.) In addition to improvement in mixing, addition of swirl appeared to result in the generation of a dominant vortex, as evidenced by a lateral motion of the injectant plume.

Johnson[11] investigated the possibility of increasing injectant penetration by injection of a pair of counterrotating swirling jets into a Mach 2 airstream. Several injectors were considered, each of which injected nominally the same mass flow rate when operated with the injectant supply at the same pressure. Of primary interest were flush wall and swept ramp injectors utilizing counterrotating pairs of swirling jets pitched at 25° to the main flow. For comparison, flush wall and swept ramp injectors utilizing a single nonswirling jet at 25° and a surface normal flush wall injector were considered. It was found that for both ramp injector cases, downstream penetration was nearly that of the normal injector. The addition of swept ramps had more influence on penetration than addition of swirl and the penetration was less than expected for the swirling jet pair. Mixing performance downstream of the injector exit location was also enhanced by the use of ramps over that of the normal injector and was best for the ramped swirling jet pair. In the case of the flush wall swirling jet pair, a vortex interaction instability occurred which led to the intermittent rotation (by ±180°) of the locations of the vortex centers, such that their mutual interaction caused an intermittently reduced jet penetration.

Streamwise vortices have been generated in low-speed flows by injection of jets from flush wall orifices with jet axes pitched in relation to the wall and skewed to the freestream. Compton and Johnston[12] examined the effects of a wall jet with fixed 45° pitch and skew varying from 0° to 180° in a turbulent boundary layer. They found the pitched and skewed jet produced a longitudinal vortex which was similar to a weak vortex formed by a solid vortex generator. They also found that the maximum vorticity was strongly dependent on the jet velocity and skew angle. Fuller, Mays, Thomas and

Schetz[13] studied the effects of pitched and skewed jets in a supersonic flow. They investigated a Mach 3, 30° pitched jet and a Mach 6, 15° pitched jet at skew angles of 0° to 28°. For the Mach 3, 30° pitch angle case, maximum injectant concentration decay was not increased by skew, and for the Mach 6, 15° pitch angle case, this decay was decreased. The injectant plume cross-section area was increased with skew in both Mach number cases, but penetration and total pressure losses were minimally affected by skew.

Northam, Greenberg and Byington[14] explored the mixing characteristics of swept and unswept ramp injectors in a combustion experiment. They investigated a pair of ramps with parallel injection in a supersonic duct flow with and without added normal injection downstream. For the tested configurations, they found that combustion efficiencies were higher for the swept ramps than for the unswept ramp. Addition of the normal injector downstream of the ramps had no effect on combustion efficiency with the swept ramp but did increase the efficiency with the unswept ramp. Overall, however, the swept ramp with no normal injection provided the best combustion. Stouffer, Baker, Capriotti and Northam[15] investigated the effects of compression versus expansion ramps in a supersonic combustion experiment. A compression ramp protrudes into the main flow producing a shock wave or compression wave at the front of the ramp, whereas, an expansion ramp produces expansion waves where the wall at the root of the ramp tapers away from the flow. At the particular test conditions of this experiment, the fuel reacted immediately downstream of the compression ramp injectors, and, although the fuel from the expansion ramp injectors did not ignite until farther downstream, combustion occurred rapidly indicating a shorter combustor might be necessary using the expansion ramps. Riggins and McClinton[16] computationally compared mixing enhancement of

6

swept and unswept ramp injectors with that of low angle (30°) wall injector. In the nonreacting mixing study, the swept ramp had the highest mixing and the unswept ramp had the lowest with the 30° wall jet having intermediate mixing. In the reacting solutions, the wall jet showed slightly better mixing effectiveness farther downstream but the swept ramp injector had slightly better mixing effectiveness closer to the injector.

1.3   Objectives

This work is in two parts. An objective of the first part is to determine whether 25° supersonic jets from a flat wall (flush wall injector) into a supersonic ducted airflow will mix more rapidly if the jet is swirling, or skewed in relation to the incident airstream. A second objective is to determine whether swirl, with and without skew, causes the injectant plume to have a net circulation (i.e., form a single or dominant vortex), as inferred from large scale motions of the fuel plume. This experiment is conducted at equal injectant mass flow rate and total pressure. Note that flush wall injectors produce no drag. However, jet thrust in the streamwise direction is slightly lower for the swirling jet than for the nonswirling one, and furthermore is lower still with skew. Swirling jet injectors are significantly more complex in their design and manufacture. Therefore, if swirling jet injectors (with or without swirl) are to be employed in a practical combustor they must produce a substantial enhancement in mixing.

The objective of the second part is to conduct a preliminary study of the mixing performance of swirling jets injected (with skew) from the base of a skewed ramp. The hypothesis is that favorable interactions between vorticity generated by the swirling jet and vorticities generated by the ramp can produce mixing enhancements. The basis of

comparison in this case is an unskewed, nonswirling jet injected from the base of a swept ramp. Whilst the swept ramp and the skewed ramp present roughly the same blockage to the flow, it is considered unlikely that they have the same drag. Thus, although, as for the flush wall injector cases, the experiment is conducted at equal injectant mass flow rate and total pressure, the basis for comparison is not entirely equivalent. Note that no measurements of vorticity could be made, which rendered interpretation of the results difficult and the experiment inconclusive.

This paper will describe the facility and then the instrumentation used. The data reduction and analysis techniques and the operating procedure will then be discussed. Finally the results of the experiment and the conclusions will be presented.

2.0   FACILITY AND MODEL

2.1   Test Facility

These experiments were conducted at the Transverse Jet Facility (TJF) in Room 205 of Building 1221C at NASA Langley Research Center. The TJF consisted of a rectangular Mach 2 two-dimensional convergent-divergent nozzle mounted on top of a plenum 400 mm in diameter and 1100 mm tall. A schematic of the facility can be seen in Figure 2-1. The plenum chamber was divided by an acoustical damper and a set of four wire screens for flow conditioning.[17] On top of the nozzle was a constant area rectangular duct with a cross-section measuring 87.88 mm (3.46 inches) by 38.61 mm (1.52 inches) (the dimensions of the nozzle exit). A photo of the duct and nozzle mounted on the TJF is shown in Figure 2-2. The height of the duct was adjustable from 123.83mm (4.875 inches) to 327.03mm (12.875 inches) in increments of 50.80 mm (2.00 inches). A section view of the duct assembly shown in Figure 2-3 includes the Mach 2 nozzle, pressure taps and the placement of the injector assembly. Figure 2-4 shows the other section view of the duct with and without the offset wall (discussed later). The exit of the duct was open to the laboratory and an overhead exhaust duct caught the exit flow. The duct included provisions for a fuel simulant injector in one of the wall plates. Figure 2-5 shows parts used to offset a duct end wall by 23.62 mm (0.93 inch) to a position 20.32 mm (0.80 inch) from the duct centerline. In the offset wall configuration (Figure 2-4(a)) the scoop separates a portion of the airflow such that any shocks created by the impinging wall tip were directed outside of the duct flow.

The $\delta_{0.995}$ boundary layer thickness in the duct model as a function of the streamwise direction x was determined by Quinn[17], who also used this facility, to be

$$\delta_{0.995} = 1.69 + 0.0075 \cdot x$$

where $\delta_{0.995}$ and x are in mm. Quinn used a combination of numerical techniques and a survey of the exit plane, similar to the one described later, to obtain this relation.

The facility also included a bottle trailer to supply the test gas which was helium with 5% oxygen (which will be denoted He/O$_2$). The trailer contained 1700 m^3 of He/O$_2$ gas at a pressure of 18600 kPa. Helium simulated hydrogen well in a nonreacting experiment due to its light molecular weight and inert properties. Because of demands on the facility by other researchers and budgetary constraints, the He/O$_2$ mixture was used instead of pure helium. Also due to these considerations, the amount of this gas that was apportioned to this study was limited. This limitation restricted aspects of the experiment such as the number of cases examined, the number of surveys taken per case and the survey grid spacing.

2.2   Injector Assembly

The injector assembly (Figures 2-6 and 2-7) was designed to inject fuel simulant into the main flow at a pitch angle of $\alpha = 25°$ to wall surface and varying skew angles β of up to $\pm25°$. The skew angle was set by locating the injector nozzle block next to a pin pressed into one of five drilled holes at -25°, -12.5°, 0°, 12.5°, 25°, where (-) indicates the injector is pointed from right to left looking at the interior wall (Figure 2-6), and locking in place with a plate and screws. The assembly is shown in the $\beta = +25°$ position in Figure 2-6. The total injection angle ϕ to the duct axis is given by

$$\phi = \text{acos}(\cos\alpha \cdot \cos\beta) \tag{2.1}$$

and for a maximum skew angle of $\beta = 25°$, $\phi = 34.8°$.

The injector assembly was also designed to provide swirl or no swirl to a supersonic fuel jet and was configured as a flush wall injector and as a ramp injector. Section views showing both configurations can be seen in Figure 2-7. The fuel simulant enters the injector plenum through the plenum cap. A pressure tap (not shown in Figure 2-7) was located in this chamber to monitor fuel simulant total pressure. The fuel simulant passes through holes in the top hat insert and enters the swirl chamber. For the swirling jet cases, the holes are drilled tangentially through the top hat insert (Figure 2-8a), swirling the flow in the counter-clockwise direction (looking downstream along the axial direction of the jet flow) into a swirl chamber. For the nonswirling cases the holes in the top hat insert were drilled radially (Figure 2-8b). The swirl and nonswirl top hat inserts were the same inserts (low swirl and nonswirl, respectively) used in the experiments conducted by Kraus.[10] The swirl chamber was connected to a convergent-divergent nozzle which accelerated the injector flow. Two nozzle inserts were used (Figure 2-9). The first had an exit-to-throat area ratio of 2.0 and an exit diameter of 6.35 mm (0.25 inch) and was used with the swirl top hat insert. This nozzle had the same throat and exit diameters as did the corresponding swirl nozzle used in Kraus' experiment.[10] The second nozzle had an area ratio of 2.3 and an exit diameter of 4.93 mm (0.194 inch) and was used with the nonswirl top hat insert. These nozzles with their associated inserts were designed to provide the same mass flow rate for the same injectant pressure. If a ramp was desired, a different nozzle insert with square ends but the same internal geometry was used. The ramp was secured over the nozzle insert with a screw. Two 10° ramps were used, one unswept and one swept (Figure 2-10). The

11

injector was located in the nozzle block which mated with a specially constructed wall plate which allowed the nozzle block to pivot about the jet exit as previously described.

2.3   Calibration of Injector Nozzles for Mass Flow Rate

Mass flow rate through the injector nozzles (both with and without swirl) was calibrated against the injector plenum pressure ($p_{t,j}$) and the total temperature of the entering gas ($T_{t,j}$). The nozzles were calibrated against an orifice plate (NASA A004433) which itself was calibrated (with air flow) against standards traceable to the National Institute for Standards and Technology. The calibration was performed by passing 6900 kPa nitrogen through the plate, throttling it through a valve and passing it through the injector. The valve setting was adjusted to vary the mass flow rate in the range approximately 0.023-0.104 kg/sec. Nozzle coefficient $\left(K_{N_2} \equiv \dfrac{\dot{m}_j \sqrt{T_{t,j}}}{p_{t,j}} \right)$ and orifice plate Reynolds number (proportional to nozzle Reynolds number) were calculated at each setting. Nozzle coefficients were interpolated at the Reynolds number of the test (computed for the specific gas injected) and then these coefficients were corrected for the injection gas. The corrections were determined by computing the mass flow rate through the nozzle for some specified $p_{t,j}$, $T_{t,j}$ using first N_2 and second the injection gas (air or He/O_2) using the isentropic, quasi-1-D flow calculations described in Section 2.4 and taking the ratio. Thus:

$$K_{He/O_2} = K_{N_2} \times \left(\frac{\dot{m}_{He/O_2 - \text{quasi}-1-\text{D,isentropic}}}{\dot{m}_{N_2 - \text{quasi}-1-\text{D,isentropic}}} \right) \tag{2.2}$$

12

Note that, for He/O_2 injection, in order to match the Reynolds number with the N_2

calibration tests, results at the low N_2 mass flow rate end of the calibration range had to

be used. Unfortunately, the calibration orifice delta pressure measured were at the low

end of the pressure transducer range for these measurements, so the mass flow rates

calculated were relatively less accurate. As a result, the uncertainty in K(He/O_2) was

estimated to be 2-3%. The results of the nozzle calibration are shown in Table 2-1.

2.4   Operating Conditions

The operating conditions for the plenum were set to provide a nominal Mach 2

flow inside the duct. A 3860 kPa air supply from a central compressor station was used

to provide compressed air at a rate of 3.72 kg/s to the plenum. This supply line was

regulated to provide about 1275 kPa in the lower plenum, ahead of the acoustical damper

and screens and 794 kPa (115 psi) ahead of the nozzle. The pressure ahead of the nozzle

was selected as 794 kPa to provide a nominal pressure of one atmosphere at the exit of

the nozzle. This was based on the nozzle design Mach number M_∞ of 2.0. The actual

Mach number was found to be 1.975 ± 0.01 which gives a pressure of 105.5 ± 1.4 kPa

(15.3 ± 0.2 psi) at the nozzle exit. These quantities are summarized in Table 2-1.

The injector was supplied with fuel simulant from one of two sources. One

simulant, air, was supplied at up to 6900 kPa from a central compressor station. The

other, He/O_2, was provided from a bottle trailer as described above. These sources were

regulated to provide an operating pressure at the injector of 4275 kPa (620 psi). This

pressure was used to match the injector exit static pressure to the effective back pressure

of the main duct flow. The effective back pressure is the pressure behind the bow shock

13

in front of the injector jet. This pressure was calculated by Kraus[10] based on the method of Mays et al.[5] by taking 80% of the pressure on the surface of a cone with a semivertex (apex half) angle of 30° in a Mach 2 flow. The effective back pressure was found to be 237 kPa (34 psi) given a main flow pressure of 105.5 kPa (15.3 psi). Even though the pitch angle in the present experiment is 25° and not 30°, the total angle of the jet relative to the duct axis varies from 25° to 33°. Furthermore, in practice, the pressure varies around the circumference of the jet at the nozzle exit, so the concept of an effective back pressure is an approximation only.

The test conditions were established by a series of calculations which assumed isentropic, quasi-1-D flow of a calorically perfect gas. The injector plenum pressure and the injector nozzle exit-to-throat area ratio are known. The injector nozzle exit conditions are needed. For the nonswirling cases, the Mach number can be calculated from the area ratio by

$$\left(\frac{A}{A*}\right)^2 = \frac{1}{M^2}\left[\frac{2}{\gamma+1}\left(1+\frac{\gamma-1}{2}M^2\right)\right]^{\frac{\gamma+1}{\gamma-1}} \tag{2.3}$$

Given the Mach number, the pressure and the temperature of the injector jet is given from the total pressure and temperature by

$$\frac{p_t}{p} = \left(1+\frac{\gamma-1}{2}M^2\right)^{\frac{\gamma}{\gamma-1}} \tag{2.4}$$

$$\frac{T_t}{T} = 1+\frac{\gamma-1}{2}M^2 \tag{2.5}$$

respectively. With these quantities, the speed of sound and the fluid velocity are

$$a = \sqrt{\gamma RT} \tag{2.6}$$

$$u = Ma \tag{2.7}$$

Then the density can also be found by

$$\rho = \frac{p}{RT} \tag{2.8}$$

Finally, the mass flow rate is given by

$$\dot{m} = \rho u A \tag{2.9}$$

These calculations are based on the assumptions of steady, isentropic, quasi-1-D flow in the nozzle. The results of these calculations are shown in Table 2-2.

The above equations, applied to the main duct flow (Table 2-1), were used to calculate quantities that were used to normalize the injector nozzle quantities as in Table 2-2. The main flow velocity u_∞ is used to nondimensionalize the jet velocity u_j. The mass flow rates of the main flow $\dot{m}_\infty$ and the jet mass flow rate $\dot{m}_j$ are also shown.

For the swirling cases, the method described by Levey[9], which accounts for the added tangential velocity component, was used to calculate the injector nozzle exit conditions. This method, as with the nonswirl case, assumes the flow to be steady, isentropic, irrotational, and quasi-1-D (negligible radial velocity component). Additionally, it assumes axisymmetric flow with a line vortex singularity along the axis of the nozzle. Thus the axial velocity component is assumed to be constant at any given streamwise position, whereas the tangential component varies in proportion to $1/r$ (r is the radial position). Equations are derived using conservation of mass and a throat (minimum area) condition. Closure is achieved by equating nozzle mass flow to mass flow through the tangential injection holes into the swirl chamber. The method, which involves some numerical integration, can be used to obtain nozzle and exit axial Mach numbers, and vortex circulation, given specified nozzle throat and exit areas, and tangential injection holes total area and radius. The static pressure and temperature can

be found by the isentropic relationships given in Equations (2.4) and (2.5), respectively.

The results of these calculations are also shown in Table 2-2.

3.0   INSTRUMENTATION

3.1   Pressure and Temperature Measurements

All pressures were measured using strain gage type pressure transducers of various manufacture, including Bell & Howell Company, Teledyne Taber, Dynisco and MB Electronics. The pressure transducers varied in range from 0-34.5 kPa (0-5 psia) to 0-6900 kPa (0-1000 psia). Pressure transducer calibrations were checked before the experiment. Two pressures were applied to each transducer, a typical operating pressure and atmospheric pressure using a Druck DPI-605 pressure calibration reference. Pressure transducer readings were then acquired through the data acquisition system and the calibration slopes and offsets used by the system were modified to give the correct readings. After the experiment, these calibrations were checked again in the same manner. The change in readings from before the experiment was no greater than 0.3%.

To record the pressures along the walls of the duct, the duct walls were fitted with 1.0 mm (0.04 inch) I.D. static pressure taps as shown on Figure 2-3. These taps were connected via 0.015 inch Tygon tubing to a Pressure Systems, Inc. model ESP-32 electronic pressure scanner and model 780B Controller. This system was controlled with a PC using a BASIC program. The pressures could be read at the rate and duration specified by the user.

All temperatures were measured using T type thermocouples. Each thermocouple was connected to an Omega-CJ cold junction compensator as an ice point reference. The bias error inherent in the thermocouple wires was 1°C over the range measured in this experiment.[18] The cold junction compensators were 0.5°C accurate over the range of 15°C to 35°C.

3.2   Flow Field Survey Apparatus

To take measurements in the flow field, four probes were mounted on a rake which was moved over the exit plane of the duct (Figure 3-1). The four probes were a cone static pressure probe, a stagnation temperature probe, a pitot probe, and a gas sampling probe. The data collected from these probes were used to calculate Mach number, static pressure, static temperature, composition, and density of the flow. These calculations are discussed in Section 3.6.

The rake was mounted to a traverse system which could move the rake in the z- and y-directions. Two stepper motor driven linear actuators, one for each direction, were used to sweep the rake. The rake was moved in the z-direction by a Compumotor Plus stepper motor/slide system and in the y-direction by a Klinger Model CD4 stepper motor/slide system. Both of these were controlled by a LabView program (discussed below).[17] This traverse assembly was mounted directly to the side of the duct. The traverse was set up such that the motion of the probes in the y-z plane was parallel to the exit plane of the duct to within 0.13 mm (0.005 inch) (maximum to minimum height). Pitot probe tip height above the exit plane of the duct varied from case to case (see Table 2-4). Motion in the z-direction was parallel to the duct side wall to within 0.13 mm (0.005 inch). Shims were used to ensure these alignment accuracies.

The **cone static probe** consisted of a cone tip of 10° nominal semivertex angle with four 0.25 mm (0.010 inch) holes drilled normal to the cone surface 4.06 mm (0.160 inch) from the tip (Figure 3-2a).[11] The determination of the actual and effective cone probe angle is discussed in Appendix A. The four holes which led to a common chamber

18

were located 90° apart around the cone. The probe was connected to the transducer by 1.5 m of 1.6 mm I.D. stainless steel tubing. This type of probe is sensitive to misalignment; pressure sensed is expected to fall by about 5% at a probe misalignment of 10°. Turbulent flow is expected to act like a fluctuating misalignment and in turbulent flow the probe should read low by as much as the same 5%.[19]

To measure the flow **stagnation temperature**, a type T or copper-constantan thermocouple was used (Figure 3-2b).[11] The actual device used was a fast-response thermal probe, Model 300-D-050-07-T, from the Paul Beckman Company. It consisted of miniature thermocouple junction at the tip of an 0.20 mm (0.008 inch) diameter needle. This needle was inserted into a radiation shield with a 0.76 mm (0.030 inch) I.D. tip and two 0.30 mm (0.012 inch) holes drilled on opposite sides of the probe needle. This type of temperature probe was shown by Cutler and Johnson[19] to read total absolute temperature about 0.7% low, which was considered acceptable without further calibration.

The **pitot probe** was similar in design to Carty's high resolution probe (Figure 3-2c).[20] It also used the tip of a hypodermic needle but with a 0.36 mm (0.014 inch) I.D. and a 0.64 mm (0.025 inch) O.D. The larger tip diameter was used to decrease the response time. This tip was brazed on to the same tapered 2.5 mm (0.10 inch) O.D. probe cone used by Carty. The probe was connected to its transducer by 0.6 m of standard 1.59 mm (1/16 inch) stainless steel tubing with I.D. of 1.0 mm (0.04 inch). This type of probe is relatively insensitive to misalignment, errors being less than 1% for a probe misalignment of up to 10°. Errors in pitot pressure due to turbulent flow were probably less than 1%.[19]

The **gas sampling probe** was the same one used by Johnson.[11] The probe tip had a 0.76 mm (0.030 inch) I.D. which diverges conically to 2.29 mm (0.090 inch) (Figure 3-2d). All tubing following this point was at least 2.29 mm I.D. to keep the flow inside the tubing from becoming choked. For this unchoked condition, a normal shock stands in the diverging passage (is "swallowed") and the entire gas sample then flows to the gas composition analyzing system subsonically. If the flow were choked somewhere downstream of the probe, then the mass flow would be restricted allowing less gas in through the probe tip and causing a normal shock to form in the flow ahead of it. In this case, the lighter component of the gas mixture would be expected to preferentially pass around the probe and the sensor to detect a lower concentration of the lighter component.[21] Swallowing of the bow shock in a Mach 2 flow was shown by Johnson using schlieren flow visualization.[11] The sensitivity of this type of probe to misalignment of 15° or less is small as shown by Ninneman and Ng.[22]

3.3   Gas Composition Analyzer

In order to determine the efficiency of mixing, the mole fraction of helium in the flow was measured. Johnson described a gas composition analyzing device using hot film anemometry to determine the composition of a binary gas mixture.[11] This device with improved design was rebuilt for the current study and its schematic can be seen in Figure 3-3.

The heart of this gas composition analyzer is the hot film anemometer. For a binary gas mixture, the voltage of a hot film is a function of velocity, pressure, temperature, and the mass fraction of one component of the mixture, or

20

$$E = fn(U,p,T,c) \tag{3.1}$$

To determine the gas composition of the binary mixture, E, U, p, and T must be known. With the sonic orifice (Figure 3-3) downstream of the hot film sensor, the Mach number at the sensor becomes a weak function of the gas composition c. The velocity U then becomes

$$U = fn(p,T,c) \tag{3.2}$$

which gives

$$E = fn(p,T,c) \tag{3.3}$$

Then by setting p and T to fixed values, gas composition is a function of hot film voltage only.

The gas sample enters the probe tip and then flows through approximately one meter of 3.25 mm (0.128 inch) I.D. copper tubing before it arrives at the analyzer system. After passing through a bulkhead fitting, the sample passes through 1.8 meters of the same size copper tubing which is submerged in an insulated ice bath to maintain the temperature at approximately 0°C. The actual temperature of the flow in the ice bath was measured to be 0.0±1.0°C which is within the uncertainty of the type-T thermocouple used. The sample then passes into a fitting with 7.49 mm (0.295 inch) I.D. which leads to a tube of the same I.D. discharging to atmosphere. The diameter of this tube is considerably larger than that used by Johnson in order to ensure the pressure at the bleed point, and thus the hot film sensor, was close to atmospheric. This pressure was actually measured to vary less than 0.7 kPa (0.1 psi) from the daily atmospheric pressure. From this fitting, a small amount of the gas sample is pulled by a vacuum pump into a 254 mm (10 inch) long straight steel tube with 2.29 mm (0.090 inch) I.D. The long tube is used to

ensure the flow is fully developed. At the end, the flow passes over a Dantec 55R01 hot film sensor. A sonic orifice was used to constrain the sample flow's velocity over the sensor.

An earlier design of the gas sample analyzer included a thermocouple upstream and one downstream of the bleed point leading to the hot film probe. During testing of the apparatus, the temperature of the two thermocouples did not deviate from 0°C. This indicated that no atmosphere was seeping into the large exhaust tube. Therefore, one thermocouple was removed to simplify the analyzer and the data acquisition system.

The amount of gas entering the probe was calculated from the probe tip area assuming typical flow conditions of $T_{t,\infty} = 298.15K$, $p_\infty = 101.3kPa$, $M_\infty = 1.8$, and gas composition of either pure air or He/O_2. The mass flow rate of the gas passing over the hot film sensor was calculated from the sonic orifice area assuming isentropic flow between the bleed point (at 1 atmosphere) and the orifice. The ratio of these quantities is then taken to get fraction of the total gas sample mass flow which passes over the hot film. Under these conditions, the fraction of the total gas sample mass flow which passes over the hot film is 0.13 for pure air and 0.11 for pure He/O_2.

The mass flow rate of gas entering the probe tip was calculated using

$$\dot{m} = \overline{\rho u} \cdot A \tag{3.4}$$

where A here is the area of the probe tip through which the sample enters, and

$$\overline{\rho u} = \bar{\rho} \, \bar{u} + \overline{\rho' u'} \tag{3.5}$$

The gas analyzer system gives the mass flux weighted time average of mass fraction of He/O_2 in the sample, $\tilde{c}$. In terms of the flow quantities,

22

$$\tilde{c} = \frac{\text{mean He / O}_2 \text{ mass flowrate into analyzer}}{\text{mean total mass flowrate into analyzer}} \qquad (3.6a)$$

$$\tilde{c} = \frac{\overline{\rho u c} \cdot A}{\overline{\rho u} \cdot A} \qquad (3.6b)$$

where c is the instantaneous mass fraction of He/O$_2$ in the flow. Then

$$\tilde{c} = \frac{\overline{\rho u c}}{\overline{\rho u}} = \frac{\overline{\rho u} \, \bar{c} + \overline{(\rho u)' c'}}{\overline{\rho u}} \qquad (3.7)$$

$$\tilde{c} = \bar{c} + \frac{\overline{(\rho u)' c'}}{\overline{\rho u}} \qquad (3.8)$$

where $\bar{c}$ is the mean mass fraction of He/O$_2$ in the flow

$$\bar{c} \equiv \frac{1}{\tau} \int_0^\tau c \cdot dt \quad (\lim \tau \rightarrow \infty) \qquad (3.9)$$

The gas analyzer was calibrated in terms of mole fraction of He/O$_2$ mixture χ; mass fraction can be found from

$$c = \frac{\chi \cdot MW_{\text{He/O}_2}}{\chi \cdot MW_{\text{He/O}_2} + (1 - \chi) \cdot MW_{\text{air}}} \qquad (3.10)$$

where

$$MW_{\text{He/O}_2} = 0.95 MW_{\text{He}} + 0.05 MW_{\text{O}_2} \qquad (3.11)$$

These derivations can be seen in more detail in Cutler and Johnson.[19]

The hot film sensor was connected to DISA Type 55M10 constant temperature anemometer bridge. The overheat ratio is the ratio of the hot film resistance at operating temperature to its resistance at ambient temperature. Previously, the overheat ratio was set to 1.7.[19] For the current work, an overheat ratio of 1.56 was used to maintain the maximum bridge voltage within the 10.0 volt limit of the data acquisition system.

The gas analyzer was calibrated by passing mixtures of He/O_2 and air of known He/O_2 mole fraction through it. The mixtures were formed by combining flows of pure He/O_2 and pure air at a T-junction at which was located a small plenum packed with glass beads to ensure mixing. A Tylan General RO-28 flow meter controller with four FC-280 flow meters, calibrated for O_2, CH_4, Ar and H_2 gases, was used. The O_2 flow meter was used to control and read the flow rate of air and the H_2 flow meter was used for He/O_2. Since for both flow meters a different gas was being used than its calibration gas, the flow rates were corrected for their respective gases using correction factors Cf given by the manufacturer. For example, to convert a flow rate of 30 SLPM (standard liters per minute) of air through the O_2 flow meter, the correction factor for O_2 to N_2 (Cf_{O2}) and for air to N_2 (Cf_{air}) are needed. (Tylan General used N_2 as the reference gas for correction calculations.) The correction factor for O_2 to air would then be

$$Cf_{O_2\text{-air}} = \frac{Cf_{O_2}}{Cf_{air}} = \frac{0.99}{1.00} = 0.99 \tag{3.12}$$

The flow rate of air through the O_2 flow meter is obtained by multiplying the indicated flow rate by $Cf_{O_2\text{-air}}$. The process for He/O_2 through the H_2 flow meter was the same except there was no published correction factor for helium with 5% oxygen mixture. The correction factors for the various gasses for which Tylan General provides data were correlated with γ, as shown in Figure 3.4. Appendix B describes the procedure used to compute the Cf for an unknown gas, namely He/O2. The equation for Cf as a function of γ from this discussion is given as

$$Cf = 3.5 \cdot \left(\frac{\gamma - 1}{\gamma}\right)^{1.04216} \tag{3.13}$$

Using the following equation, γ was calculated for He/O$_2$:

$$\gamma_{He/O_2} \equiv \frac{c_p}{c_v} = \frac{\chi_{He}\left(\dfrac{\gamma_{He}}{\gamma_{He}-1}\right) + (1-\chi_{He})\left(\dfrac{\gamma_{O_2}}{\gamma_{O_2}-1}\right)}{\chi_{He}\left(\dfrac{1}{\gamma_{He}-1}\right) + (1-\chi_{He})\left(\dfrac{1}{\gamma_{O_2}-1}\right)} \qquad (3.14)$$

where $\chi_{He} = 0.95$ in the He/O$_2$ mixture. The Cf was found to be 1.390 at $\gamma = 1.644$. Due to an analysis error made by the He/O$_2$ gas supplier which was discovered midway through the investigation, Cf was calculated for a helium with 5.2% oxygen mixture. The difference in Cf for 5.0% and 5.2% oxygen was less than 0.08%, which is far less than any other error, so this error was ignored.

In order to ensure their consistency, the two flow meters used, O$_2$ and H$_2$ meters, were connected in series and air flowed through them. One was used to control the flow rate while the other was set to wide open and used to read the flow rate. Then the first was set to wide open to read the flow rate and the other was used to control the flow rate. The volumetric flow rates were varied up to 30 SLPM and the readings of the two flow meters were corrected to air and compared to each other. On the basis of these comparisons, small corrections were implemented on the flow meter calibrations and the resulting flow rate measurements were believed to be accurate within ±0.5% of full scale (30 SLPM).

To calibrate the gas analyzer system, the He/O$_2$ concentration in the gas mixture was varied while reading the voltage output of the anemometer bridge. The He/O$_2$ mole fractions were stepped by 0.1 from 0.0 to 1.0 and then from 1.0 to 0.0 while maintaining the total flow rate at a nominally constant rate of 30 SLPM for all readings. During the calibration, the system was allowed to settle for 30-45 seconds before a reading was

taken. After the 22 points were taken, the data were least squares fit to a fourth order polynomial to derive a calibration equation. A typical calibration curve is shown in Figure 3-5 along with its calibration equation, converting voltage to He/O_2 mole fraction.

The uncertainty in He/O_2 mole fraction , assuming that the uncertainty in the individual volumetric flow rates are both ±0.5% of full scale (30 SLPM), is given by

$$\delta\chi = \sqrt{(1-\chi)^2 + \chi^2} \times 0.005 \qquad (3.15)$$

Thus $\delta\chi \gtrsim 0.005$ for all points in the calibration.

The calibrations on the gas analyzer tended to drift slightly; the gas analyzer had to be calibrated frequently. The calibrations were monitored by checking the calibration before and after each survey of the duct flow. The connection to the gas analyzer system could easily be changed from the gas sampling probe to the calibration flow source by simply changing a tube fitting. Immediately before a survey, the flow meters were set for He/O_2 mole fraction χ_{He} equal to 0.0, 0.5 and 1.0 and data acquisition system readings were recorded. If the readings were off by more than 0.2% full scale, then the calibration was deemed invalid and the hot film was calibrated again. If the calibration was off for the check after the survey, then the hot film was calibrated again and the new calibration was used in the data reduction. Generally, the errors due to this drift were below 0.2-0.4%. The total uncertainty is then

$$\delta\chi \approx \sqrt{(0.5\%)^2 + (0.4\%)^2} = 0.64\% \quad \text{or} \quad \pm0.006\text{-}\pm0.007. \quad (3.16)$$

3.4   Data Acquisition System

Each run or survey consisted of the probes making a number of sweeps over the end of the duct for a given case. During each survey, the translation stage motion was

controlled using LabView, a programming environment from National Instruments. The LabView data acquisition program was set up to initialize the translation stage, then take initial zero-flow condition data before operation of the TJF, and then upon pressurizing the plenum the program took measurements as the probes swept across the flow.

A schematic of the data acquisition system is shown in Figure 3-6. All pressure transducers and thermocouples were connected to their own Neff Model 122-123 DC Amplifier for signal conditioning. The outputs of the Neff were connected to a National Instruments (NI) AMUX-64T multiplexer and a PC with an NI AT-MIO-16E-10 analog-to-digital converter. Each Neff was set to a gain of 100 and to filter out signals above 100 Hz. Within the LabView program the signals were rescaled by 1/100. The LabView data acquisition program read all voltages, performed data reduction (converted the voltages to the proper physical quantities), and wrote the data to disk. At each rake position during a sweep, the rake would pause for 0.3 second to allow for time response of the probes. After the pause, the program read all channels 500 times at 2500 Hz, then averaged the readings for each channel. At the end of a sweep, the program saved the data, then moved the rake 0.25 inch in the y-direction and began the next sweep. After the last sweep, the program returned the rake to its initial position and then wrote the data for all sweeps to disk.

3.5   Probe Response Time

To determine the pause prior to data acquisition at each step in a sweep, the response time of the probes was needed. The response time for the temperature probe was close to instantaneous because the thermocouple was directly in the flow. The

27

response times of the pitot and gas sampling probes were determined using the coaxial jet

model designed by Carty.[20] For the pitot probe, only the centerjet was operated, using

air, and for the gas sampling probe both centerjet (with He/O_2 gas) and coflow (air) were

operated.

The pitot probe was set up 0.005 inch above the exit of the center jet nozzle

outside of the flow. The data acquisition system was set to record pitot pressure at a rate

of 1000 Hz for 10 seconds. After starting the flow, data acquisition was started and the

probe was traversed into the jet flow at up to 600 m/s (2000 ft/sec) for 19.1 mm (0.75

inch). The variation of pitot pressure with time during this experiment is shown in Figure

3-7, from which the probe response time was found to be 0.22 second. The response time

for the cone pressure probe was not measured but assumed to be smaller than that of the

pitot probe due to its larger orifice area.

The response time of the gas analyzer system is the total of the time it takes for a

change in sample gas composition at the probe tip to be first sensed by the hot film sensor

plus the time for the hot film to equilibriate. To determine the time to equilibriate, the

gas sampling probe was set up 0.127 mm (0.005 inch) over the exit of the center jet and

in the coflow. The data acquisition system and the probe traverse were set to the same

rates and data was taken the same way as with the pitot probe. The time to equilibriate

was measured at 0.15 second (Figure 3-8). The time for a change in sample gas

composition at the probe tip to be first sensed by the hot film sensor was calculated. The

mass flow rate entering the probe tip was

$$\dot{m} = \overline{\rho u} \cdot A_{probe\,tip} \tag{3.17}$$

This was converted to a volumetric flow rate at 1 atm and 0°C. The time t was found by

$$t = \frac{V_{\text{probe tip to T}}}{\dot{V}_{\text{probe tip}}} + \frac{V_{\text{T to hot film}}}{\dot{V}_{\text{hot film}}} \qquad (3.18)$$

where $V_{\text{probe tip to T}}$ is the volume inside the tubing from the probe tip to the T-fitting,

$V_{\text{T to hot film}}$ is the volume inside the tubing from the T-fitting to the hot film sensor, $\dot{V}_{\text{probe tip}}$

is the volume flow rate through the probe tip and $\dot{V}_{\text{hot film}}$ is the volume flow rate over the

hot film sensor. The typical flow conditions that were used in the calculation were

$T_{t\infty} = 298.15K$, $p_{\infty} = 101.3kPa$, $M_{\infty} = 1.8$, composition either pure air or He/O$_2$. For pure

air the calculated time was 0.19 second, and for He/O$_2$ it was 0.073 second. Then the

maximum response time for the gas sampling probe, the calculated time plus time to

equilibriate, was 0.34 second.

3.6   Probe Data Reduction and Analysis

The raw survey probe data included cone-static pressure p_c, total temperature T_t,

pitot pressure p_{pit}, and He/O$_2$ mole fraction χ. These data can be converted to more

useful values of the flow such as Mach number M, static pressure p, total pressure p_t.

Useful characteristics about each case can also be calculated, such as center of the fuel

plume in the duct, maximum fuel concentration and mixing efficiency. The following

describes the equations used for reducing the raw data.

Since the ratio of specific heats γ is needed to calculate most other quantities, it is

considered first. From the measured χ and

$$\gamma = \frac{\chi \left(\dfrac{\gamma_{\mathrm{He/O_2}}}{\gamma_{\mathrm{He/O_2}} - 1} \right) + (1 - \chi) \left(\dfrac{\gamma_{\mathrm{air}}}{\gamma_{\mathrm{air}} - 1} \right)}{\chi \left(\dfrac{1}{\gamma_{\mathrm{He/O_2}} - 1} \right) + (1 - \chi) \left(\dfrac{1}{\gamma_{\mathrm{air}} - 1} \right)} \tag{3.19}$$

γ for the flow is found. Now the quantities M, p, p_t can be calculated. The Rayleigh pitot

tube formula relates p/p_{pit} to M and γ. This formula assumes a normal shock in front of

the pitot probe tip and is given by

$$\frac{p}{p_{pit}} = \left(\frac{2\gamma}{\gamma+1} M^2 - \frac{\gamma-1}{\gamma+1} \right)^{\frac{1}{\gamma-1}} \left(\frac{\gamma+1}{2} M^2 \right)^{\frac{-\gamma}{\gamma-1}} \tag{3.20}$$

From a numerical solution of the Taylor-McColl problem, a table of values for

$$\frac{p_c}{p} = fn(M, \gamma) \tag{3.21}$$

was constructed for the effective cone angle.[23] The effective cone angle of the probe tip

was determined in conjunction with nozzle exit plane surveys, as described in Appendix

A. Reynolds number effects were incorporated into the effective cone angle. With

Equations 3.20 and 3.21 and the table, M and p could be calculated in an iterative manner

given p_c and p_{pit}. Once M and p were calculated, p_t is given by

$$\frac{p_t}{p} = \left(1 + \frac{\gamma-1}{2} M^2 \right)^{\frac{\gamma}{\gamma-1}} \tag{3.22}$$

The mass fraction of He/O_2 in the flow can be calculated using Equation 3.10. Similarly,

the gas constant R is given by

$$R = \frac{8314.34}{\chi \cdot MW_{He/O_2} + (1 - \chi) \cdot MW_{air}} \left(\frac{J}{kg \cdot K} \right) \tag{3.23}$$

The mass flux ρu can be found by

$$\rho u = pM\sqrt{\frac{\gamma}{RT}} \qquad (3.24)$$

All calculations assume a calorically perfect gas (c_p, c_v constant).

Three integral quantities of interest, the fuel simulant mass flow rate, the mixing efficiency and the fuel plume center of mass, can be found by integrating the probe data over the survey area. Integrations were performed simply by multiplying each data point value of the quantity being integrated by $\Delta y \Delta z$ (the product of the grid spacing in the y and z directions) and then summing over all data points. The fuel simulant mass flow rate $\dot{m}_{j,probe}$ was calculated from

$$\dot{m}_{j,probe} = \int_A \rho u c \, \mathrm{d}A \qquad (3.25)$$

This quantity can be compared with the mass flow rate determined using the calibration of the injector plus pressure measured at the injector plenum, and with the mass flow rate calculated assuming isentropic quasi-1-D flow in the nozzles, as a check of our experimental techniques. The ratios of these mass flow rates normalized to the injector nozzle calibration mass flow rates for the ten cases are shown in Figure 3-9. This plot shows the uncertainty in conservation of mass for this experiment (+2.5% to –7.5%). One cause for this uncertainty is the relatively sparse grid spacing. Other causes include errors in ρ, u, and c (particularly in ρ and u which are not directly measured but are derived quantities based on pitot, cone and gas sampling probe results).

A quantifiable measure of the penetration of the fuel plume into the main flow is given by the location of the center of mass in a cross-section (y-z plane) of the flow

$$y_{cm} = \frac{\int_A \rho u c y \, \mathrm{d}A}{\dot{m}_{j,probe}} \qquad (3.26a)$$

31

$$z_{cm} = \frac{\int_A \rho ucz \, dA}{\dot{m}_{j,probe}}$$
(3.26b)

In a non-reacting simulation of a supersonic combustor, it is useful to know the mixing efficiency of the injection process. This gives an idea of how well the fuel would burn in an actual scramjet combustor in the same pressure field. The mixing efficiency η is the total mass flow rate of fuel which would react assuming steady, isentropic, quasi-1-D flow divided by the total mass flow rate of fuel. This is also given as

$$\eta = \frac{\int \rho u Z \, dA}{\int \rho u c \, dA}$$
(3.27)

Z is the local injectant mass fraction which would react if the injectant were H_2 assuming all H_2 or O_2 is consumed in combustion, producing H_2O. In other words,

$$Z = c \qquad\qquad \text{if} \qquad c \le f \quad (H_2 \text{ lean - all } H_2 \text{ consumed})$$

$$Z = (1-c)\frac{f}{1-f} \qquad \text{if} \qquad c > f \quad (O_2 \text{ lean - all } O_2 \text{ consumed})$$

where f is the stoichiometric mass fraction of hydrogen in air and hydrogen mixture for complete reaction of all H_2 and $O_2 \rightarrow H_2O$, i.e.

$$f = \left. \frac{m_{H_2}}{m_{H_2} + m_{air}} \right|_{stoich.} = 0.02833 \text{ [19]}$$

Uncertainty in η, $\delta\eta$, assuming the uncertainties in the numerator and denominator of Equation 3.27 are uncorrected, can be written as follows.

$$\left(\frac{\delta\eta}{\eta}\right)^2 = \left(\frac{\delta\left(\int \rho u Z dA\right)}{\int \rho u Z dA}\right)^2 + \left(\frac{-\delta\left(\int \rho u c dA\right)}{\int \rho u c dA}\right)^2$$
(3.28)

Assuming first and second terms are roughly equal, and based on the results of Figure 3-9, this gives

$$\frac{\delta\eta}{\eta} \approx \pm 0.05 \cdot \sqrt{2} \qquad (3.29)$$

In fact, it is likely that errors in the numerator and denominator of 3.27, due to errors in ρ, u, and c or the integration procedure, are highly correlated. That is, if the numerator in, say, 5% high, then the denominator is also ~5% high. If perfectly correlated, then $\frac{\delta\eta}{\eta} = 0$. For the current purposes, we shall assume that

$$\frac{\delta\eta}{\eta} \lesssim \pm 0.05 \qquad (3.30)$$

The eqivalence ratio Φ is the ratio of the mass flow rate of H_2 with the mass flow rate of H_2 to completely burn all air with no excess. This relates to f such that

$$\Phi = \frac{\dot{m}_{H_2}}{\dot{m}_{air}\left(\dfrac{f}{1-f}\right)} \qquad (3.31)$$

This results in values for equivalence ratio of $\Phi = 0.3478$ for the swirling jet and $\Phi = 0.3487$ for the nonswirling jet.

3.7   Operating Procedure

Ten cases were investigated in this study, varying swirl, skew angle, duct configuration (duct wall offset or not), and ramp configuration. For each case, three fuel simulant setups were used, He/O_2 injection, air injection and no injection. Table 3-1 shows the ten cases that were examined and their configurations. (Note that the nomenclature used in Table 3-1 will be used throughout this paper to add consistency to

this discussion.) It also shows nominal locations of the probe surveys that were

conducted for each case. Not all of available locations were surveyed for each case to

conserve the expensive He/O$_2$.

The procedure for setting up and running each test included assembly of the duct,

calibration of the gas sampling probe, alignment of the probes over the duct, operation of

the tunnel and data acquisition. Not all of these steps were taken for all test cases, an

example being that for cases where the duct was already assembled to the height of the

test, the duct assembly step was unnecessary. The gas sampling probe calibration

procedure was described in Section 3.3.

Due to the number of cases surveyed, repeated rebuilding of the duct model was

required. Therefore, to ensure the flow integrity inside the duct, procedures were

established so that the rebuilding was done repeatably. The duct was installed to the exit

of the Mach 2 nozzle such that the interior walls lined up with the interior surfaces of the

nozzle. The duct walls were assembled using clamps to make sure each wall joint was

tight and flush. A down-force was applied to the top of the duct with a soft mallet or a

screw jack to ensure that no gaps remained in the wall joints. Aluminum tape was used

to seal potential gaps in the side wall joints. Gasket material was inserted into the "z"

shaped joints of the end wall plates. For each breakdown and assembly of the duct, the

wall plates were assembled in this manner. The reliability of these procedures was tested

using wall static pressure taps. These tests are discussed later and their results are

discussed in Appendix C.

After the duct was assembled the probe traverse system was aligned. Shims were

used to align the probes in the x-z plane and the y-z plane. Play in the mounting holes

allowed for adjustment in the *x-y* plane and adjustment of the height of the probes above the exit plane of the nozzle. The height of the pitot probe was measured over the four corners of the exit plane of the duct to check these planar adjustments. The cone static probe was then aligned manually to the inside corner of the nozzle exit. The stepper motors were turned on and the probes were moved to their initial survey position by the stepper motor controller subroutine on the PC.

Once the facility and the instrumentation hardware were set up, the survey was taken. All pressure transducers were zeroed to the current atmospheric pressure by adjusting the Neff signal conditioners. Table 3-2 shows the grid spacing along with the probe height above duct exit plane for all cases. In general, three surveys were conducted for each case, one each with air, He/O_2 and no injection. For the He/O_2 injection survey, the gas analyzer was calibrated immediately before the survey. The air supply was established and the plenum pressure was increased to the operating conditions. When the pressure became steady at 794 kPa, the injector pressure was increased to operating pressure 4275 kPa. When both pressures became steady, the program was started to run the survey. After the program indicated the last sweep was completed, both air flows were shut down. At the end of the survey, the probe position was checked to ensure proper operation of the stepper motors.

After the flush wall survey runs (N0, N25, S0, S25, S-25), the wall pressure measurement tests were performed. As explained earlier and in Appendix C, these tests helped determine the repeatability of the duct assembly procedure. The ESP system described in Section 3.1 was used to measure the wall static pressures. These tests were performed for the air injection cases without swirl at 0° skew (N0) and with swirl at 25°

skew (S25). The duct was built up to 228.6, 177.8, 127.0 76.2 mm in length for these tests. The same method of building up the duct as mentioned earlier. For the remaining cases (S25X, N0S, N25R, S25R, S-25R) at the 228.6 mm duct length, the ESP system was used to take wall pressure readings during the surveys.

4.0 RESULTS

4.1 Probe Survey Data

Probe surveys were acquired as indicated in Table 3-1. These include, for each case, surveys for air injection and for He/O$_2$ injection. In some cases (those surveyed towards the end of the test series) surveys were also acquired without injection. As discussed previously, gas composition, pitot, total temperature, and cone-static pressure probes were utilized. After data reduction, these yielded such quantities as velocity, density, etc. Because of the large amount of data generated, only data sufficient to address the objectives of this thesis will be presented. These include the gas composition and pitot surveys, and the integral quantities such as plume center of mass, mixing efficiency, and peak He/O$_2$ mole fractions. These data, taken together, allow comparison of the relative penetration and mixing performance of the various geometries. In addition to the probe surveys, wall static pressure distributions were acquired for most of the cases as discussed in Section 3.7. These are not presented, except that comparisons for various buildup heights are presented in Appendix C in order to establish the repeatability of the flow within the duct as a function of buildup height. All pressures and temperatures are referenced to plenum total pressures and temperatures ($p_{t,\infty}$ and $T_{t,\infty}$ respectively). All lengths are referenced to the duct height $h = 38.61$mm. The following is a case by case examination of the He/O$_2$ injection cases.

4.2 Flush Wall Cases

As discussed previously, the first part of this work was to determine whether swirl or skew enhances the mixing of a supersonic jet from a flat surface into a supersonic

37

airstream, or forms a vortex (as inferred from large scale motions of the injectant-air plume). All cases were at equal injectant mass flow rate and total pressure.

4.2.1 Flush Wall, Nonswirl (N0,N25)

The data for the flush wall, nonswirling jet cases, N0 and N25, are shown in Figures 4-1 and 4-2 respectively. For the $0°$ skew case (N0), the He/O_2 mole fractions at $x/h = 0.658$, 3.289 and 5.921 from the injector exit are shown in Figure 4-1(a). For clarity, a close-up of the He/O_2 mole fraction survey at the $x/h = 0.658$ location is shown in Figure 4-1(c). The mole fraction contours (labeled mole f) form a horseshoe shape close to the injector ($x/h = 0.658$). Farther downstream, the contours become more circular in shape as the plume lifts off the wall. The N0 case pitot pressures (labeled ppt/pp) normalized to the plenum total pressure at the same three locations are shown in Figure 4-1(b). For clarity, a close-up of the pitot pressure survey at the $x/h = 0.658$ location is shown in Figure 4-1(d). For this case, the maximum pitot pressure in the jet was 1.539 and the minimum was 0.364. The high pitot pressure region occurs (at $x/h = 0.658$) because the He/O_2 jet has a higher total pressure than the surrounding air stream. The low pitot pressure region occurs (at $x/h = 0.658$) because air expands around the back of the jet and the Mach number is very high, hence the pitot pressure is very low. In addition (and this is particularly the case at the two downstream locations), boundary layer fluid (of low p_t) is entrained (due to vortex action) up between the vortices in the jet plume. For the $25°$ skew case (N25), the He/O_2 mole fractions at $x/h = 3.289$ from the injector exit are shown in Figure 4-2(a) and the pitot pressures are shown in Figure 4-

38

2(b). These two plots show similar flow characteristics as the N0 case with the exception of a lack of left-right symmetry.

The following explanation, as illustrated in Figure 4.3, is offered for the observed results. Distributed streamwise vorticity is generated in the air around the jet as a result of the curved bow shock (and consequent entropy gradients). Appendix D describes bow shock/vorticity generation in more detail. Vortex sheets are also formed at the jet/air interface. Figure 4-3(a) shows these features at the point of injection. Vorticity is known to be conserved as it convects downstream, except that it may diffuse by viscous processes, or that vorticity of either sign (positive or negative) may be generated. Also, longitudinal vortices, such as those created by aircraft wings, are known to persist for a large streamwise distance, once generated. Vorticity interaction can be used to explain the downstream development of the jet and plume. For the N0 (0° skew without swirl) case, the vortex sheets on both sides of the jet roll up into a vortex pair, combining with the air in the surrounding airstream which contains distributed vorticity (Figure 4-3(b)). This forms a plume with an embedded vortex pair (Figure 4-3(c)). It is well known that this type of counterrotating vortex pair is produced from a pitched wall jet injected into a crossflow as observed by Kraus and Cutler,[2] Riggins and McClinton[16] and Zhang and Collins[24]. For the N25 (25° skew) case, the situation is probably very similar with the exception of the strength and location of the distributed vorticity and the lack of left-right symmetry.

4.2.2 Flush Wall, Swirl (S0, S25, S-25)

The data for the flush wall, swirling jet cases, S0, S25 and S-25, are shown in Figures 4-4, 4-5 and 4-6 respectively. For the $0°$ skew case (S0), the He/O_2 mole fractions at the $x/h = 3.289$ and 5.921 locations are shown in Figure 4-4(a). The mole fraction contours show a plume which, for the most part, remains attached to the injection wall. The plume also moves to the right (positive z) and away from the wall. The pitot pressures for the S0 case are shown in Figure 4-4(b). The pitot pressure contours are similar to those for the nonswirling cases in that they also show entrainment of lower pressure boundary layer fluid away from the wall. However, in these swirl cases, the lower pressure region moves to the right as it moves away from the wall. Figure 4-5(a) shows the He/O_2 mole fractions at the $x/h = 0.658$, 3.289 and 5.921 locations for the $25°$ skew case (S25). For clarity, a close-up of the He/O_2 mole fraction survey at the $x/h = 0.658$ location is shown in Figure 4-5(c). These mole fraction contours are similar to those of S0 except they are broader in the y-direction and slightly farther to the right. The contours are also not as closely attached to the injector wall as they are in S0. At the $x/h = 0.658$ location, the main concentration of He/O_2 is attached to the wall at the left. The pitot pressure contours, shown in Figure 4-5(b), also have a broader shape than those of S0 but still have the asymmetrical shape at the $x/h = 0.658$, 3.289 and 5.921 locations. The low pressure boundary layer entrainment region is farther to the right than that of the S0 case. For clarity, a close-up of the pitot pressure survey at the $x/h = 0.658$ location is shown in Figure 4-5(d). At the $x/h = 0.658$ location, a high pressure region resides near the wall with a low pressure region on its right, also near the wall. Another low pressure region, not as low, also resides next to the high pressure area on the side opposite the

wall. For the -25° skew case (S-25), the He/O_2 mole fractions at the $x/h = 3.289$ location are shown in Figure 4-6(a). The mole fraction contours have a similar shape as those of the S0 case except the plume is more closely attached to the wall. The pitot pressure contours, shown in Figure 4-6(b), have a similar shape to those of S0 except the pressures are lower and the contours are slightly farther to the left.

The following explanation, as illustrated in Figure 4-7, is offered for the observed results for the swirling jet cases, and the differences as compared to the nonswirling cases. Due to the presence of jet swirl with counterclockwise rotation, a dominant vortex sheet of clockwise circulation is formed around the right-hand interface of the He/O_2 jet and the main air flow. This can be seen in Figure 4-7(a). This vortex sheet tends to roll up in a clockwise sense, pulling jet fluid over it from left to right as seen in Figure 4-7(b). Farther downstream, an asymmetrically oriented vortex pair is formed from the roll-up of the right hand vortex sheet and merger of the airstream distributed vorticity into right- and left-hand vorticities (Figure 4-7(c)). An isolated counterclockwise vortex is probably not formed as had been believed by Kraus et al.[1,2,10] as described in Chapter 1.

The effect of positive skew (i.e. skewed to the right in the figures) is to increase the circulation in the vortex sheet at the jet-air interface, below and to the right side of the jet, causing the jet to move more to the right in the near field. Skew also increases the circulation of the distributed vorticity in the airstream to the right of the jet which may have the effect farther downstream of lifting the plume farther from the surface. Negative skew has the opposite effect.

4.2.3 Offset Wall (S25X)

It was hypothesized that, if injection with swirl (and skew) produced an injectant-air plume with net circulation (i.e., a vortex), then introduction of a symmetry plane close to the plume (on the up flow side) would result in greater penetration of the plume into the airstream through mutual interaction of the vortex and its image in the plane. In a practical combustor, such a symmetry plane would be achieved with a pair of skewed, swirling jet injectors, with the one injector having equal and opposite rotation and skew to the other. In this experiment, a symmetry plane was approximated by the offset wall. Note however that the previously described results seem to suggest that a strong, dominant vortex is not generated by swirl, and this is confirmed by the results presented in this section.

Figure 4-8 shows the pitot pressure survey of the main flow of the duct with the offset wall without injection at the x/h = 3.289 and 5.921 locations. This plot shows that no major disturbances in the flow are created by the offset wall. The boundary layer on the offset wall, however, is not as large as suggested by the plot. This is an artifact of the greater grid spacing of data points in the z-direction (6.35mm) than in the y-direction (3.81mm).

The He/O_2 mole fractions of the flush wall case with swirl, 25° skew and offset wall (S25X) at x/h = 3.289 and 5.921 from the injector exit are shown in Figure 4-9(a). These plots show virtually the same He/O_2 mole fraction contours compared with the corresponding case without the offset wall, S25. The S25X case pitot pressures at the same locations are shown in Figure 4-9(b). pitot pressures are also similar, except for low pitot pressure areas in the corner at the side wall/offset wall intersection.

4.2.4 Summary

When comparing the nonswirling jet cases with the swirling jet cases, several observations can be made. The He/O_2 mole fractions plots for the 0° skew cases (N0 in Figure 4-1(a) and S0 in Figure 4-4(a)) have only a small difference in plume size and peak He/O_2 concentration. The significant difference between the two is the shape. The same can be said of the skewed cases (N25 in Figure 4-2(a) and S25 in Figure 4-5(a)). This indicates little, if any, advantage in mixing of the swirling jet over the nonswirling jet, with or without skew. Since the stream thrust contribution of the swirling jet is slightly less than that of the nonswirling jet, there appears to be no practical advantage in using a swirling jet over a nonswirling jet. For the swirling 25° skew case (S25) and the case with the offset wall (S25X) the plume penetration and size are the same. If the swirling jet did produce a plume with net circulation, or a dominant vortex, the plume would move away from the injection wall due to the vortex's interaction with its virtual image in the offset wall. The similarity of the S25X and the S25 surveys suggests that the plume does not contain a dominant vortex.

4.3 Ramp Cases

As discussed previously, the second part of this work is a preliminary study to investigate whether injection of a swirling jet from the base of a skewed ramp produces significant mixing improvement, perhaps due to interactions with ramp induced vorticity. The results are necessarily inconclusive, since comparisons with the baseline swept ramp case were probably not at equal ramp drag.

4.3.1 Swept Ramp, Nonswirl, No Skew (N0S)

The data for the swept ramp, nonswirling jet case, N0S, are shown in Figures 4-10 and 4-11. The pitot pressure contours with no injection are shown in Figure 4-10. This plot shows a low pressure zone that moves away from the injection wall as it moves farther downstream from the ramp. Similar to previous cases where the plume entrained some boundary layer fluid, this low pressure zone also appears to be entraining boundary layer fluid at the $x/h = 3.289$ location. With injection, the He/O_2 mole fraction contours in Figure 4-11(a) have a horseshoe shape that continues, to a lesser degree, to the $x/h = 5.921$ location. At the $x/h = 5.921$ mm location, the plume is detached from the injector wall and is approaching the opposite wall. The pitot pressure contours with injection, shown in Figure 4-11(b), are similar to those with no injection except that there are two centers of lower pressure within the low pressure zone indicating a vortex pair.

The penetration of the injectant plume is the best of all the cases. This is presumably due to the existence of a stronger vortex pair than the other cases. The ramp alone acts as a vortex generator due to the separation of the boundary layer at the swept corners, and the roll up of this feeding vortex sheet just downstream of these corners. By comparison of the pitot pressure distributions with (Figure 4-11(b)) and without (Figure 4-10) injection, it may be inferred that fuel injection increases the vortex pair strength. This is because, while the ramp angle to the wall surface is only 10°, the jet injection angle is 25°, so the jet is not entirely obscured from the main flow by the ramp. Rather, the jet generates vorticity in its own right, as discussed previously and shown in Figure 4-

3. This vorticity combines with the vortices generated by the ramp, strengthening them both.

4.3.2 Skewed Ramp (N25R, S25R, S-25R)

The skewed ramp is expected to generate a longitudinal, counterclockwise rotating (as viewed in the figures) streamwise vortex due to separation of the boundary layer at the downstream swept corner and the rollup of the feeding vortex sheet. It may also create a second counterclockwise rotating vortex due to separation of the boundary layer ahead of the upstream swept corner. These cases utilized the offset wall to provide a symmetry plane near the ramp. It was believed that these types of ramps should be operated in oppositely oriented pairs to provide greater penetration through mutual vortex interaction. The plot of pitot pressure for the case without injection in Figure 4-12 shows significant deficits in the wake downstream of the ramp, and at the offset wall (especially towards the bottom). These deficits probably have associated with them counterclockwise rotating vorticity. (Note that data without injection was acquired for all three skewed ramp cases. The results were almost identical, indicating the geometric repeatability of the setup, even for the mirror image geometry used for the $-25°$ skewed case. Therefore, only one plot is shown here.)

The trajectory of the He/O$_2$ plume with injection depends strongly upon whether or not the jet is swirled. Without swirl, with skew angle 25° (N25R) the plume, which is shown in Figure 4-13(a), lies above the (vortical) wake downstream of the ramp. It appears from the development between the $x/h = 3.289$ and 5.921 downstream locations that the plume is being wrapped around and into the vortical region created by the ramp,

leading to stretching of the He/O$_2$ plume (which it is conjectured will enhance mixing due to increase of the plume/air interfacial area). The pitot pressure distribution for this case, shown in Figure 4-13(b), is similar to that of the case without injection, although the pitot pressure deficit downstream of the ramp is a little greater, and the region of deficit displaced a little farther from the injection wall.

With swirl and skewed 25° (S25R) the plume shown in Figure 4-14(a) appears to be merged with the wake downstream of the ramps, and mixing and penetration are consequently less at $x/h = 5.921$ than with no swirl (N25R). Similar results are obtained with the ramp and jet skewed –25° (S-25R) as seen in Figure 4-15(a). In Figure 4-15(a), the data have been reflected about $z = 0$ giving an impression of negative (clockwise) swirl and +25° skew. Thus, the sense of rotation of the jet swirl seems to be unimportant. The pitot pressure distributions for these cases (Figure 4-14(b) for S25R, Figure 4-15(b) for S-25R) are similar to those without swirl, although at the $x/h = 3.289$ location the wake of the ramp appears to be flatter in shape, and lies closer to the injection wall in the S-25R case.

When comparing the pitot pressure surveys of the swept ramp case with the skewed ramp cases, the pressures downstream of the skewed ramp were lower than those of the swept ramp for both cases with and without injection. This suggests that the skewed ramp produces more drag than the swept ramp. However, since no drag measurements were take, this cannot be quantified. Since the skewed ramp cases did not have better mixing than the swept ramp and the skewed ramp appeared to have higher drag, the swept ramp is probably the better practical injector of the ramp cases.

4.4   Integral Quantities

The previously described integral quantities can be used to compare the different cases directly. The derivations for these quantities are shown in Section 3.6. One such useful comparison, shown in Figure 4-16, is of the motion of the location of the center of mass of the plume (z_{cm}/h, y_{cm}/h), i.e., penetration and lateral movement of the injectant jet into the main flow. From the plot, several observations can be made. The effect of skewing the nonswirling (straight) jet +25° (N0 → N25) is to shift the plume center to the right ($z_{cm}/h > 0$), but there is no significant reduction of height (y_{cm}/h). The effect of swirling the jet (without skewing) (N0 → S0 and N25 → S25) is to shift the plume center to the right and reduce height. The effect of skewing the swirling jet +25° (S0 → S25) is to shift the plume center to the right and increase the height slightly (but not back to the level for the straight, 0° skew case). The effect of skewing the swirling jet -25° (S0 → S-25) is the opposite. The effect of the offset wall on the swirling jet, 25° skew (S25 → S25X), is negligible. The swept ramp case (N0S) had the greatest height at the $x/h =$ 5.921 location, and at $x/h = 3.289$ exceeded all the flush wall jet cases at $x/h = 5.921$. The height for the skewed ramp, nonswirl case (N25R) was the greatest of all cases at x/h = 3.289, but at $x/h = 5.921$ was less than the swept ramp case (N0S). For the N25R case, between $x/h = 3.289$ and 5.921, the plume center moved to the left as the plume began to be wrapped around the ramp generated vortex. The heights for the skewed ramp cases with swirl (S25R, S-25R) are very similar for +25° and -25° skew, and comparable to the flush wall cases (N0, N25, S0, S25, S-25, S25X), but less than the skewed ramp without swirl (N25R).

47

Lateral movements of the plume in the swirling jet cases are much less than might be expected if these jets generated single isolated vortices with the same circulation as that of the jet flows at the nozzle exit. The lateral movement of such a vortex Δz at a height y above the injection surface in a streamwise distance Δx due to the influence of the image of the vortex in the surface plane is

$$\Delta z = \Delta x \left(\frac{v_{\theta j}}{u_\infty} \right) \left(\frac{d/2}{2y} \right) \tag{4.1}$$

where d_e is the nozzle exit diameter. Using the results from Table 2-2, and assuming y is 10.16 mm (0.4 inch)

$$\Delta z = \Delta x \tan(15.49)(2.364) \left(\frac{0.25 inch}{4 \cdot 0.4 inch} \right) \tag{4.2}$$

$$\Delta z = 0.102 \cdot \Delta x \tag{4.3}$$

Thus, for $\Delta x = 25.4$ mm, 127.0 mm, 228.6 mm, this would be about 2.59 mm, 12.95 mm, 23.32 mm (0.10, 0.51, 0.92 inch) respectively. Except at the $x/h = 0.658$ location, these calculated movements are much greater than the observed lateral movements of the plume.

One measure of mixing effectiveness is the peak He/O_2 concentration in the flow. Figure 4-17 shows the peak He/O_2 mole fractions measured for all cases. It should be noted, in interpreting these results, that uncertainties in χ_{max} may be of order ±5-10% of χ_{max}, arising due to the relatively sparse data grid and the fact that grid points may not lie precisely at the maximum. The skewed ramp cases with swirl (S25R, S-25R) have significantly higher peak mole fraction He/O_2, indicating poorer mixing. At $x/h = 3.289$ from the injector exit, the N0S case had the lowest maximum He/O_2 mole fraction at 0.404, but at $x/h = 5.921$, there appears to be little significant difference between the N0,

48

S0, S25, N0S, and N25R cases. The skewed ramp case without swirl (N25R) case has the greatest change in He/O_2 peak mole fraction from x/h = 3.289 to x/h = 5.921 (i.e., peak slope magnitude), which suggests that this case might provide the best mixing downstream of the x/h = 5.921 location.

Figure 4-18 shows a plot of the mixing efficiency for all cases. As discussed in Section 3.6, uncertainties in η are believed to be less than $\pm 0.05\eta$. It is clear from the plot that the swept ramp case (N0S) has the best mixing efficiency at both x/h = 3.289 to x/h = 5.921. However, the mixing efficiency for the flush wall case without swirl and skew (N0), and the skewed ramp case without swirl (N25R) appear to be approaching the mixing efficiency for the swept ramp case at x/h = 5.921, and may equal it further downstream. The mixing efficiency for all the swirling cases is lower than the non-swirling cases at x/h = 3.289 to x/h = 5.921. However, it is higher for the swirling 25° skewed flush wall case (S25) than for the unskewed, nonswirl flush wall case (N0) at x/h = 0.658. The implication is that mixing enhancement due to swirl, predicted by previous experiments (References 3-6), exists in the near field of the injector, but does not persist very far downstream – at least in the current downstream angled wall jet configuration.

5.0   CONCLUSION

This experiment investigated the effects of swirl on the mixing of a supersonic jet of a 5% oxygen in helium (He/O_2) mixture injected into a ducted supersonic flow. The jet was generated by a convergent-divergent nozzle in the wall of the duct, with axis at 25° to the wall. The nozzle could be rotated in a plug about an axis normal to the wall to vary the jet skew from –25° to 0° to +25° with respect to the downstream direction. For the swirling jet cases, swirl was produced in the injector by tangential injection into a swirl chamber ahead of the nozzle. The injectors were modified so that injection took place from the base of a ramp (swept or unswept). Thus, two categories of injector were studied: those without ramps (flush or flat wall) and those with. Nozzle exit pressure was nominally the same for all cases and was nominally matched to the pressure behind the bow shock generated by the jet in the main flow. By use of different nozzle contours for the swirl and nonswirl cases, the same jet mass flow was provided at the same injectant total pressure for all cases.

The flow measurements were taken by sweeping four probes mounted on a computer operated traverse system across the exit of the duct. The four quantities that were measured by the probes were cone static pressure, stagnation temperature, pitot pressure, and gas composition. Wall static pressures were also measured to ensure the quality of the duct flow from test to test. Surveys were conducted at $x/h = 3.289$ and 5.921 downstream from the injector nozzle exit for most cases and additionally at $x/h = 0.658$ for two cases. The data from the surveys were plotted with only the He/O_2 mole fractions and the pitot pressures being shown for this discussion. For direct comparison

of all cases, the data was also reduced to useful integral quantities such as the plume center of mass, the peak He/O_2 concentration, and mixing efficiency.

The results for the flush wall cases indicate that, except relatively close to the injection point, swirl, with or without skew, does not enhance the mixing and penetration of the jet, but in fact reduces it. It is likely that swirl disrupts or alters the rollup process of the counterrotating vortex pair typically created by flush wall injectors, a process which appears to be critical in determining mixing and penetration. On the other hand, injection of a swirling jet into a supersonic airstream does not appear to create a plume with net circulation (i.e., a single or dominant vortex) as had previously been believed. The effects of skew on the jet plume were relatively small for the nonswirl case, but were larger for the swirling case, with skew in the "positive" direction improving penetration. The results for the ramp cases indicate that skewed ramps with swirl do not provide good mixing. However, the results are relatively inconclusive in that it was not possible to offer an adequate explanation for the results. It may be, with better understanding, that a ramp injector incorporating jet swirl could be designed which does provide improved mixing. Direct measurements of vorticity (and also ramp drag) would have greatly helped in the interpretation of these results.

APPENDIX A

Exit Plane Survey

A survey was performed at the exit plane of the Mach 2 nozzle in order to check

for potential nonuniformities in the main duct flow and to check the effective cone angle

on the cone pressure probe. The pitot pressures of the exit survey are shown in Figure A-

1 (the data in each survey are shifted vertically by ¼ times the respective z/h). The pitot

pressures are quite uniform over the nozzle exit. The slight waviness in p_{pit} in the

freestream is not instrumentation error, and to some degree repeats from survey to

survey, indicating the presence of weak 2-D waves in the Mach 2 nozzle. Other than this

slight waviness, the pitot pressure is very uniform, indicating nearly constant Mach

number. The cone static pressures of the exit survey are shown in Figure A-2 (the data in

each survey are shifted vertically by 1/15 times the respective z/h). The cone probe

pressure is uniform within about 5.59 mm (0.22 inch) from the walls (which are located

at $y/h = 0$ and $y/h = 1.0$). Small increases in cone pressure between 5.08-5.59 mm (0.20-

0.22 inch) from the walls may be attributed to weak shock/expansion waves which

emanate from the exit (corners) of the nozzle, and intersect the sensing static taps of the

probe at these locations. For a nozzle exit Mach number of about 2, the Mach wave

angle is given by

$$\mu = \sin^{-1}\left(\frac{1}{M_\infty}\right)$$
(A.1)

So, for a nozzle exit Mach number of about 2.0, μ would be 30°. The length of the probe

from tip to sensing port is 4.064·cos10° mm (0.160·cos10° inch). At the plane of the

probe tip, the distance from the probe tip that the Mach wave would be sensed would be

(4.064·cos10°)·tan30° mm or 2.311 mm. Therefore, the pitot probe will sense the wave

2.31 mm closer to the wall than the cone probe, i.e. at 5.59 − 2.31 = 3.28 mm from the

wall. Thus, the pitot measurements within 3.28 mm (0.13 inch) of the wall are also

influenced by the weak shock/expansion waves from the nozzle exit corners and do not

represent undisturbed boundary layer. Note that probe surveys at the $x/h = 0.658$, 3.289

and 5.921 locations were performed with probe tips closer to the surface, 0.33-0.71 mm

(0.013-0.028 inch) versus 2.64-2.82 mm (0.104-0.111 inch) at the exit plane, and so

suffer less from this problem. From the data taken from this survey, the effective cone

probe angle and Mach number could be inferred. Typically, cone pressure, p_c, and pitot

pressure, p_{pit}, along with the specific heat ratio γ and the cone angle, are use to calculate

the Mach number, total pressure and static pressure (discussed in Section 3.6). To

determine the effective cone angle, an iterative process is used. First, iterate on M_∞,

computing $p_{pit}/p_{t,\infty}$ each time using the equation for total pressure ratios across a normal

shock (at M_∞), until the computed $p_{pit}/p_{t,\infty}$ equals the experimental value. The nozzle is

assumed to be isentropic, so that the local and plenum total pressures are equal. Next,

given M_∞, iterate on cone angle, computing $p_c/p_{t,\infty}$ by solution of the Taylor-MacColl

problem until the computed $p_c/p_{t,\infty}$ equals the measured value (see Section 3.6). The cone

probe was damaged during the experiment so a new one was constructed to finish the

remaining surveys. The exit plane survey performed before the duct surveys is valid for

the first cone probe. The exit plane survey performed at the end of the experiment is

valid for the second cone probe. Analysis of the two exit surveys yielded a cone angle of

10.04° for the first cone probe and 10.15° for the second probe. The exit Mach number

was determined to be 1.975 ± 0.01.

APPENDIX B

Tylan General RO-28 Correction Factor

Since He/O_2 is such an unusual gas, the Tylan General RO-28 flow meter

correction factor Cf for the test gas He/O_2 has not been measured and therefore needs to

be calculated. The process to compute this factor for an unknown gas is described below

using He/O_2 as an example. The response of the flow meter is related to the heat transfer

of a hot wire or hot film element in the flow meter

$$\frac{flow\ meter}{response} \propto \dot{q}$$

which can be written as

$$\frac{flow\ meter}{response} \propto \rho u A c_p (\Delta T) \propto \rho \dot{V} c_p (\Delta T)$$

where

$$\rho = \frac{p}{RT} \qquad \text{and} \qquad \frac{c_p}{R} = \frac{\gamma}{\gamma - 1}$$

The quantities p, T, ΔT are fixed by the design of the controller.

For a given flow meter response, i.e. He/O_2 versus N_2:

$$\left(\rho \dot{V} c_p \right)_{He/O_2} = \left(\rho \dot{V} c_p \right)_{N_2}$$

$$Cf = \left(\frac{\dot{V}_{He/O_2}}{\dot{V}_{N_2}} \right) = \frac{\left(\rho c_p \right)_{N_2}}{\left(\rho c_p \right)_{He/O_2}} = \frac{\dfrac{1}{R_{N_2}} \cdot \left(\dfrac{\gamma R}{\gamma - 1} \right)_{N_2}}{\dfrac{1}{R_{He/O_2}} \cdot \left(\dfrac{\gamma R}{\gamma - 1} \right)_{He/O_2}} = \frac{\left(\dfrac{\gamma}{\gamma - 1} \right)_{N_2}}{\left(\dfrac{\gamma}{\gamma - 1} \right)_{He/O_2}}$$

$$Cf = 3.5 \cdot \left(\frac{\gamma - 1}{\gamma} \right)^1_{He/O_2}$$

This gives *Cf* as a function of only γ. To make the curve fit the experimental value for

helium, the exponent 1 was modified to 1.04216. This brought the correction factor

equation to

$$Cf = 3.5 \cdot \left(\frac{\gamma - 1}{\gamma} \right)_{He/O_2}^{1.04216}$$

or, in more general terms

$$Cf = 3.5 \cdot \left(\frac{\gamma - 1}{\gamma} \right)^{1.04216}$$

APPENDIX C

Duct Breakdown

Wall pressure readings were taken for all duct wall height configurations to determine if the different configurations affected the flow in the duct. Two cases were run with air injected into the flow to investigate the effect of duct breakdown and buildup on the duct flow. The nonswirl, 0° skew case is shown in Figure C-1 and the swirl, 25° skew case is shown in Figure C-2. The point of these plots is to show the repeatability of the flow within the duct as a function of duct height. In particular, they should show whether there are any major influences of the exit plane which propagate upstream into the duct. Such influences would have to take the form of recirculation zones, since in supersonic flows and attached boundary layers, influences propagate downstream only. The plots show fair repeatability for different duct heights, with no inconsistently large variations at the duct exit [which, of course is at a different location for each data set]. The variations that are observed might be attributed to changes in step height or gap width of the joints in the model walls. The uncertainty in $p_w/p_{t,\infty}$ as a consequence of this appears to be ±0.02.

Also of importance is the influence the presence of the survey probes has on the duct flow. Figure C-3 shows the pressure measured at the downstream most wall taps during several surveys as the probes swept back and forth across the duct exit. This figure shows that the probes had no influence on the wall tap measurements and thus no influence on the flow in the duct.

APPENDIX D

Streamwise Vorticity Generation by Bow Shock

The problem of the bow shock generated by an angled jet injected from a flat surface is difficult; therefore consider first the problem of the 2-D flow around a cylinder mounted normal to a supersonic flow. A curved shock is generated ahead of this body. Streamlines passing through the shock near the symmetry plane (where the shock is normal to the flow) suffer a larger loss of total pressure than those passing farther from the symmetry plane. Thus there is vorticity of both signs behind the shock, with direction normal to the plane of the flow (and parallel to the cylinder) (Crocco's theorem). Suppose now that a uniform velocity component is added to the flow parallel to the axis of the cylinder; this represents a simple change of reference frame. The resulting flow may be regarded as the flow around an infinite cylinder whose axis is swept with respect to the oncoming flow. The vorticity behind the bow shock now has a non-zero component parallel to the resultant velocity vector, which is thus "streamwise" vorticity. The bow shock generated by an angled jet is both curved and swept like that of the infinite swept cylinder, and therefore is expected to generate distributed streamwise vorticity of both signs in the airstream in the same manner.

REFERENCES

[1]Kraus, D. K., Cutler, A. D., "Mixing Enhancement by Use of Supersonic Swirling Jets," AIAA Paper 93-3126, July 1993.

[2]Kraus, D. K., Cutler, A. D., "Mixing of Swirling Jets in a Supersonic Duct Flow," *Journal of Propulsion and Power*, Vol. 12, No. 1, 1995, pp. 170-177.

[3]Bushnell, D. M., "Hypervelocity Scramjet Mixing Enhancement," *Journal of Propulsion*, Vol. 11, No. 5, 1995, pp. 1088-1090.

[4]McClinton, C. R., "The Effect of Injection Angle on the Interaction Between Sonic Secondary Jets and a Supersonic Free Stream," NASA TN D-6669, February 1972.

[5]Mays, R. B., Thomas, R. H., Schetz, J. A., "Low Angle Injection Into a Supersonic Flow," AIAA Paper 89-2461, July 1989.

[6]Swithenbank, J., Chigier, N. A., "Vortex Mixing for Supersonic Combustion," *Proceedings of the Twelvth International Symposium on Combustion*, The Combustion Institute, 1968, pp. 1153-1162.

[7]Cutler, A. D., Levey, B. S., Kraus, D. K., "An Experimental Investigation of Supersonic Swirling Jets," AIAA Paper 93-2922, July 1993.

[8]Cutler, A. D., Levey, B. S., "Vortex Breakdown in a Supersonic Jet," AIAA Paper 91-1815, June 1991.

[9]Levey, B. S., "An Experimental Investigation of Supersonic Vortical Flow," M.S. Thesis, School of Engineering and Applied Science, The George Washington University, September 1991.

[10]Kraus, D. K., "An Experimental Investigation of Mixing Enhancement in a Simulated Scramjet Combustor by Use of Swirling Jets," M.S. Thesis, School of Engineering and Applied Science, The George Washington University, August 1993.

[11]Johnson, C., "Applications of Streamwise Vorticity in Enhancement of Injectant Mixing and Penetration in a Supersonic Flow," M.S. Thesis, School of Engineering and Applied Science, The George Washington University, May 1996.

[12]Compton, D. A., Johnston, J. P., "Streamwise Vortex Production by Pitched and Skewed Jets in a Turbulent Boundary Layer," *AIAA Journal*, Vol. 30, No. 3, 1992, pp. 640-647.

[13]Fuller, E. J., Mays, R. B., Thomas, R. H., Schetz, J. A., "Mixing Studies of Helium in Air at High Supersonic Speeds," *AIAA Journal*, Vol. 30, No. 9, 1992, pp. 2234-2243.

[14]Northam, G. B., Greenberg, I., Byington, C. S., "Evaluation of Parallel Injector Configurations for Supersonic Combustion," AIAA Paper 89-2525, July 1989.

[15]Stouffer, S. D., Baker, N. R., Capriotti, D. P., Northam, G. B., "Effects of Compression and Expansion-Ramp Fuel Injector Configurations on Scramjet Combustion and Heat Transfer," AIAA Paper 93-0609, January 1993.

[16]Riggins, D. W., McClinton, C. R., "Analysis of Losses in Supersonic Mixing and Reacting Flows," AIAA Paper 91-2266, June 1991.

[17]Quinn, J. E., "Effects of Mass Injection on Supersonic Cavity Drag with Applications to Scramjets," M.S. Thesis, School of Engineering and Applied Science, The George Washington University, September 1997.

[18]Omega Complete Temperature Measurement Handbook and Encyclopedia, Omega Engineering, Inc., 1995.

[19]Cutler, A. D., Johnson, C. H., "Analysis of Intermittency and Probe Data in a Supersonic Flow with Injection," *Experiments in Fluids*, No. 23, 1997, pp. 38-47.

[20]Carty, A. A., "Mixing of Co-axial Jet in a Co-annular Flow," M.S. Thesis, School of Engineering and Applied Science, The George Washington University, August 1998.

[21]Reis, V. H., Fenn, J. B., "Separation of Gas Mixtures in Supersonic Jets," *The Journal of Chemical Physics*, Vol. 39, No. 12, 1963, pp. 3240-3250.

[22]Ninnemann, T. A., Ng, W. F., "A Concentration Probe for the Study of Mixing in Supersonic Shear Flows," *Experiments in Fluids*, No. 13, 1992, pp. 98-104.

[23]Anderson, J. D., "Conical Flow," *Modern Compressible Flow with Historical Perspective*, 2nd ed., McGraw-Hill, New York, 1990, pp. 294-306.

[24]Zhang, X., Collins, M. W., "Flow and Heat Transfer in a Turbulent Boundary Layer Through Skewed and Pitched Jets," *AIAA Journal*, Vol. 31, No. 9, 1993, pp. 1590-1599.

TABLES

	mean	run-to-run variation	total uncertainty
$p_{t,\infty}$ (kPa)	794	±3	±5
p_{∞} (kPa)	105.4	±0.3	±1.7
$T_{t,\infty}$ (K)	299	±6	±6
$p_{t,j} / p_{t,\infty}$	5.40	±0.03	±0.05
$T_{t,j} / T_{t,\infty}$	1.03	±0.02	±0.02
$\dot{m}_j$ (swirl) (kg/s)	0.0333	±0.0003	±0.0014
$\dot{m}_j$ (nonswirl) (kg/s)	0.0355	±0.0003	±0.0015

Table 2-1. Experimentally measured flow conditions with He/O_2 as injectant.

	nonswirl	swirl
p_j (kPa)	228.6	225.3*
M_j	2.584	2.594*
$\mathrm{atan}(v_{\theta,j} / u_j)$	0.0	15.49*
u_j / u_{∞}	2.450	2.364
$\dot{m}_j$ (kg/s)	0.03784	0.03794
$\dot{m}_{\infty}$ (kg/s)	3.731	3.731

(* - these quantities are applicable at the outer edge of the jet only)

Table 2-2. Calculated exit flow conditions based on nominal conditions.

61

case	swirl	skew angle	ramp	offset wall	survey locations (mm)
N0	no	0°			25.4, 127.0, 228.6
N25	no	25°			127.0
S0	yes	0°			127.0, 228.6
S25	yes	25°			25.4, 127.0, 228.6
S-25	yes	-25°			127.0
S25X	yes	25°		X	127.0, 228.6
N0S	no	0°	Swept		127.0, 228.6
N25R	no	25°	Unswept	X	127.0, 228.6
S25R	yes	25°	Unswept	X	127.0, 228.6
S-25R	yes	-25°	Unswept	X	127.0, 228.6

Table 3-1. Test Cases.

case	duct height	injected gas	start z	end z	z spacing	number surveys	start y	end y	y spacing	number points per survey	pitot probe height above exit plane
N25	127.0	all	-38.1	38.1	3.18	29	1.52	37.08	2.54	15	0.610-0.711
S25	127.0	all	-38.1	38.1	3.18	29	1.52	37.08	2.54	15	0.610-0.711
S0	127.0	all	-38.1	38.1	3.18	29	1.52	37.08	2.54	15	0.610-0.711
S-25	127.0	all	-38.1	38.1	3.18	29	1.52	37.08	2.54	15	0.610-0.711
N0	127.0	all	-38.1	38.1	3.18	29	1.52	37.08	2.54	15	0.610-0.711
N0	228.6	all	-38.1	38.1	6.35	15	2.16	36.45	3.81	10	0.457-0.559
S25	228.6	all	-38.1	38.1	6.35	15	2.16	36.45	3.81	10	0.457-0.559
S25	25.4	air, none	-38.1	38.1	3.18	29	1.52	37.08	2.54	15	0.483-0.584
N0	25.4	air, none	-38.1	38.1	3.18	29	1.52	37.08	2.54	15	0.483-0.584
S25	25.4	He/O_2	-12.7	12.7	3.18	12	1.52	24.38	2.54	10	0.483-0.584
N0	25.4	He/O_2	-19.05	9.53	3.18	13	1.52	24.38	2.54	10	0.483-0.584
S25X	127.0	air, none	38.1	-19.05	-6.35	13	36.45	2.16	-3.81	10	0.381-0.457
S25X	127.0	He/O_2	19.05	-19.05	-6.35	10	36.45	2.16	-3.81	10	0.381-0.457
S25R	127.0	air, none	38.1	-19.05	-6.35	13	36.45	2.16	-3.81	10	0.457-0.559
S25R	127.0	He/O_2	19.05	-19.05	-6.35	10	36.45	2.16	-3.81	10	0.457-0.559
N25R	127.0	air, none	38.1	-19.05	-6.35	13	36.45	2.16	-3.81	10	0.457-0.559
N25R	127.0	He/O_2	19.05	-19.05	-6.35	10	36.45	2.16	-3.81	10	0.457-0.559
S25R	127.0	air, none	38.1	-19.05	-6.35	13	36.45	2.16	-3.81	10	0.381-0.457
S25R	127.0	He/O_2	19.05	-19.05	-6.35	10	36.45	2.16	-3.81	10	0.381-0.457
N0S	127.0	air, none	38.1	-38.1	-6.35	16	36.45	2.16	-3.81	10	0.457-0.559
N0S	127.0	He/O_2	31.75	-31.75	-6.35	14	36.45	2.16	-3.81	10	0.457-0.559
S-25R	127.0	air, none	-38.1	19.05	6.35	13	2.16	36.45	3.81	10	0.406-0.508
S-25R	127.0	He/O_2	-19.05	19.05	6.35	10	2.16	36.45	3.81	10	0.406-0.508
S-25R	228.6	air, none	-38.1	19.05	6.35	13	2.16	36.45	3.81	10	0.330-0.432
S-25R	228.6	He/O_2	-19.05	19.05	6.35	10	2.16	36.45	3.81	10	0.330-0.432
N0S	228.6	air, none	38.1	-38.1	-6.35	16	36.45	2.16	-3.81	10	0.330-0.457
N0S	228.6	He/O_2	31.75	-31.75	-6.35	14	36.45	2.16	-3.81	10	0.330-0.457
N25R	228.6	air, none	38.1	-19.05	-6.35	13	36.45	2.16	-3.81	10	0.457-0.508
N25R	228.6	He/O_2	19.05	-19.05	-6.35	10	36.45	2.16	-3.81	10	0.457-0.508
S25R	228.6	air, none	38.1	-19.05	-6.35	13	36.45	2.16	-3.81	10	0.457-0.508
S25R	228.6	He/O_2	19.05	-19.05	-6.35	10	36.45	2.16	-3.81	10	0.457-0.508
S25X	228.6	air, none	38.1	-19.05	-6.35	13	36.45	2.16	-3.81	10	0.457-0.508
S25X	228.6	He/O_2	19.05	-19.05	-6.35	10	36.45	2.16	-3.81	10	0.457-0.508

Table 3-2. Grid spacing for survey measurements.

63
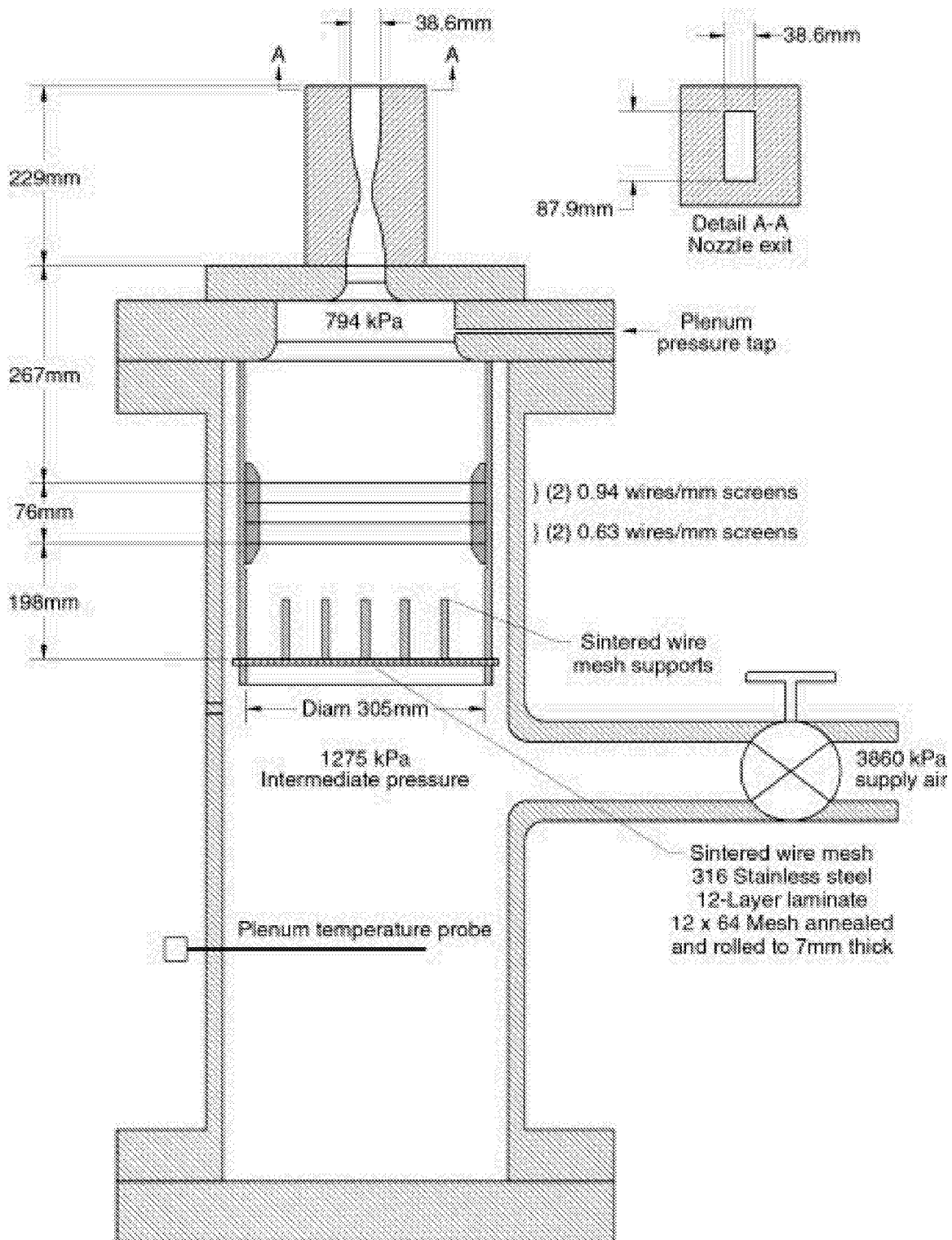
FIGURES

Figure 2-1.   Detail of Transverse Jet Facility (TJF).
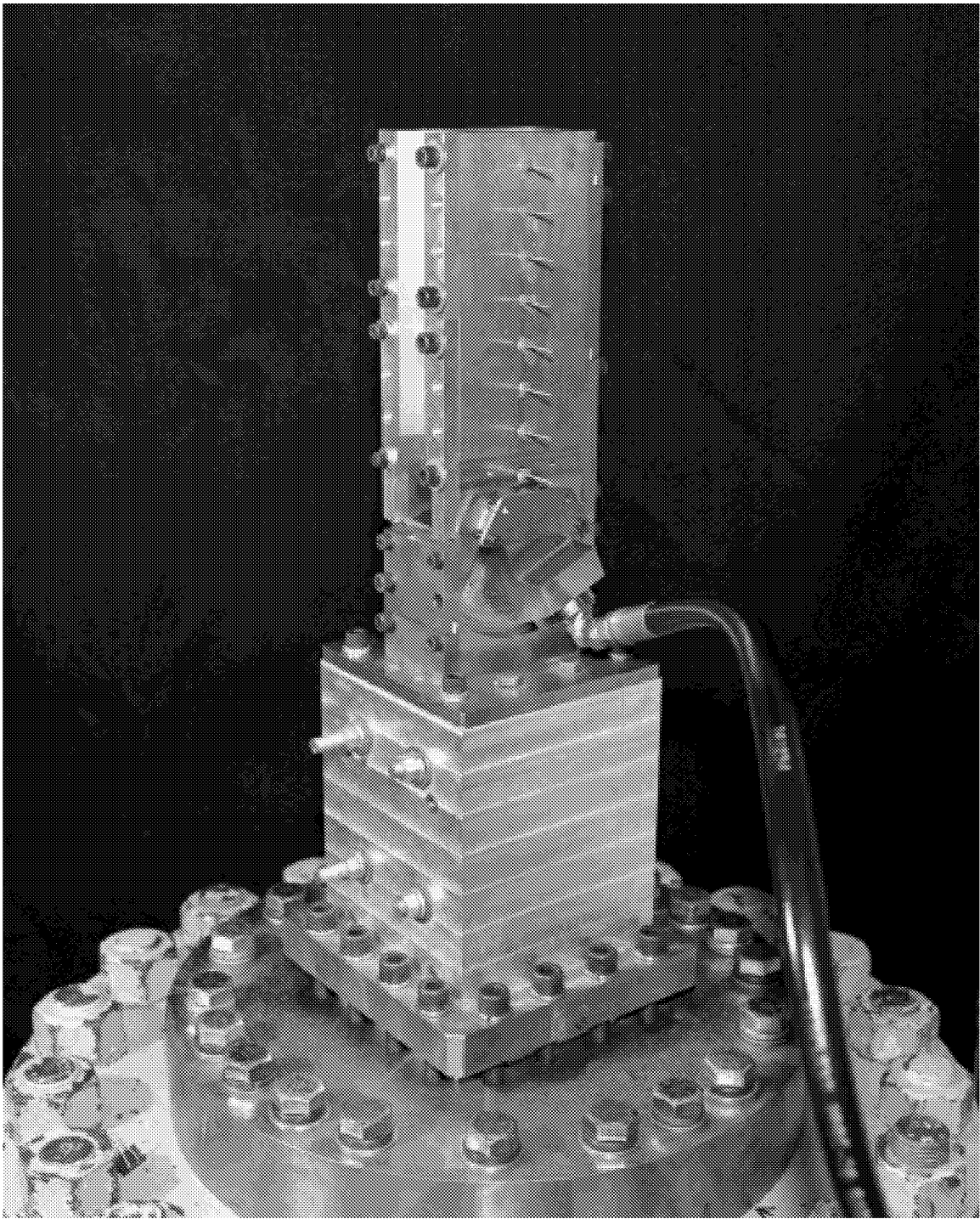
Figure 2-2   Duct and nozzle mounted on TJF
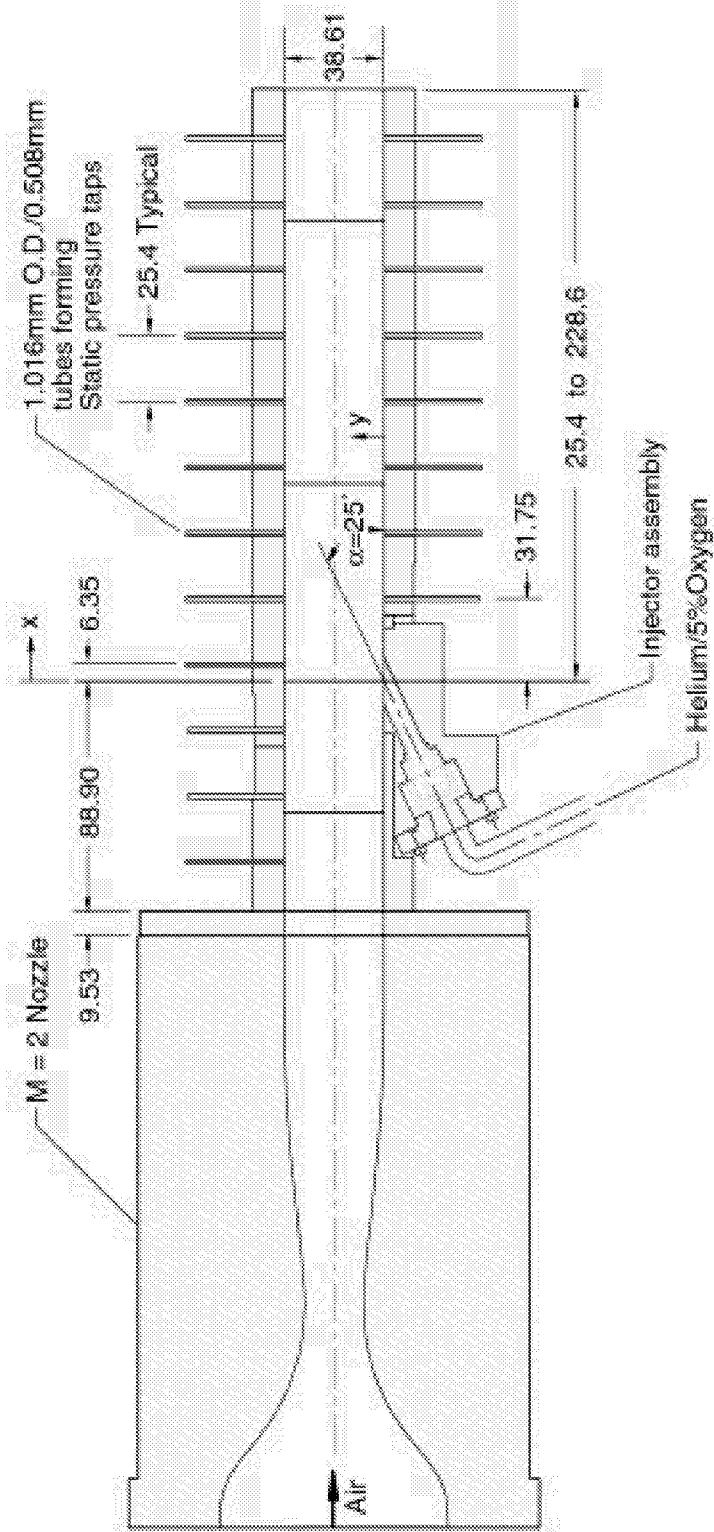
Figure 2.3. Mach 2 nozzle and duct model with injector ($\beta = 0$)
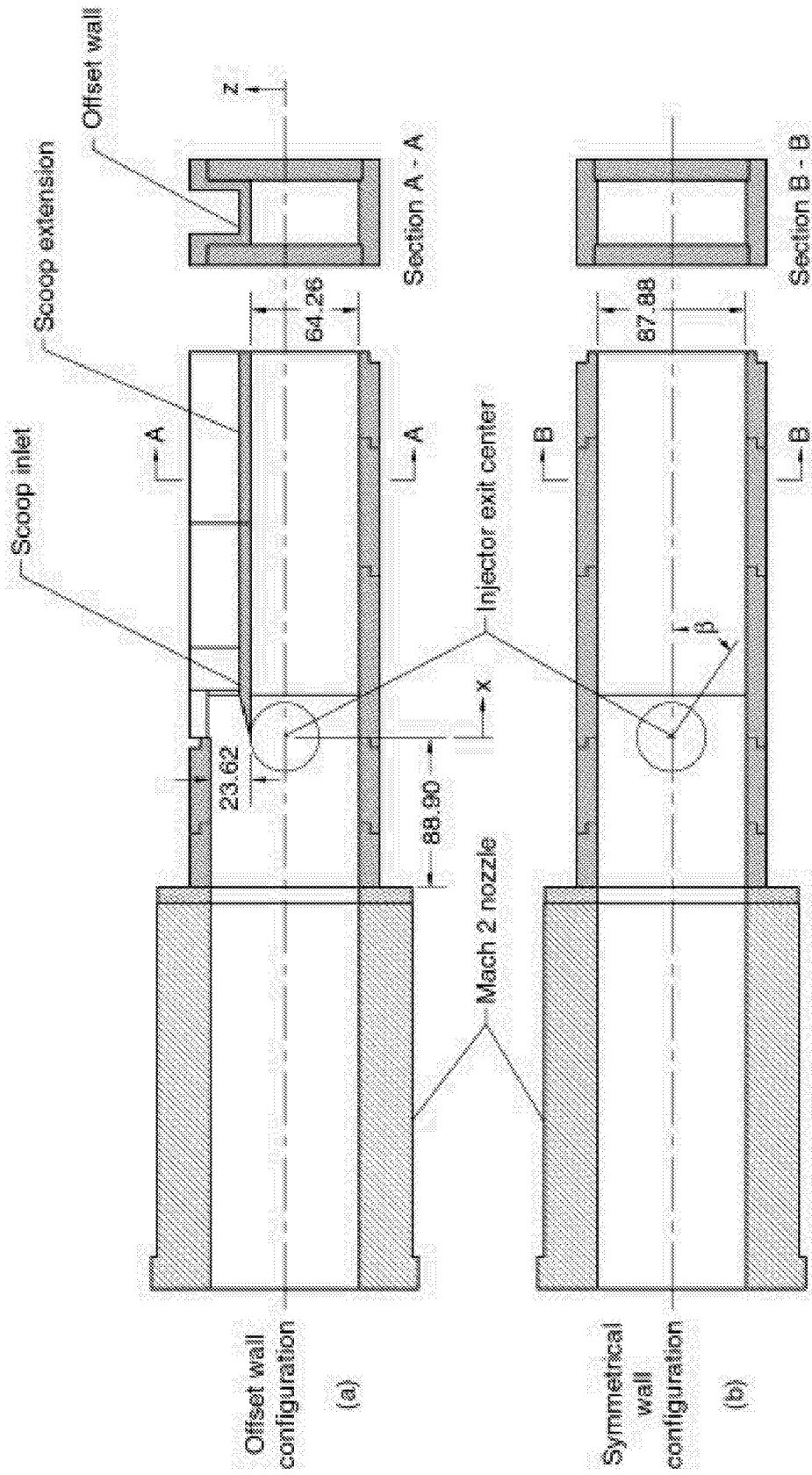
Figure 2-4. Section of nozzle and duct.
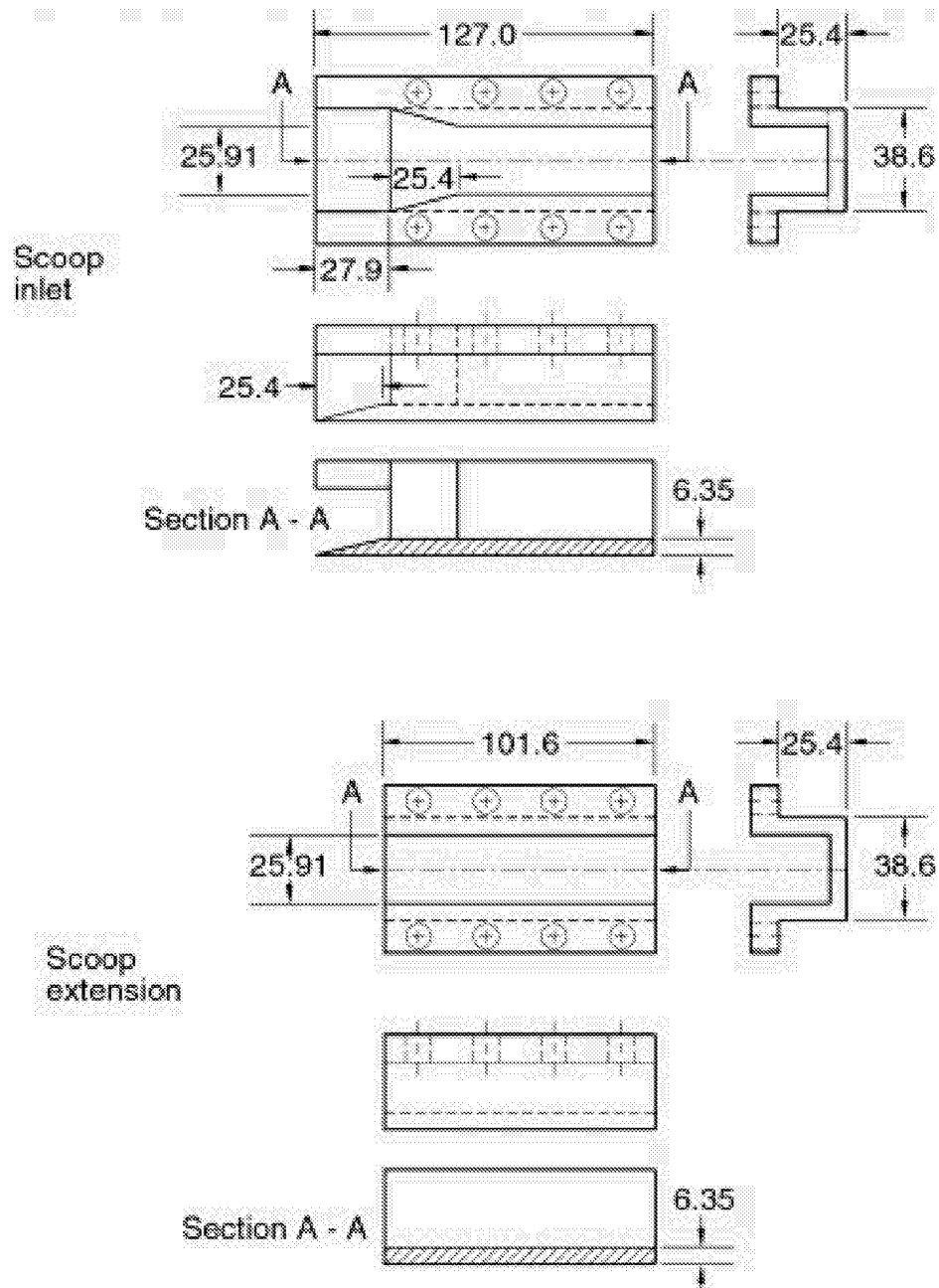
Figure 2-5.   Offset wall parts.
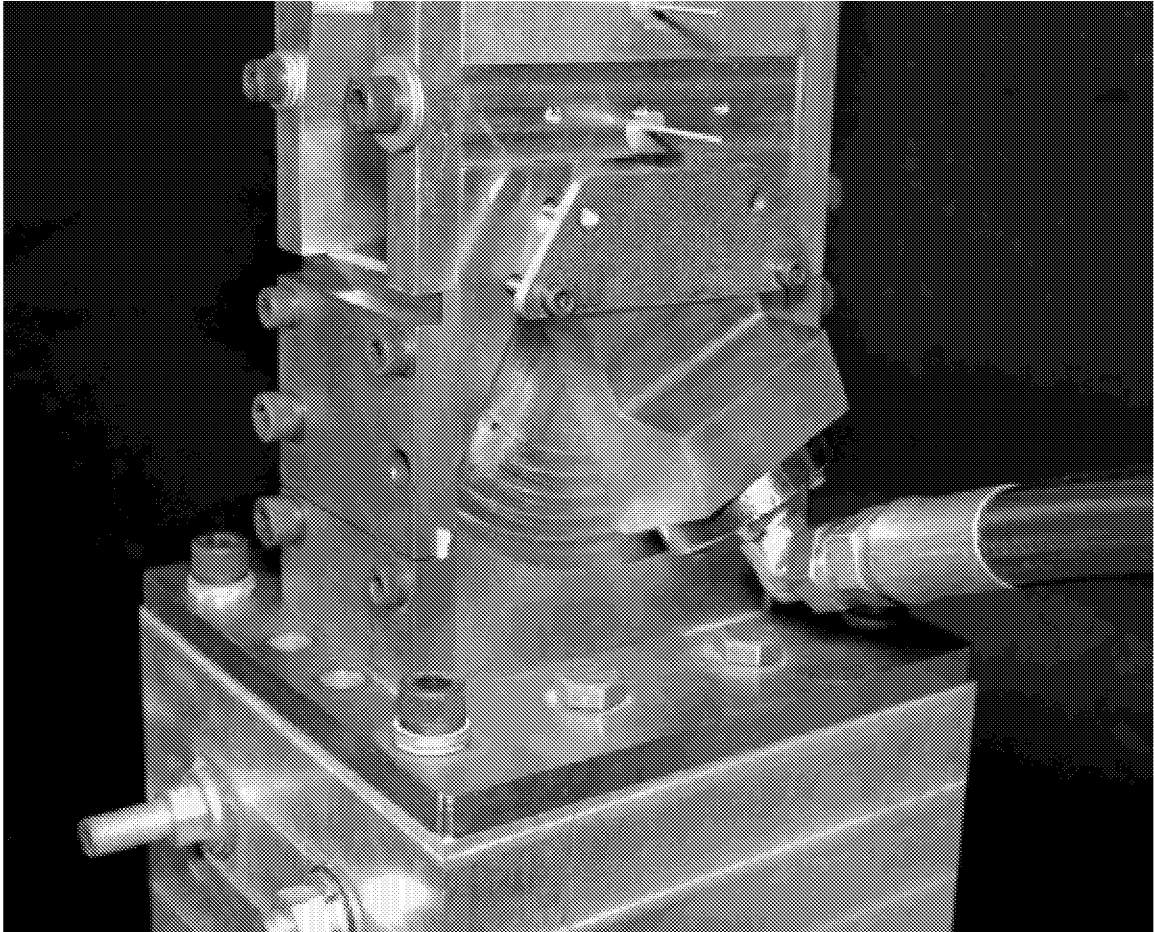
Figure 2-6   Injector on duct at $\beta = +25°$
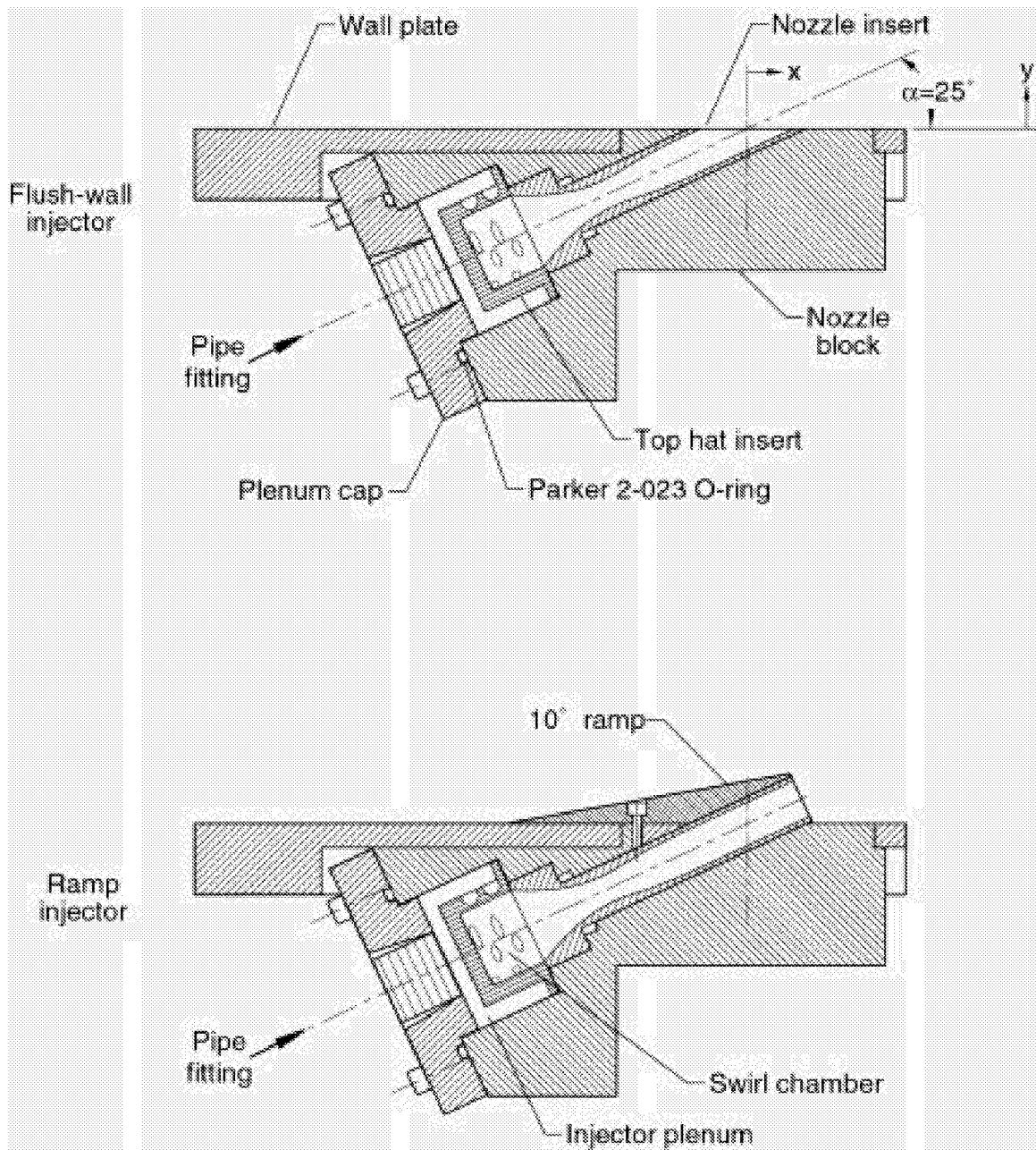
Figure 2-7.   Injector assembly, cross-section view ($\beta = 0$).
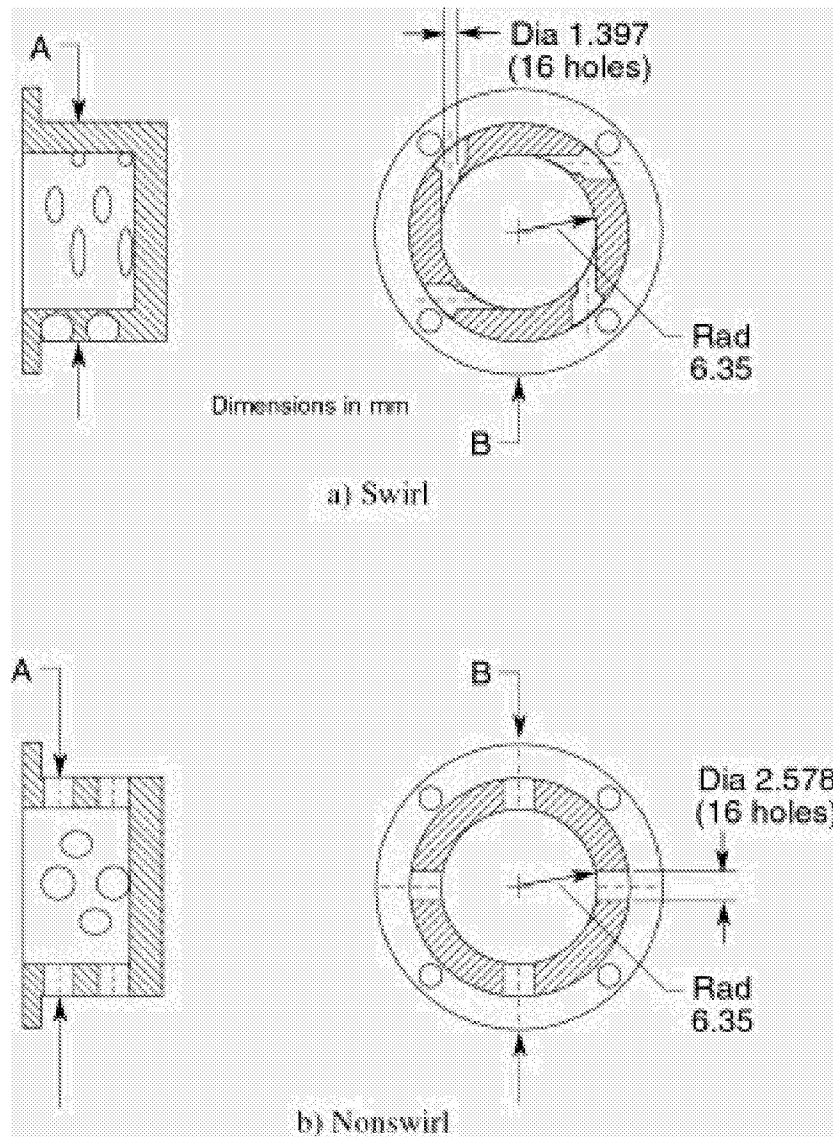
Figure 2-8. Top-hat inserts (Section A looking downstream).

71

Swirl

Nonswirl

Flush-wall injector

Ramp injector

⌀ 6.35

⌀ 4.93

25°
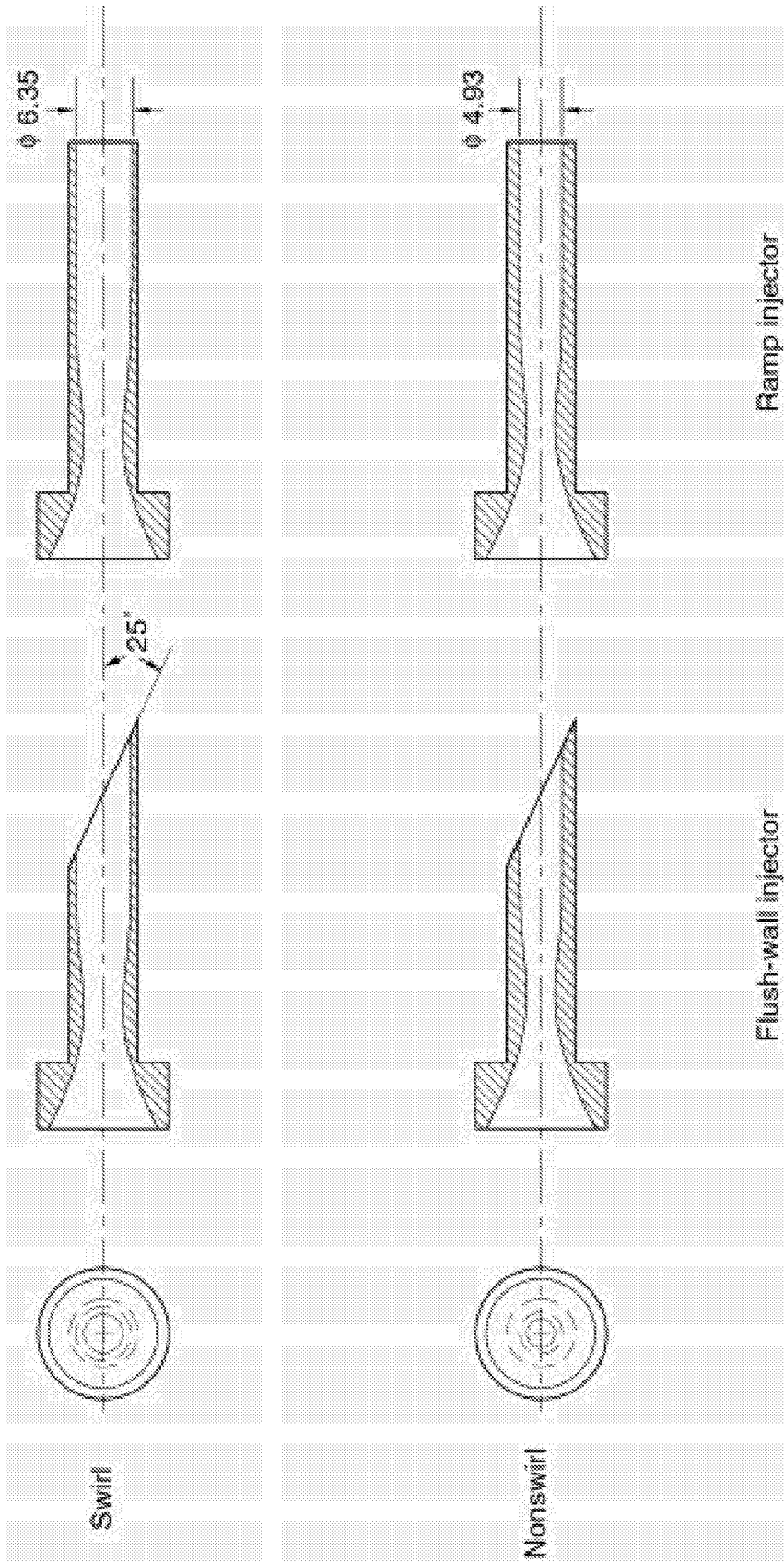
Figure 2-9. Injector nozzle inserts. (4)
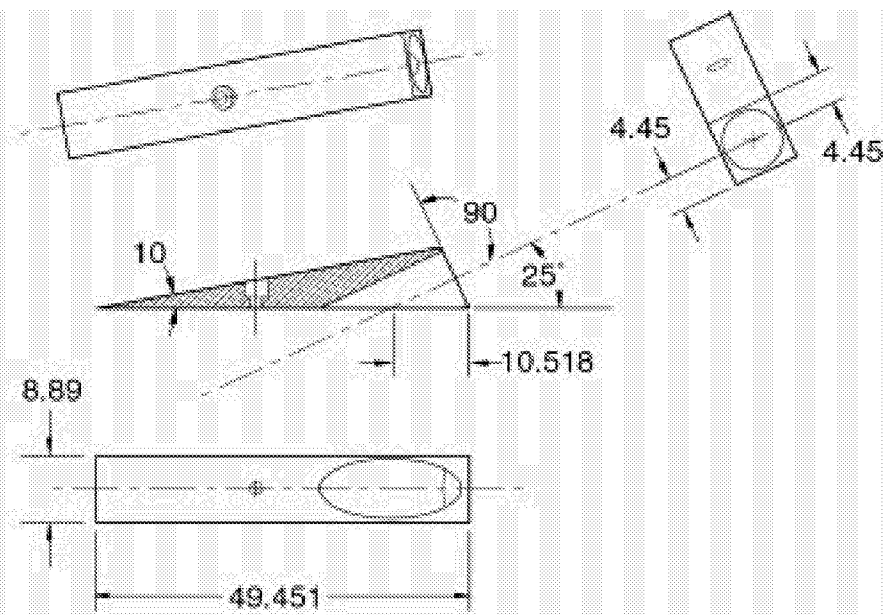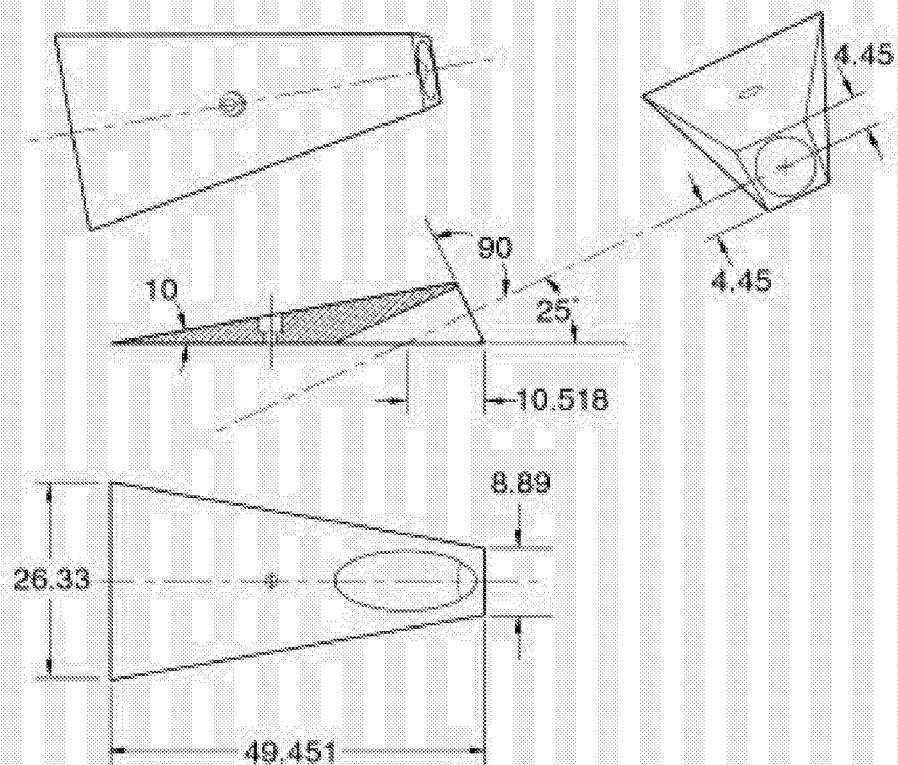
Figure 2-10.   Injector nozzle ramps.

Temperature probe
set back to reduce
shock wave effect
on core probe

x

z

Top View

16.5

3.8

6.35

114.3

9.53

Side View

20° incl.

88.9

End View
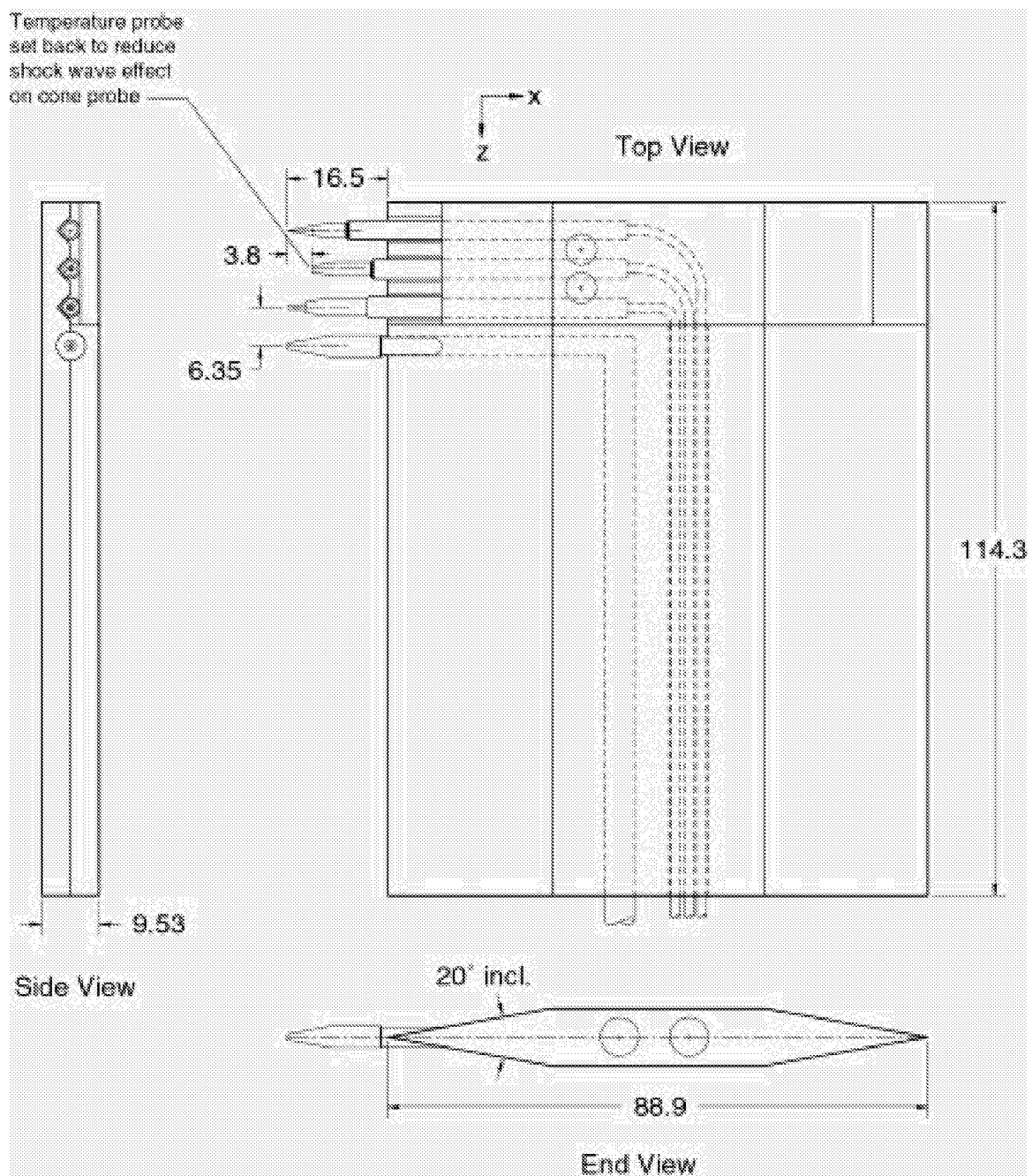
Figure 3-1.   Flow field survey probes and rake assembly.
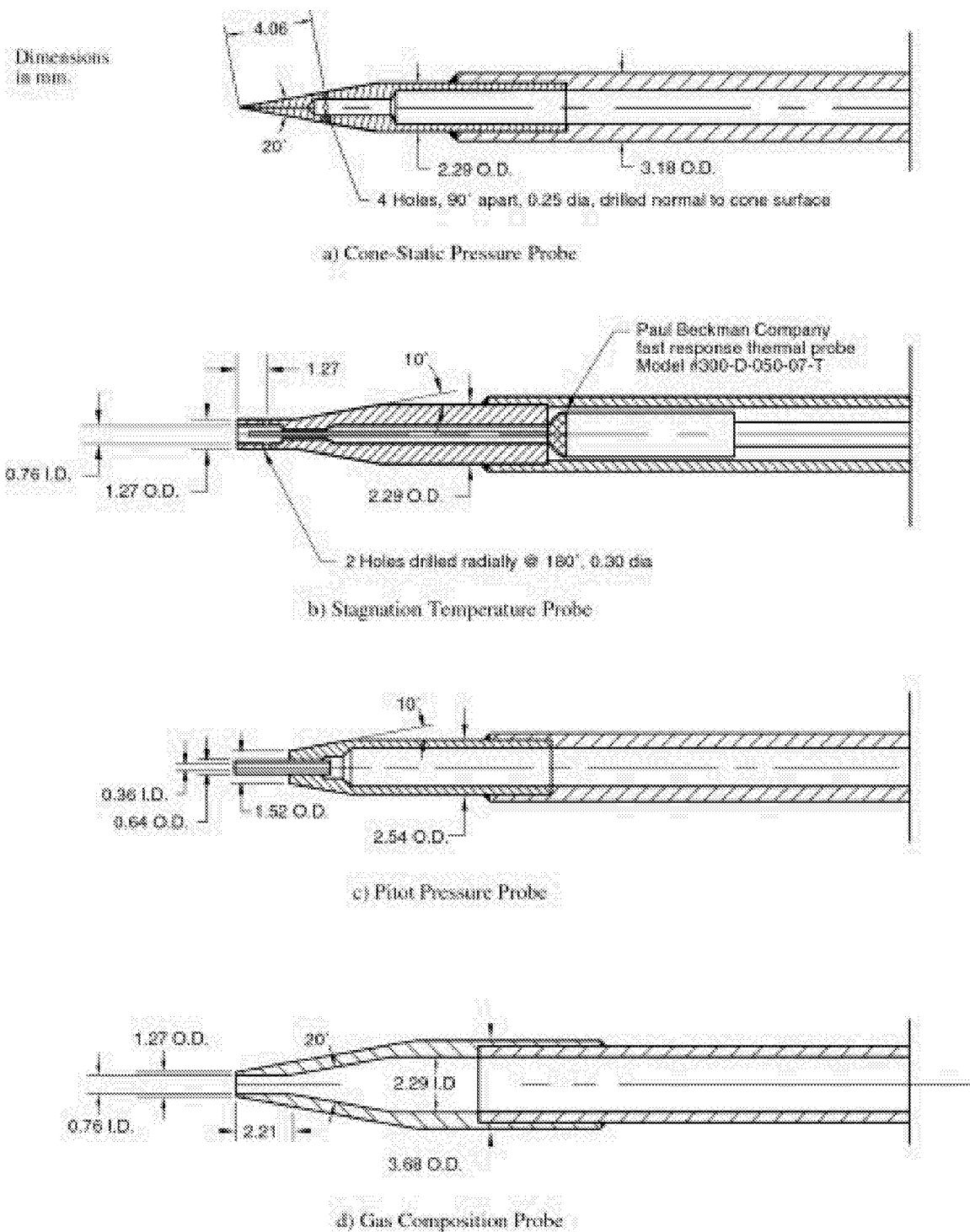
Figure 3-2. Flow field survey probes.

■ = Submerged in ice bath (T ≈ 0°C)

Gas composition probe tip

1.07m Copper tubing, 4.78mm O.D., 3.25mm I.D.

1.8m Copper tubing, 4.78mm O.D., 3.25mm I.D.

T_{gc}
"T"-type thermocouple probe

Discharge to atmosphere

P_{bld}
Pressure transducer

Hot film voltage to computer A/D

0.6m Copper tubing, 9.53mm O.D., 7.49mm I.D.

DISA CTA Bridge with 5m cable compensator

DANTEC 55R01 straight, general-purpose fiber-film probe

Flow straightening and development section (stainless steel tubing, 3.18mm O.D., 2.29mm I.D. length = 254mm)

2.29mm I.D.

5m Cable

P_{vac}
Pressure transducer

Hot-film probe holder

Sonic orifice 0.533mm I.D.

Vacuum pump

Figure 3-3.   Gas composition analyzer system.

76

$$Cf = \left[3.5 \left(\frac{\gamma - 1}{\gamma} \right) \right]^{1.04216}$$
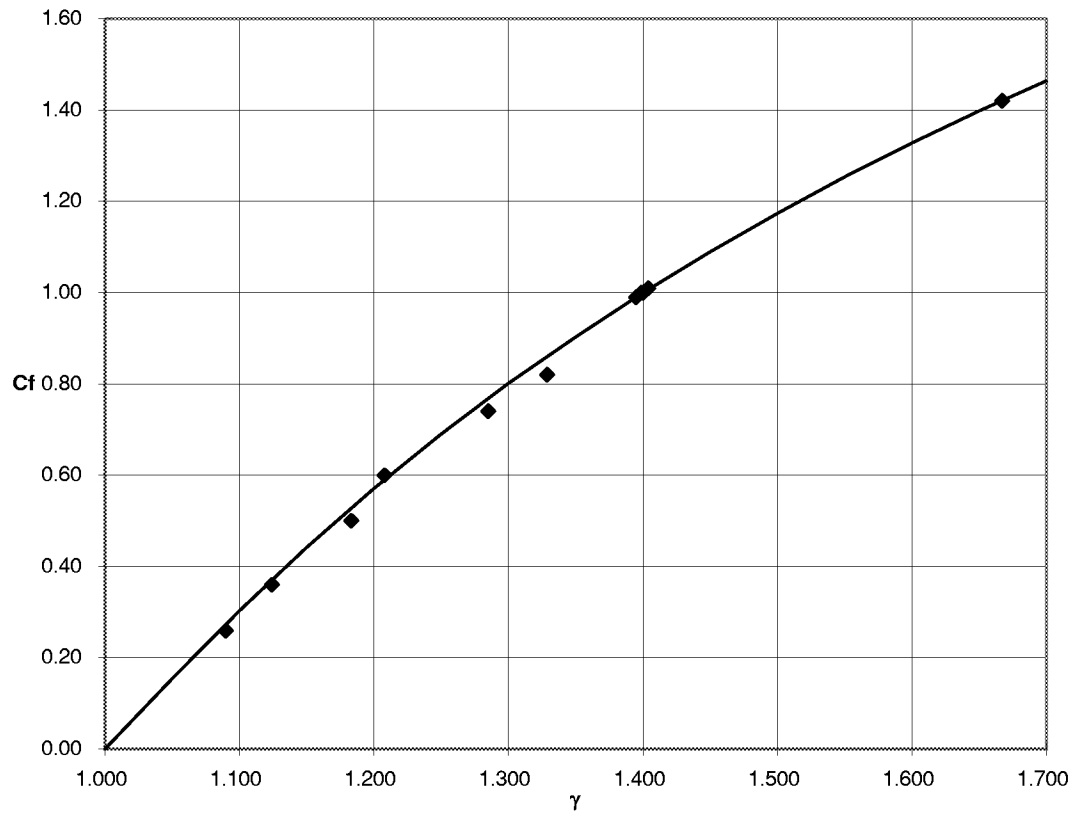
Figure 3-4. Correction factor for Tylan General flowmeter/controller.

$$y = 2.93473E\text{-}04x^4 - 6.93765E\text{-}03x^3 + 2.89089E\text{-}02x^2 + 4.69410E\text{-}01x - 2.54706E\text{+}00$$
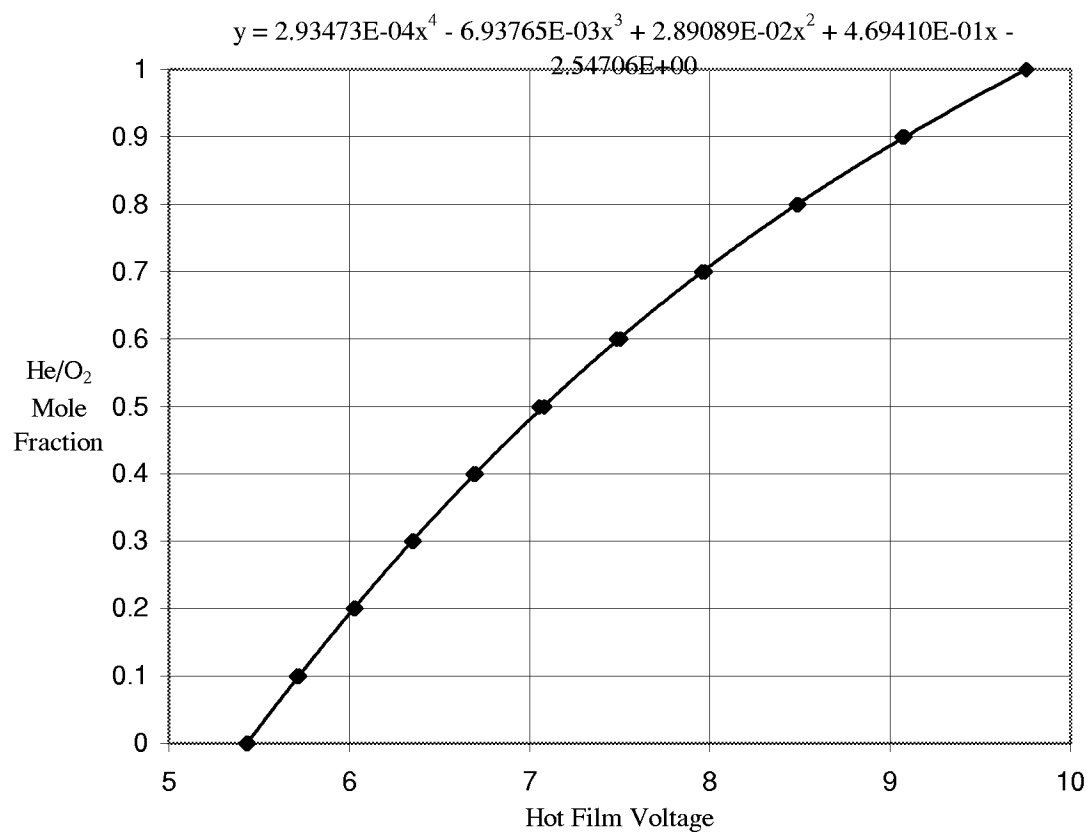
Figure 3-5.   Typical hot film calibration data and curve fit.
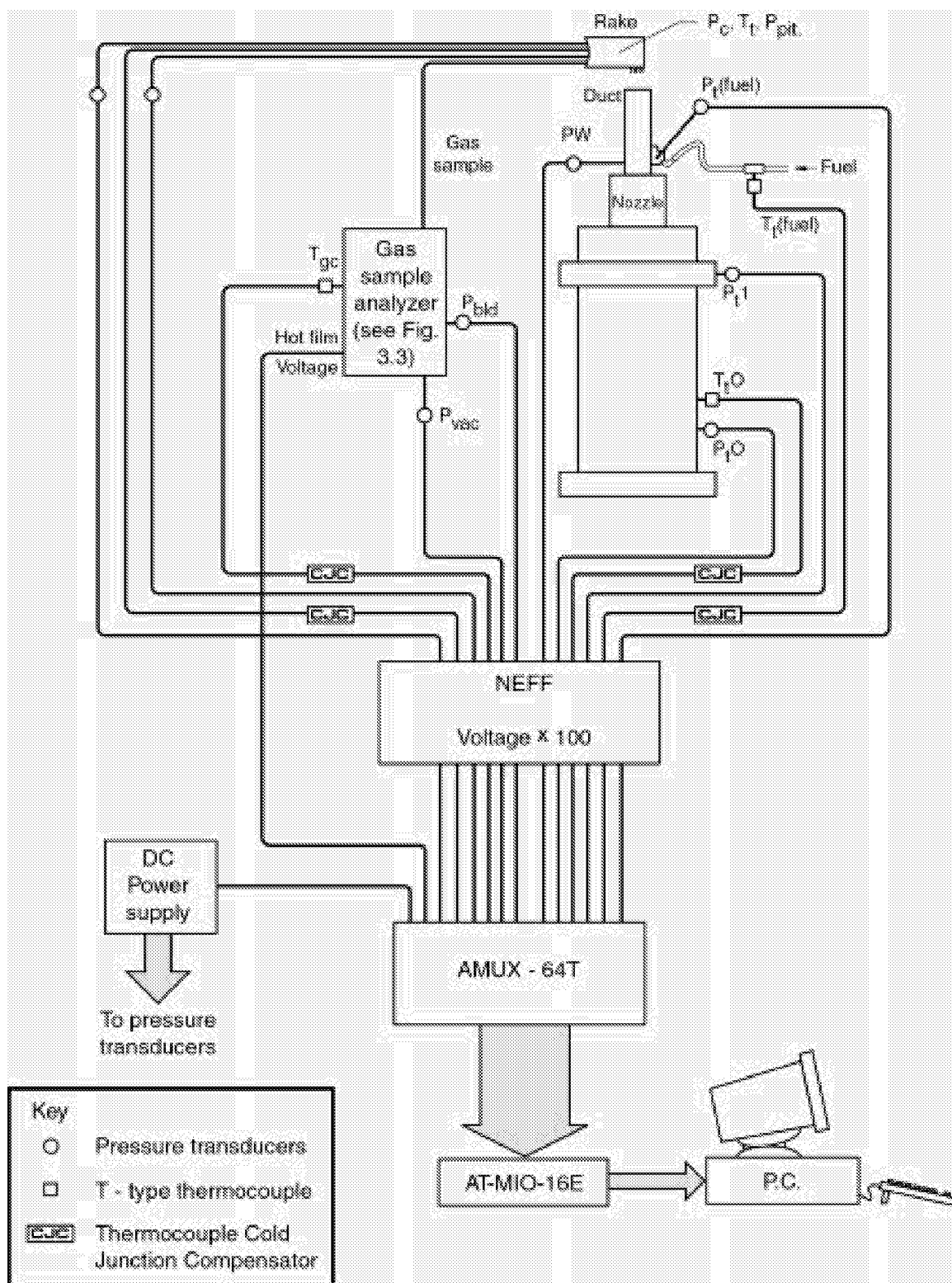
Figure 3-6.   Data acquisition system.
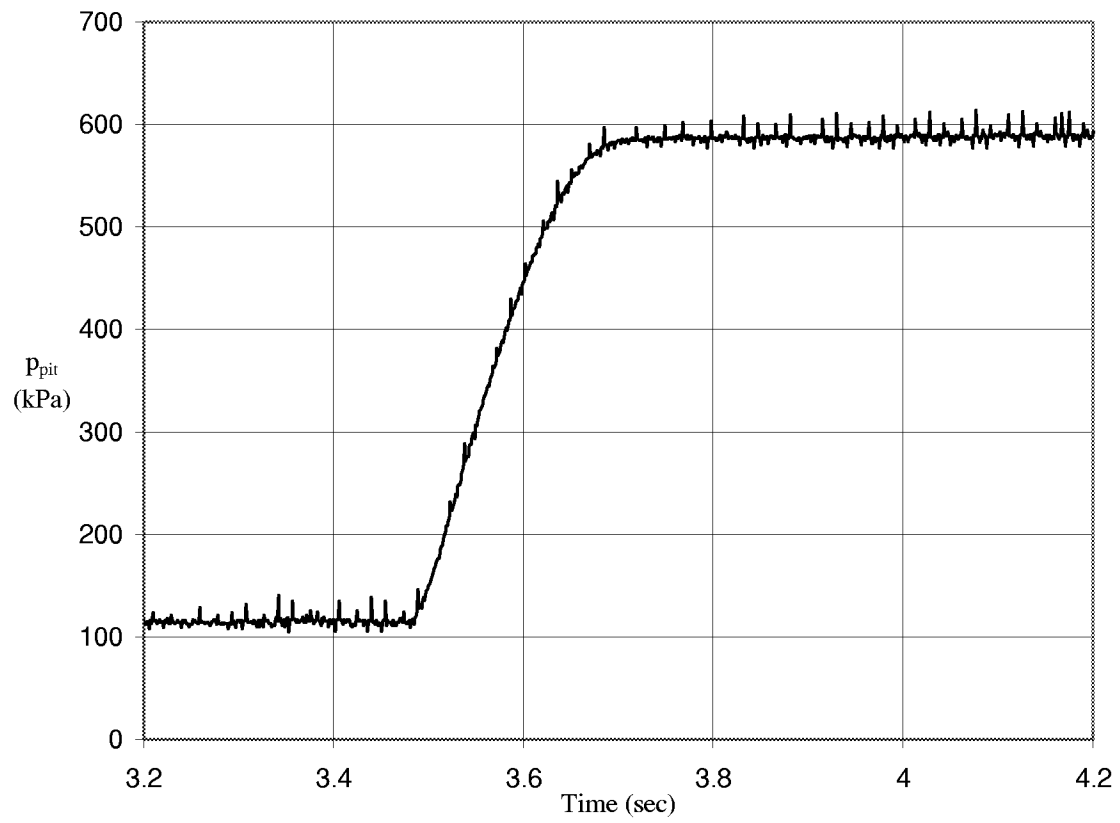
Figure 3-7.   Pitot pressure time response.
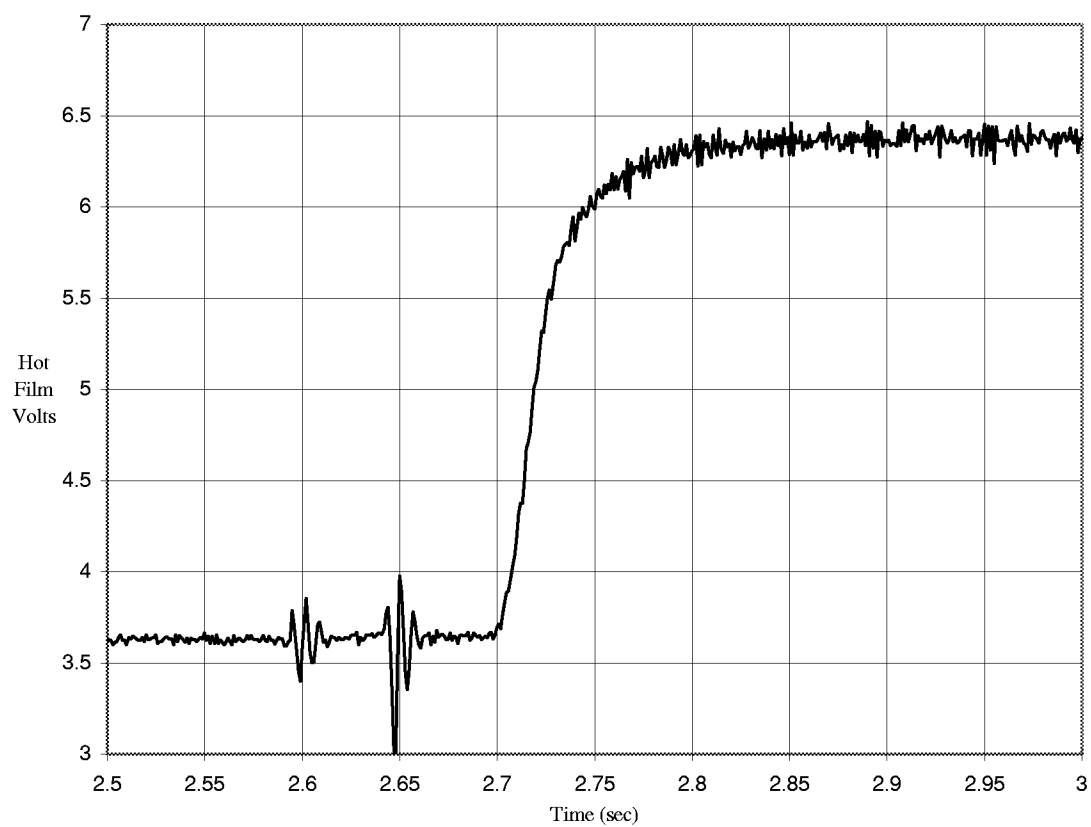
Figure 3-8.   Hot film voltage time response.
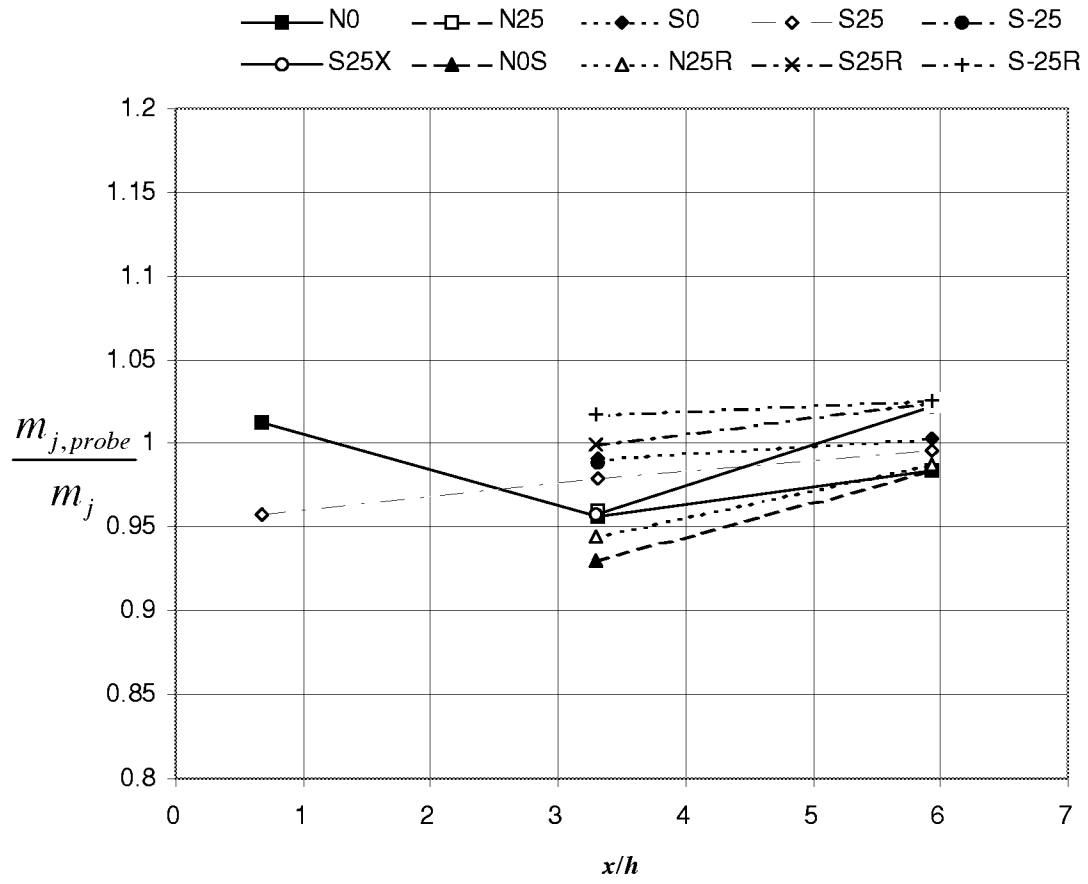
Figure 3-9. Ratio of integrated He/O₂ mass flow rate (based on probe data) to He/O₂ mass flow rate determined from injector nozzle calibration.
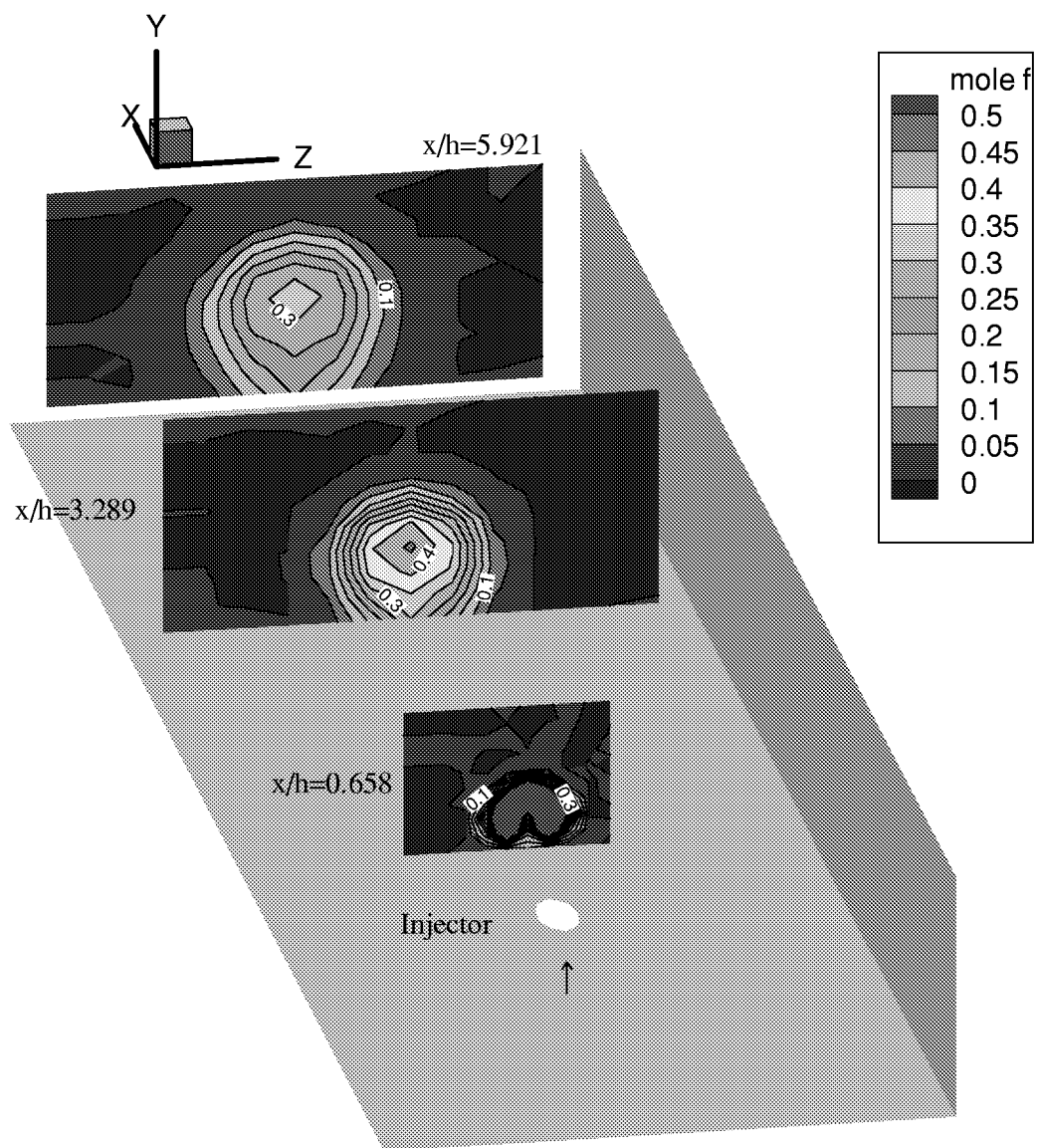
Figure 4-1(a). He/O_2 mole fractions for nonswirl, 0° skew, flush wall injector (N0).
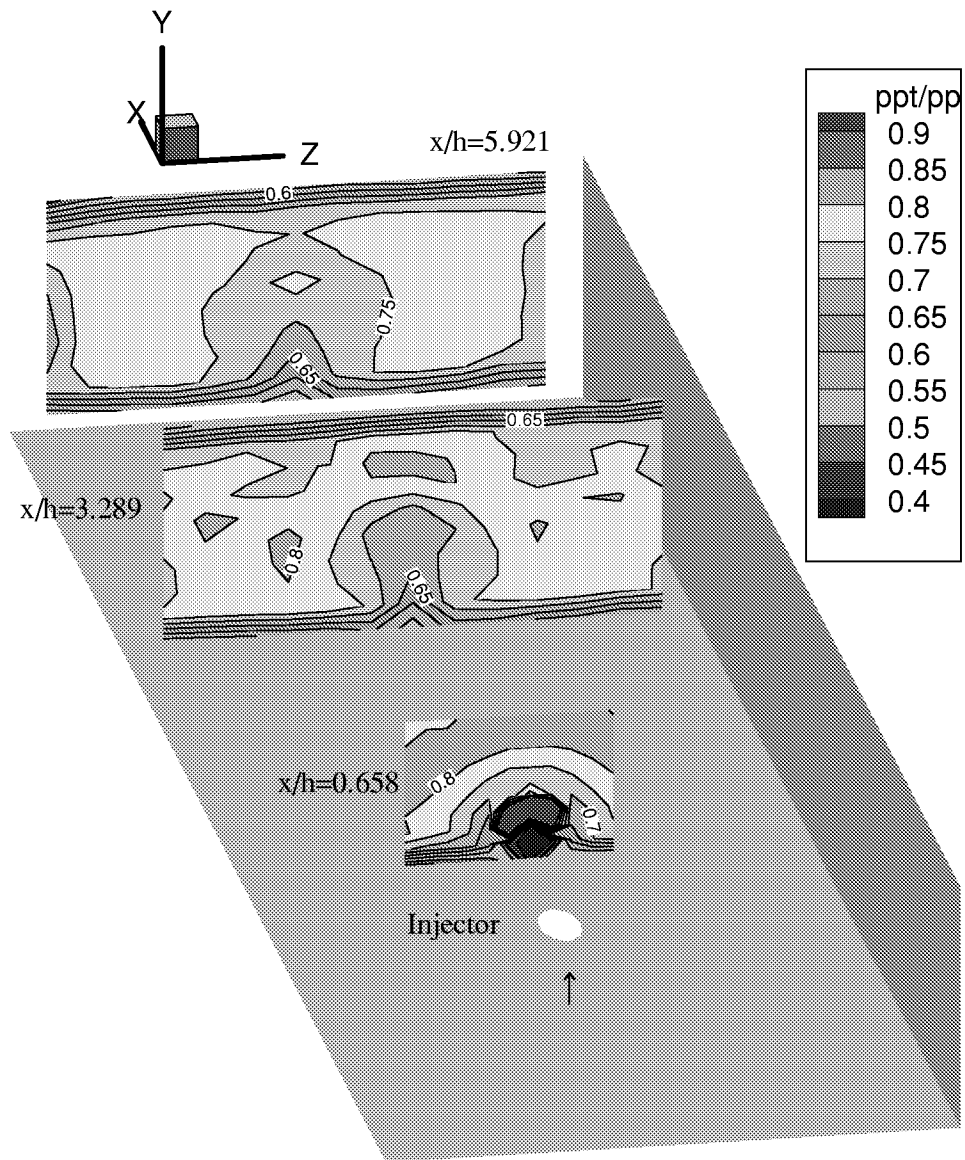
Figure 4-1(b). Pitot pressures (p_{pit} / $p_{t,\infty}$) for nonswirl, 0° skew, flush wall injector (N0).
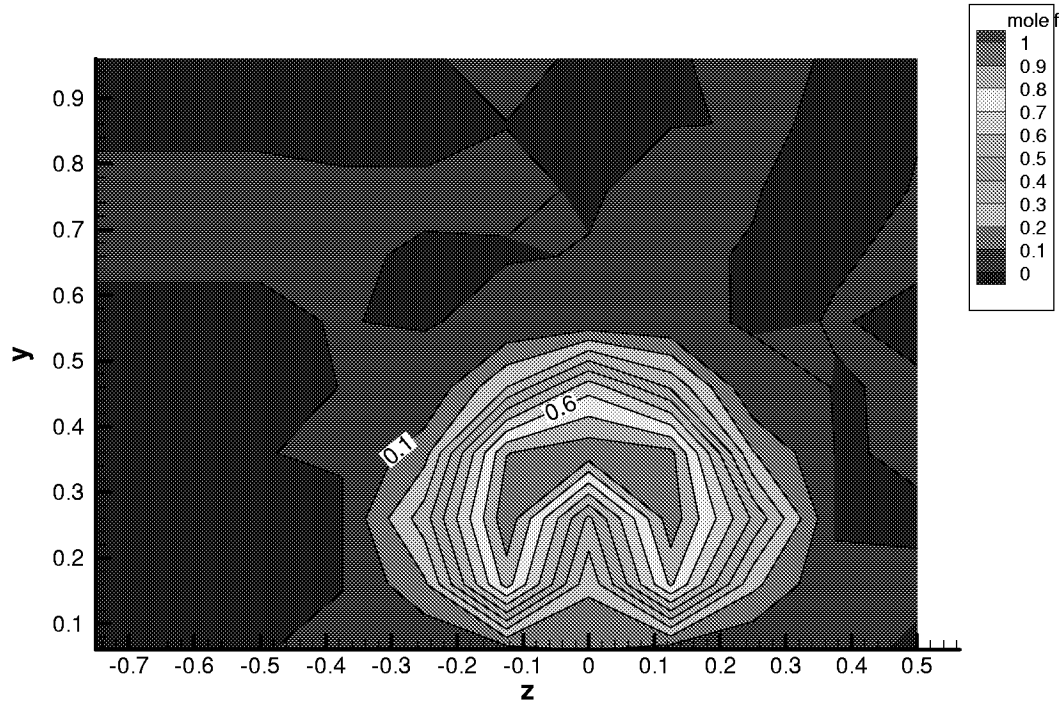
Figure 4-1(c). Close-up of $x/h = 0.658$ mole fractions of N0 case.
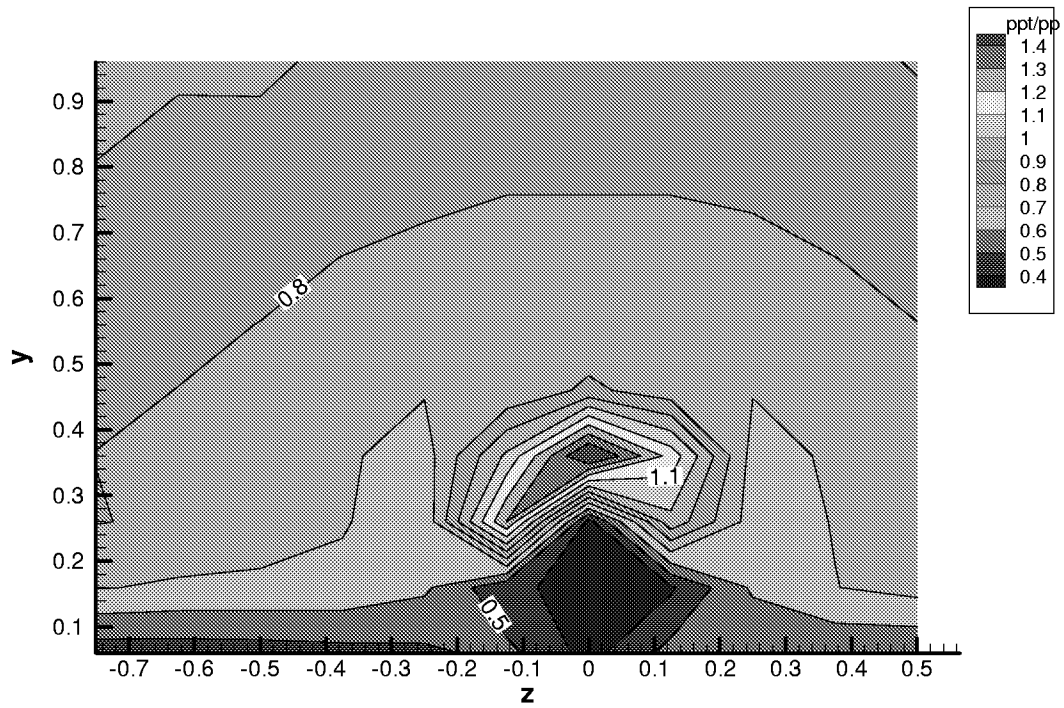
Figure 4-1(d). Close-up of $x/h = 0.658$ Pitot pressures of N0 case.
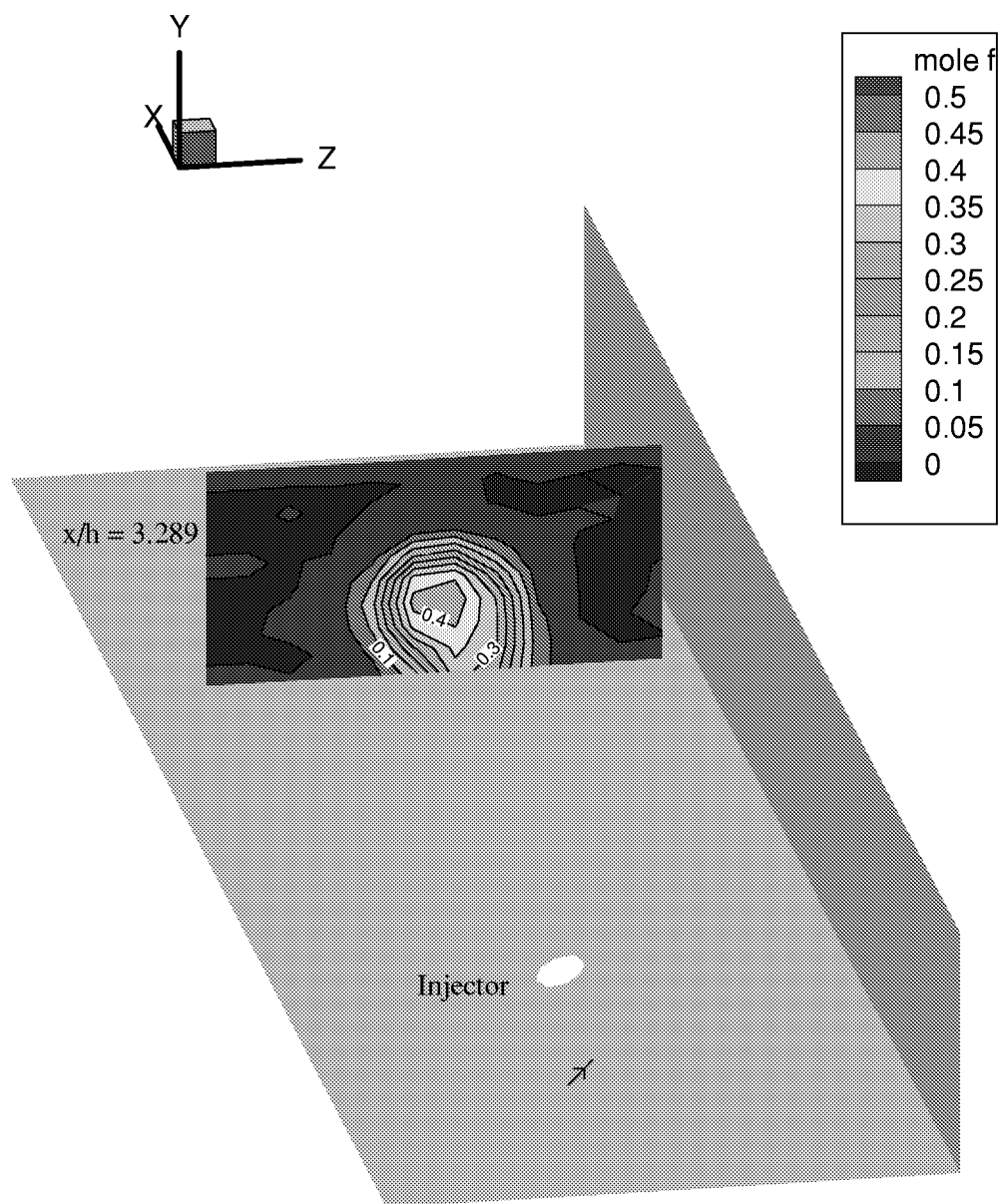
Figure 4-2(a). He/O$_2$ mole fractions for nonswirl, 25° skew, flush wall injector (N25).
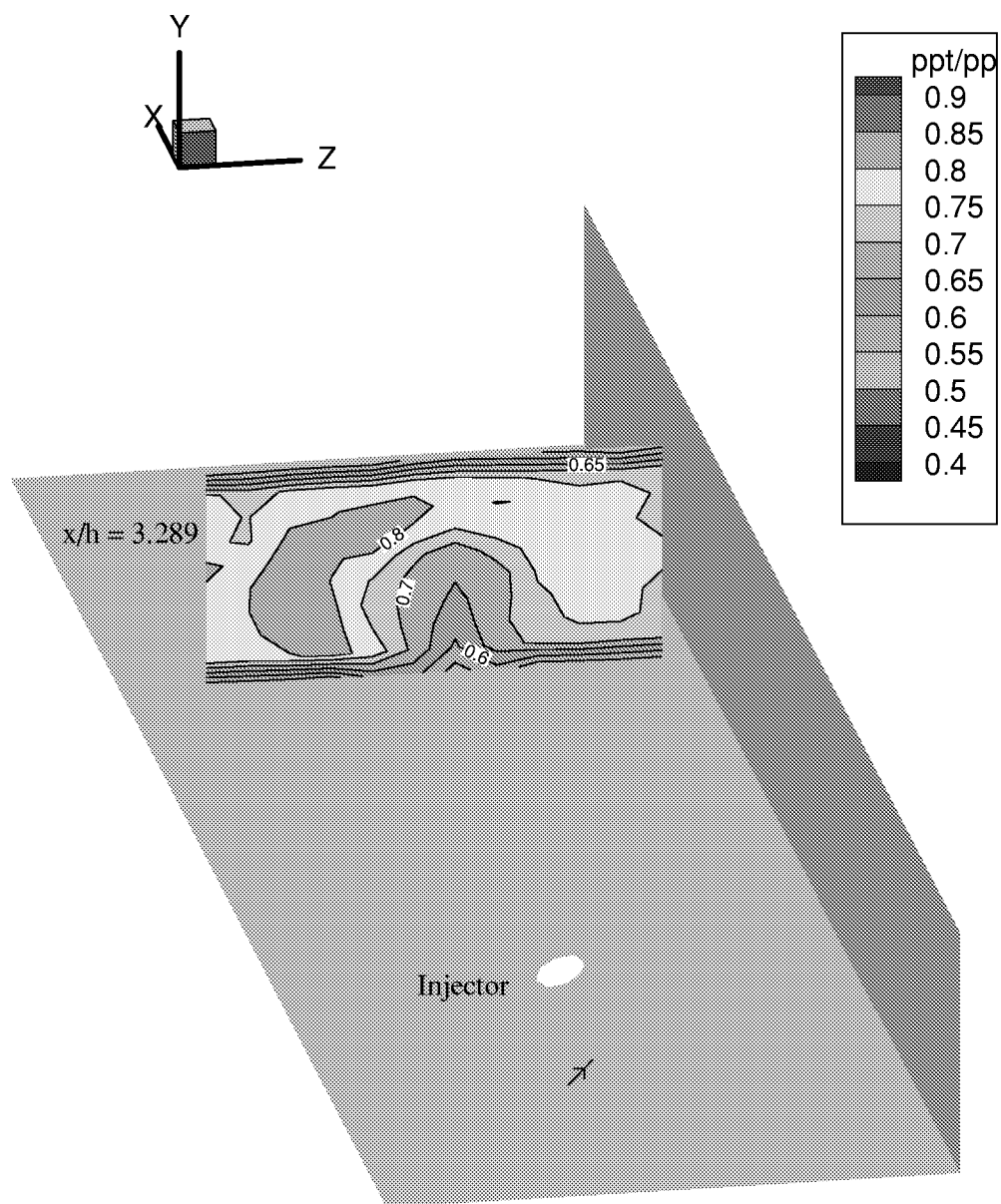
Figure 4-2(b).   Pitot pressures for nonswirl, 25° skew, flush wall injector (N25).

Vortex
sheet

Distributed
vorticity
due to shock

Bow shock

He/O₂
jet

Vortex sheet

(b) Near injection

He/O₂

Vortex rollup
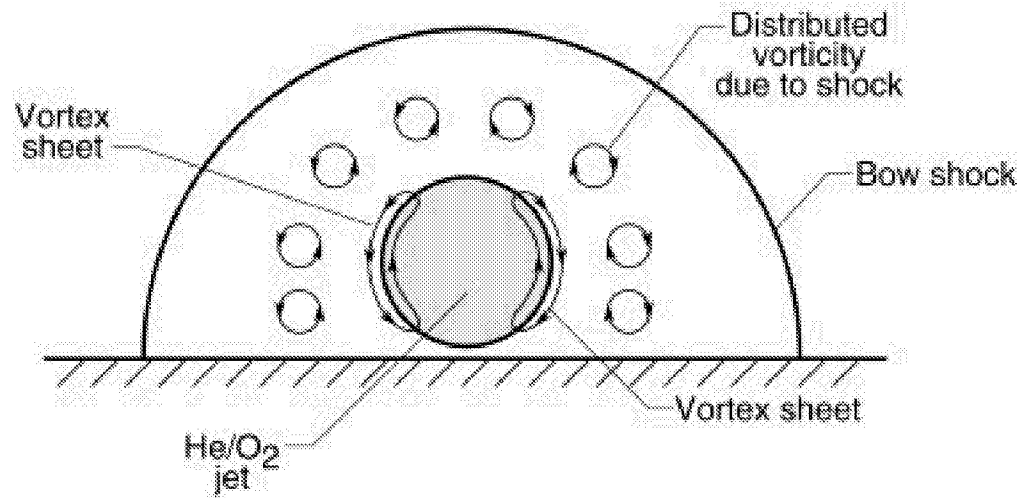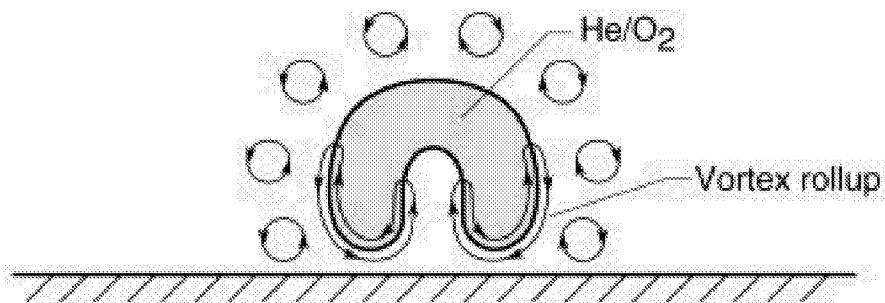
(c) Downstream
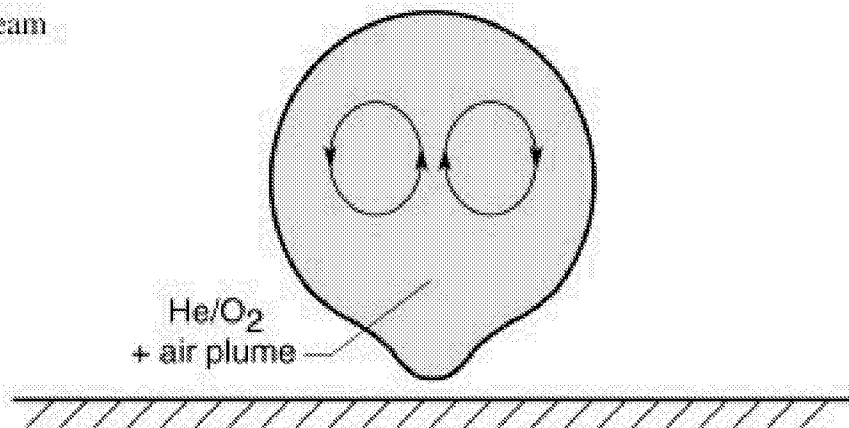
He/O₂
+ air plume

Figure 4-3.   Cross-section view looking upstream for no-swirl, zero skew flush wall injector.
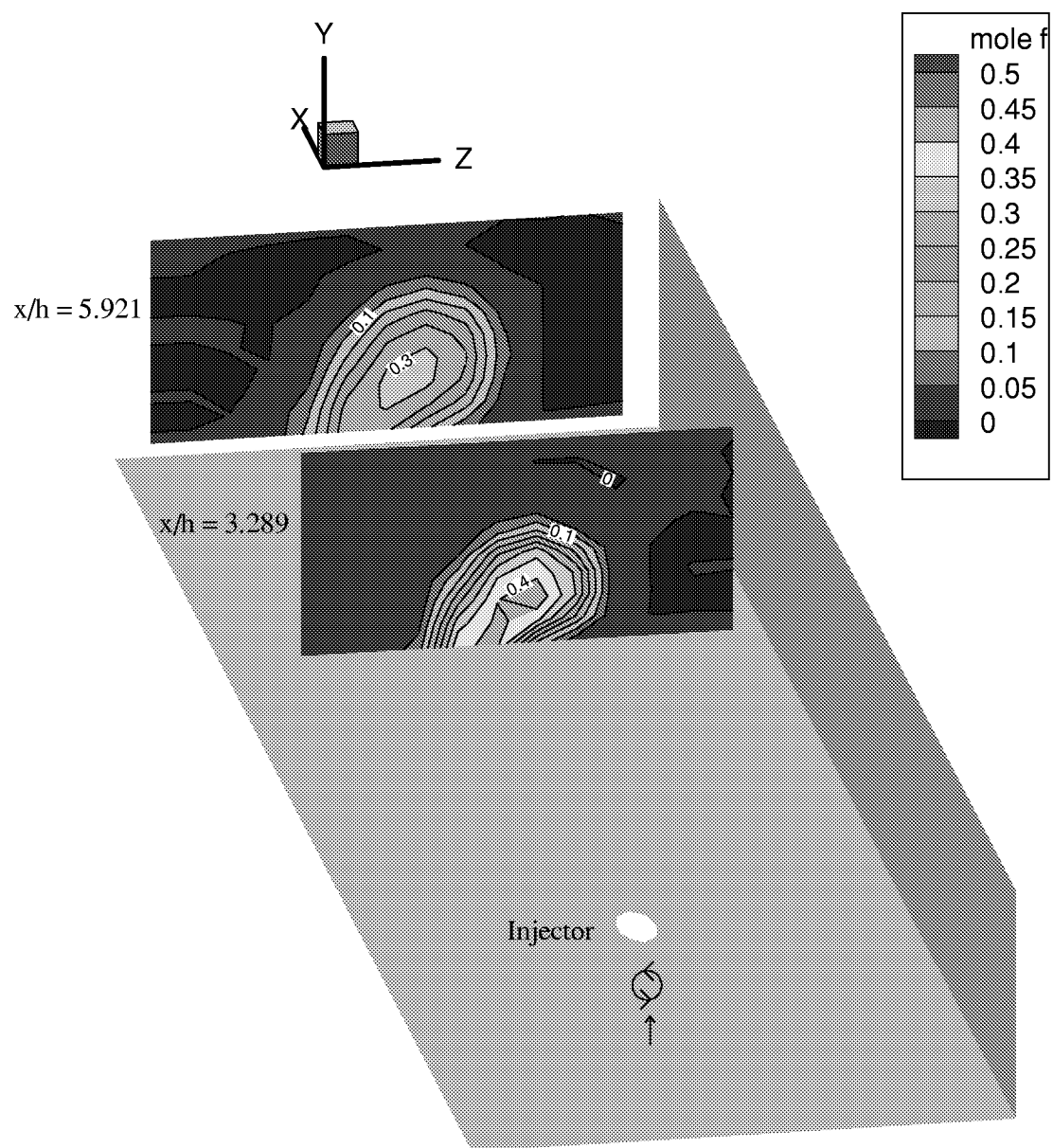
Figure 4-4(a).   He/O_2 mole fractions for swirl, 0° skew, flush wall injector (S0).
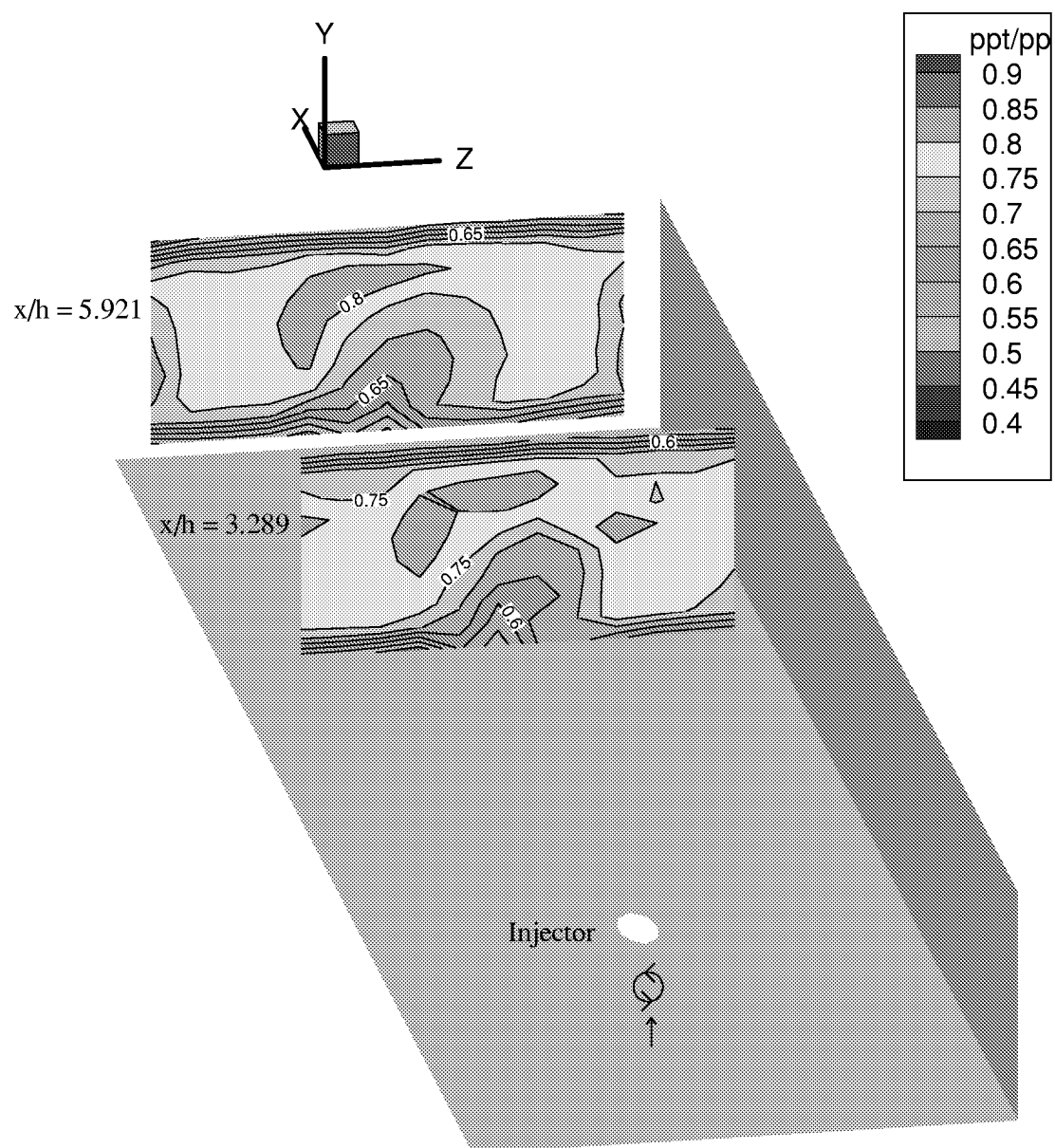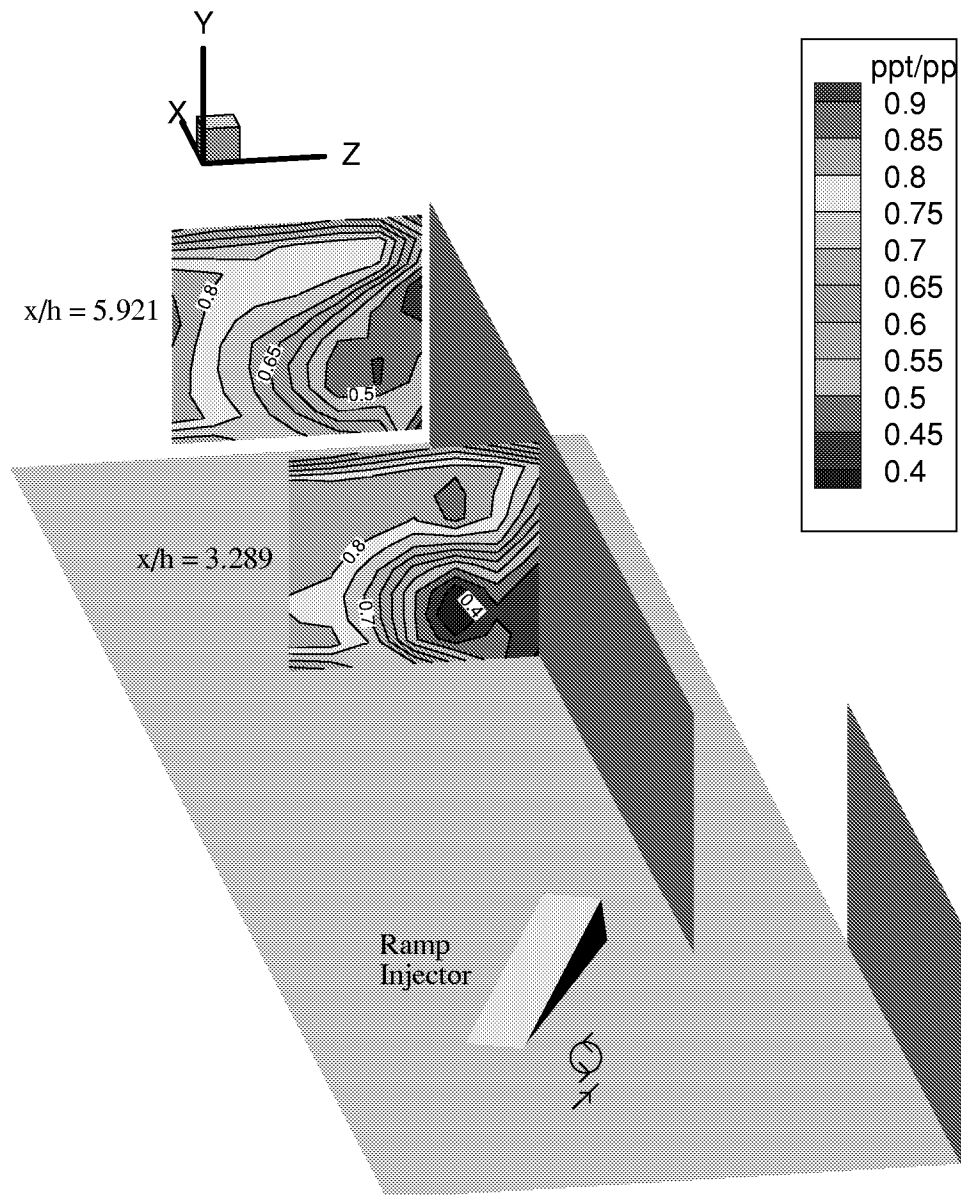
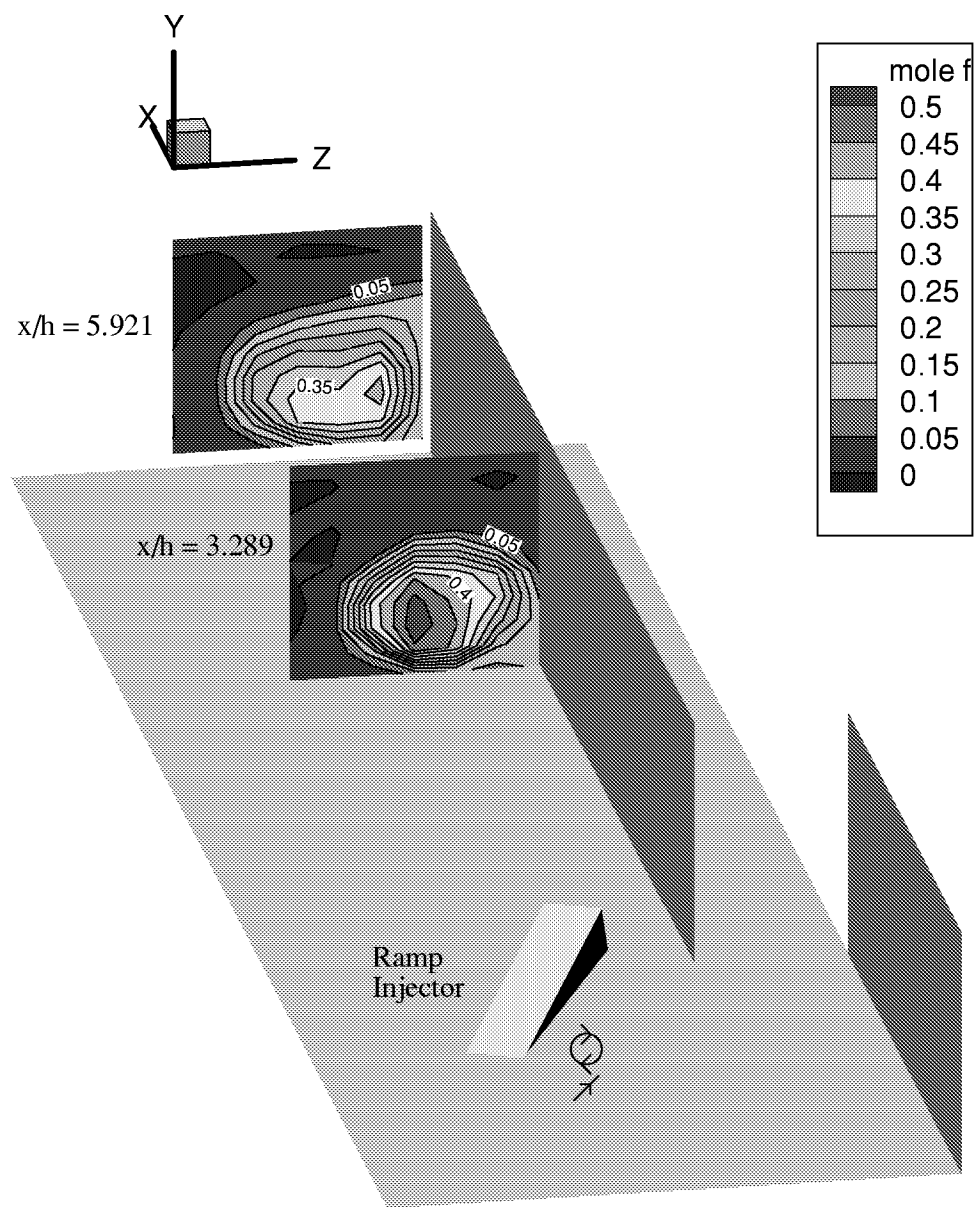Figure 4-4(b).   Pitot pressures for swirl, 0° skew, flush wall injector (S0).
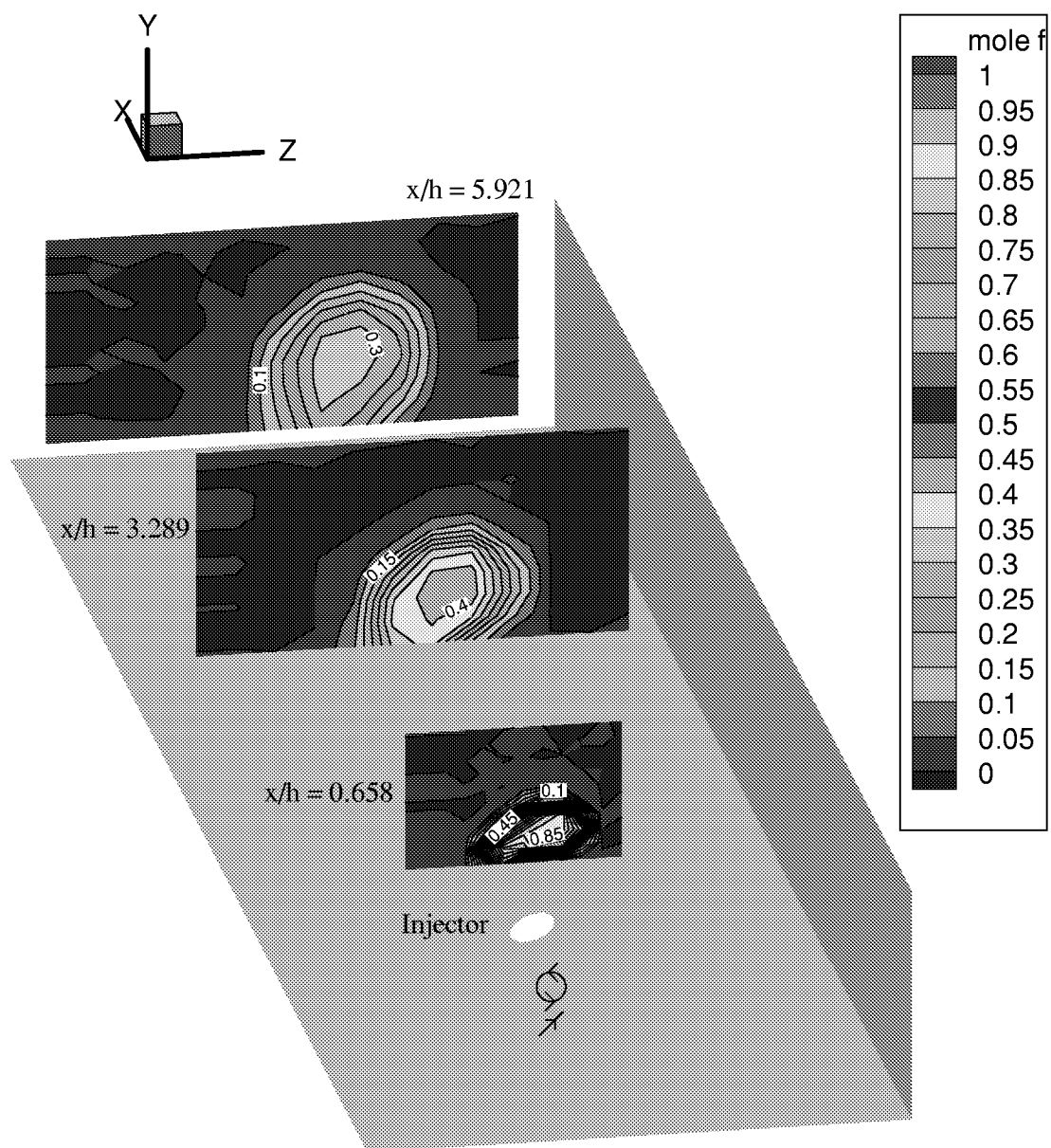
Figure 4-5(a).   He/O$_2$ mole fractions for swirl, 25° skew, flush wall injector (S25).
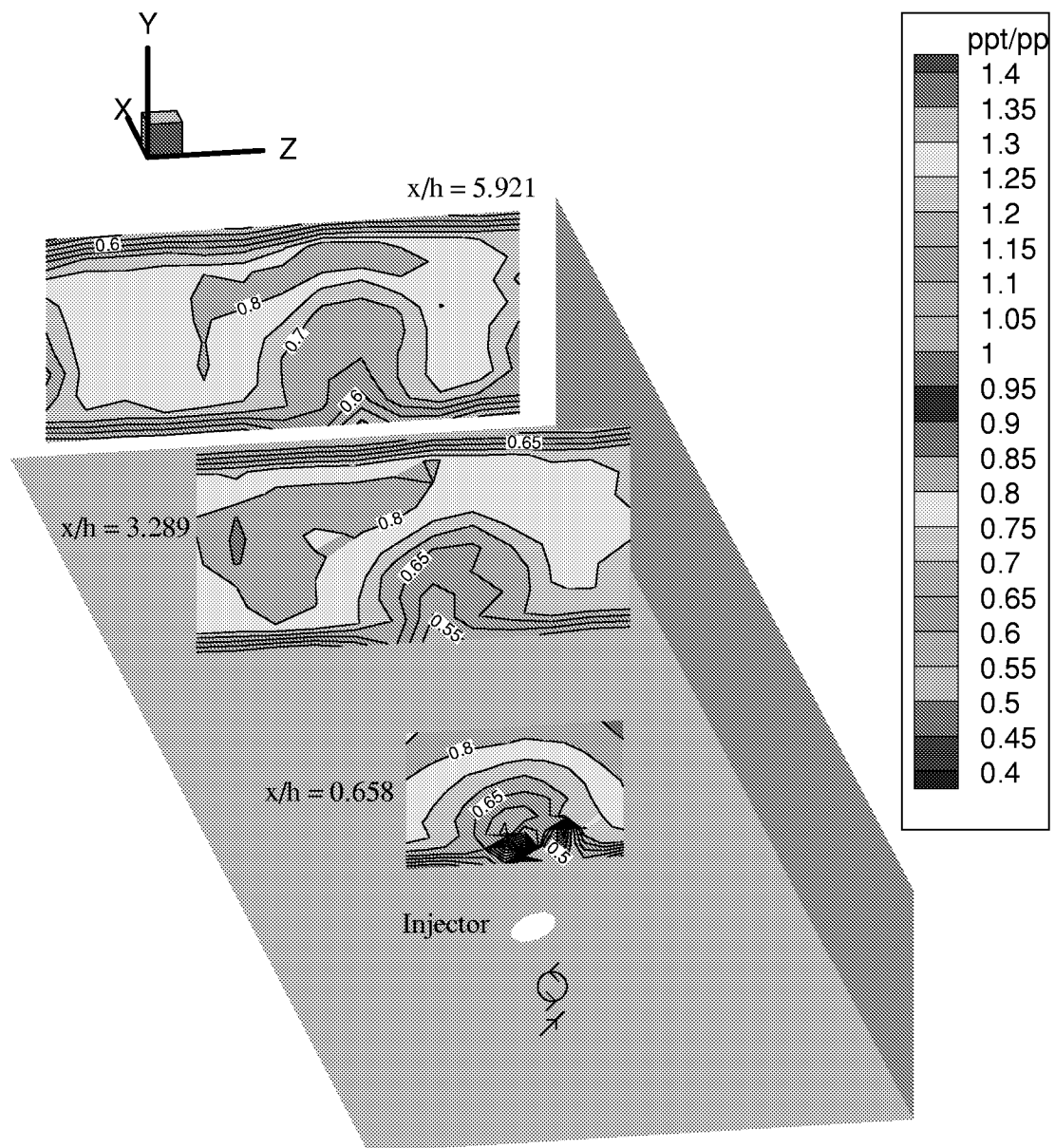
Figure 4-5(b). Pitot pressures for swirl, 25° skew, flush wall injector (S25).
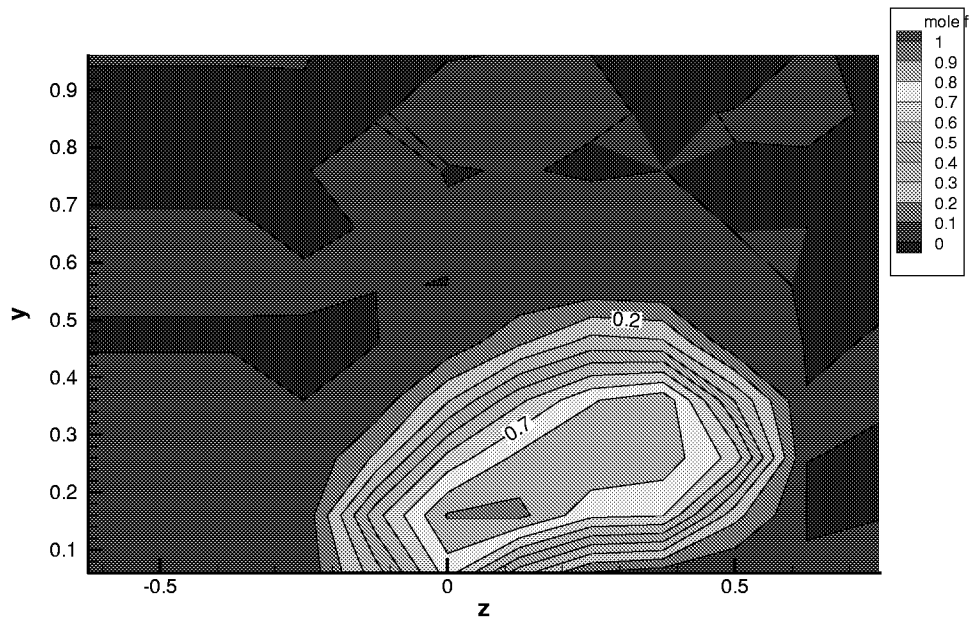
Figure 4-5(c).   Close-up of $x/h = 0.658$ mole fractions of S25 case.
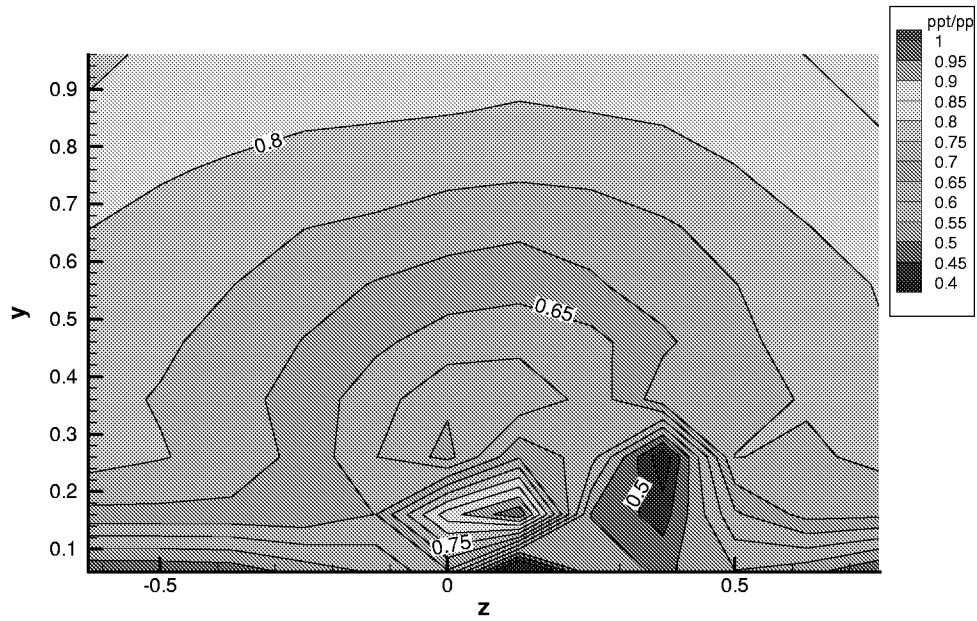
Figure 4-5(d).   Close-up of $x/h = 0.658$ Pitot pressures of S25 case.
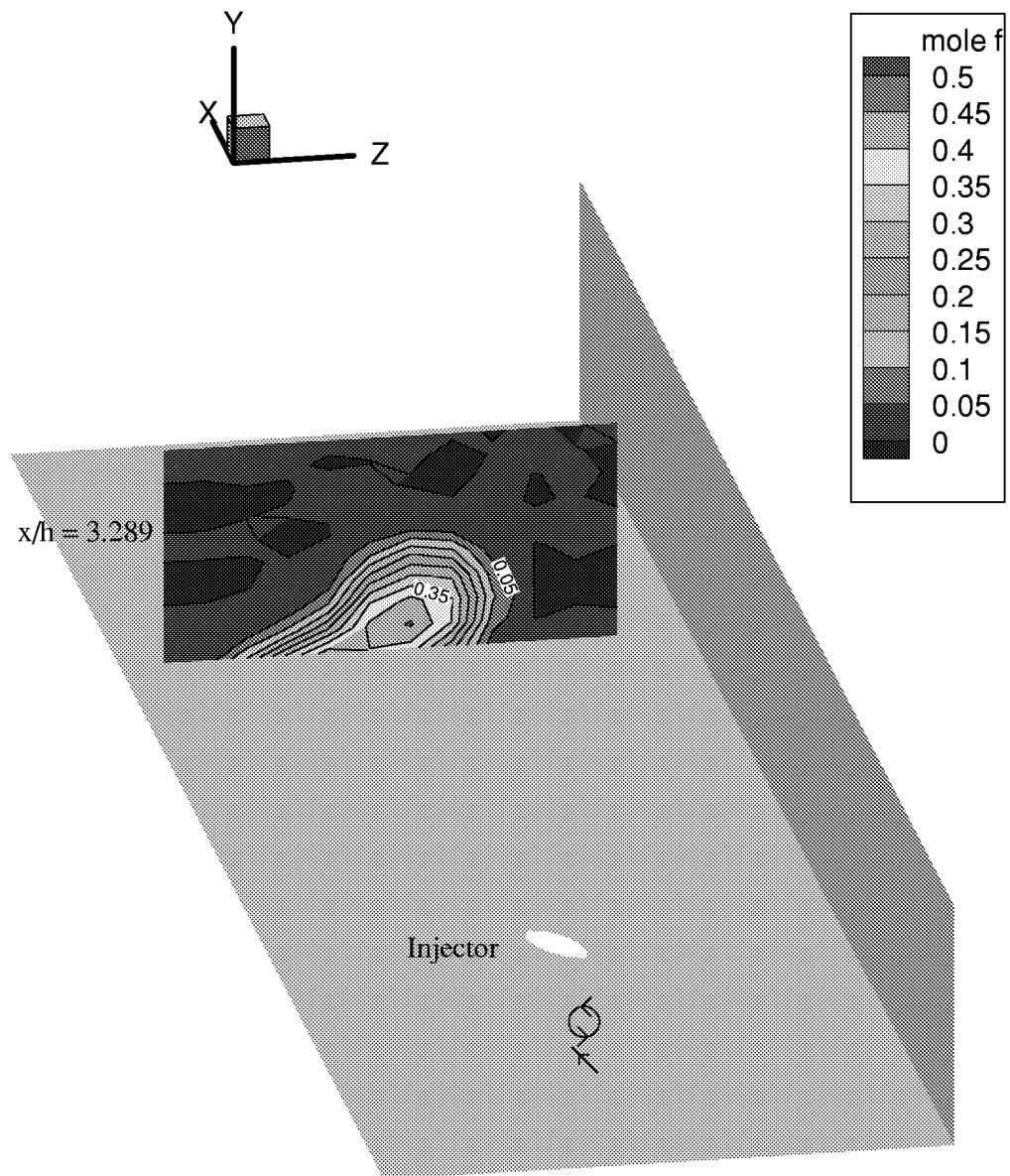
Figure 4-6(a). He/O$_2$ mole fractions for swirl, -25° skew, flush wall injector (S-25).
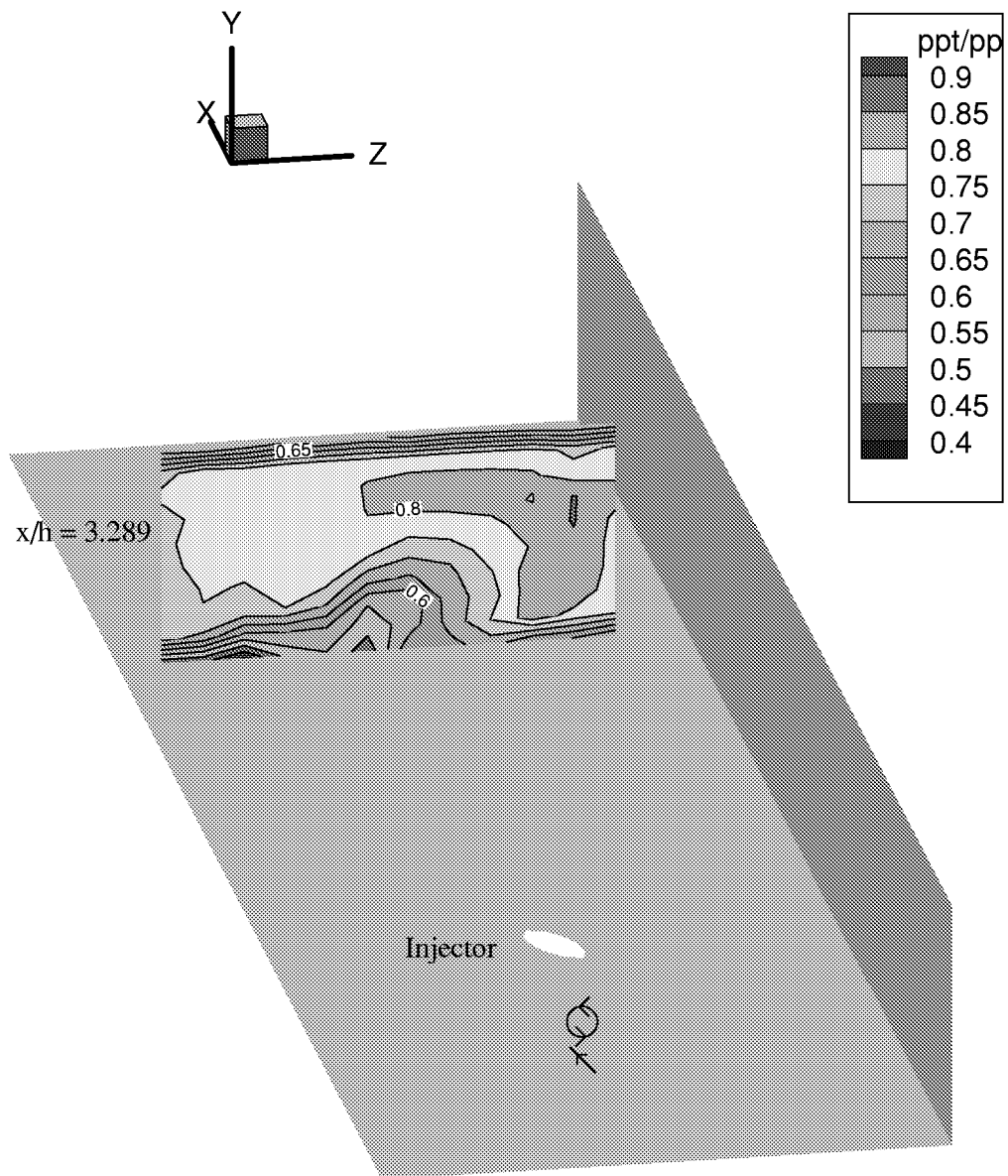
Figure 4-6(b).   Pitot pressures for swirl, -25° skew, flush wall injector (S-25).

(a) At injection

Swirl

Distributed
vorticity
due to shock

Bow shock

He/O$_2$
jet

Vortex sheet
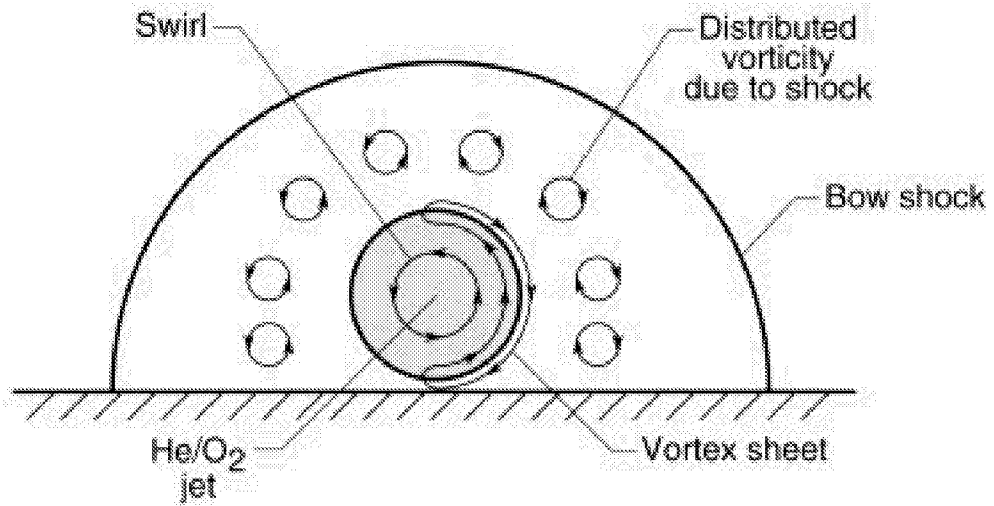
(b) Near injection
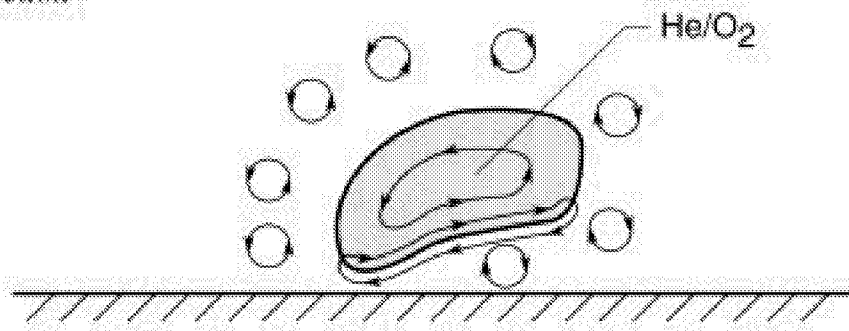
He/O$_2$

(c) Downstream
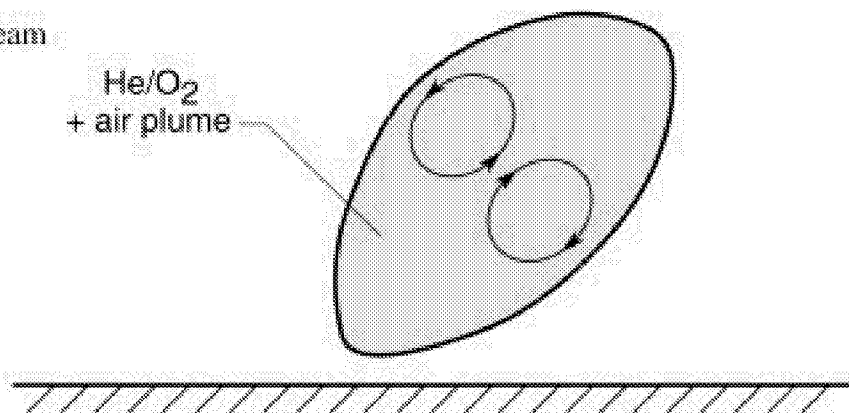
He/O$_2$
+ air plume

Figure 4-7.   Cross-section view looking upstream for swirl, zero skew flush wall injector.

96
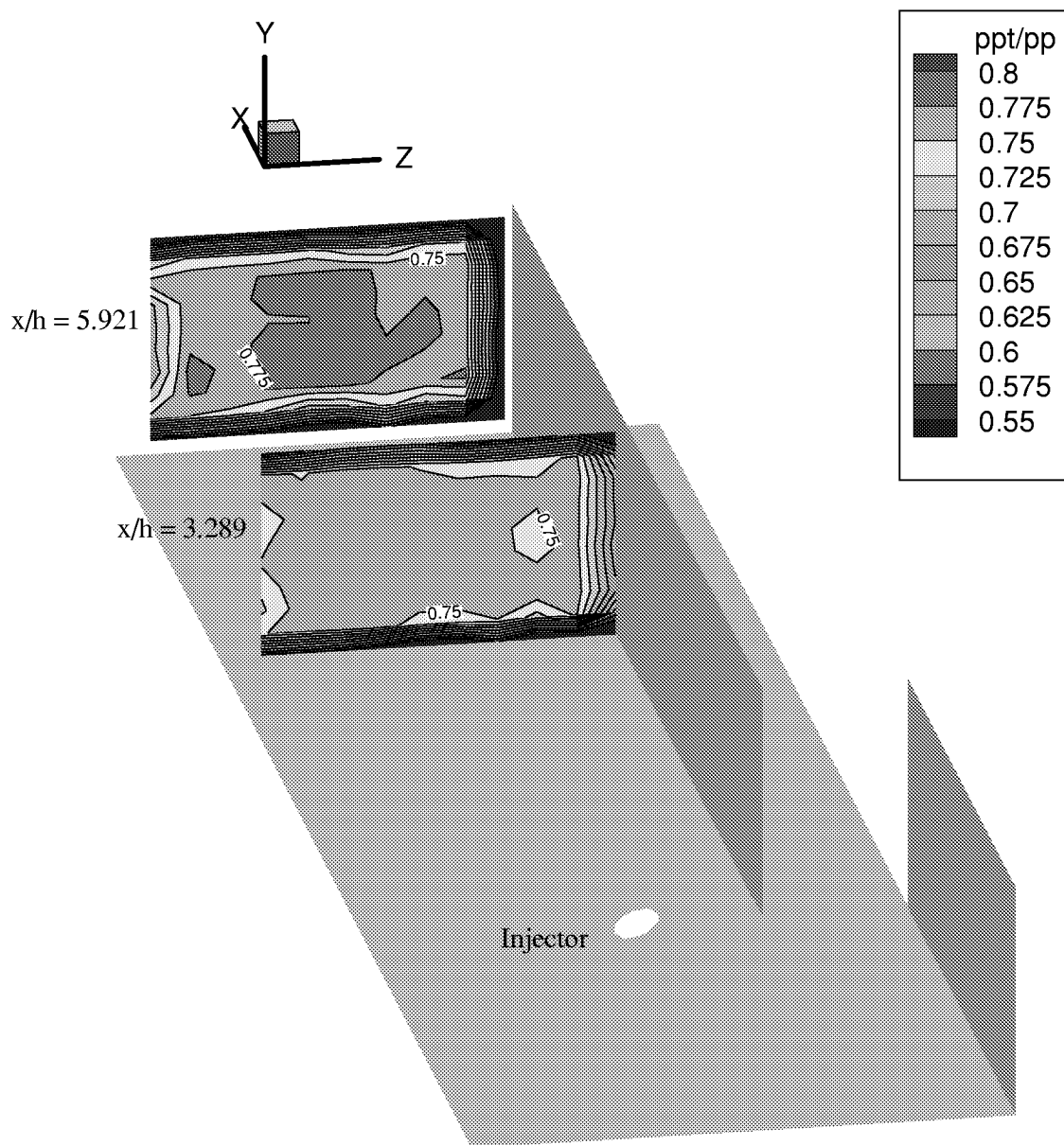
Figure 4-8. Pitot pressures for no injection, 25° skew, flush wall injector, offset wall (S25Xn).
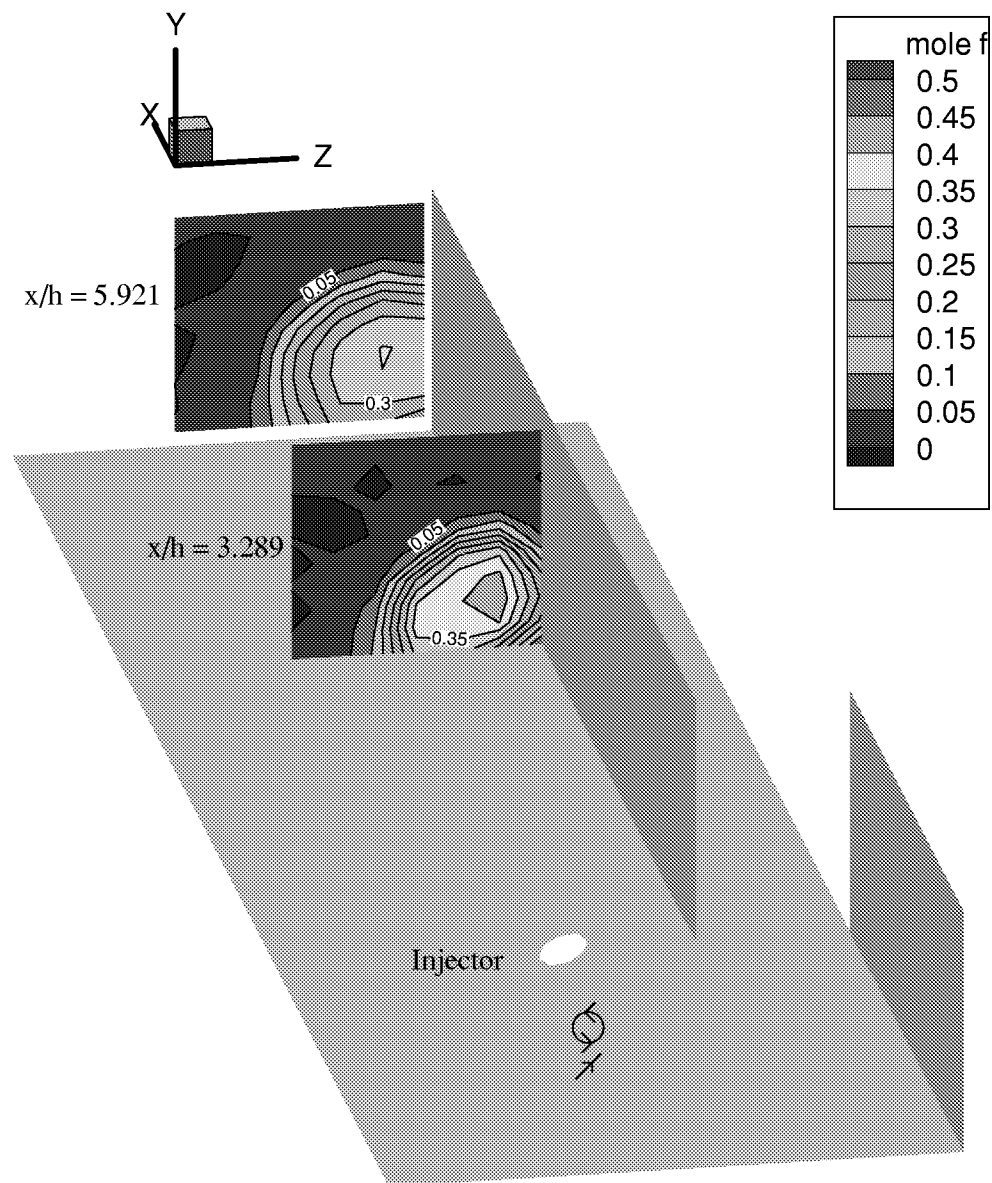
Figure 4-9(a).   He/O$_2$ mole fractions for swirl, 25° skew, flush wall injector, offset wall (S25X).
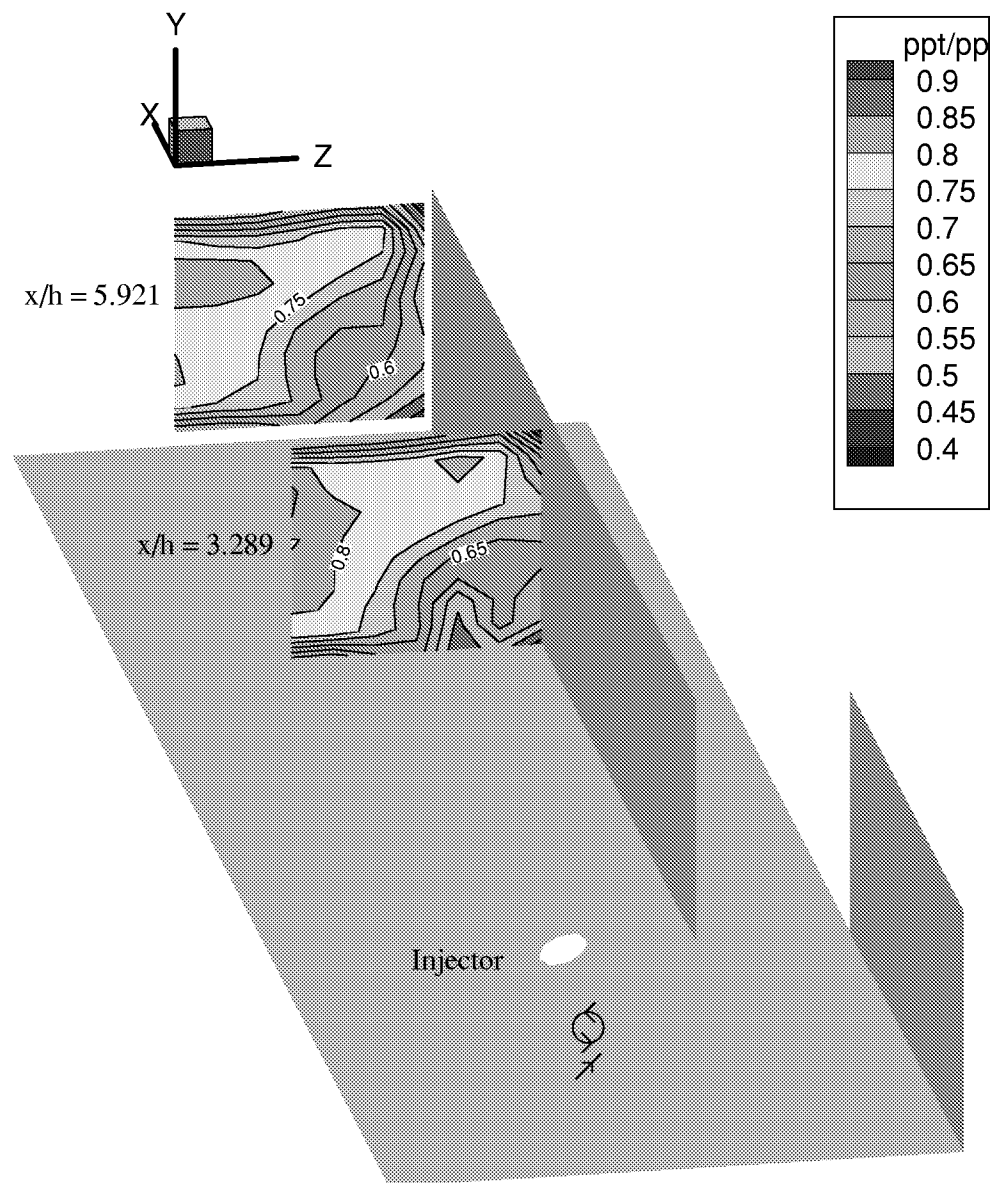
Figure 4-9(b). Pitot pressures for swirl, 25° skew, flush wall injector, offset wall (S25X).
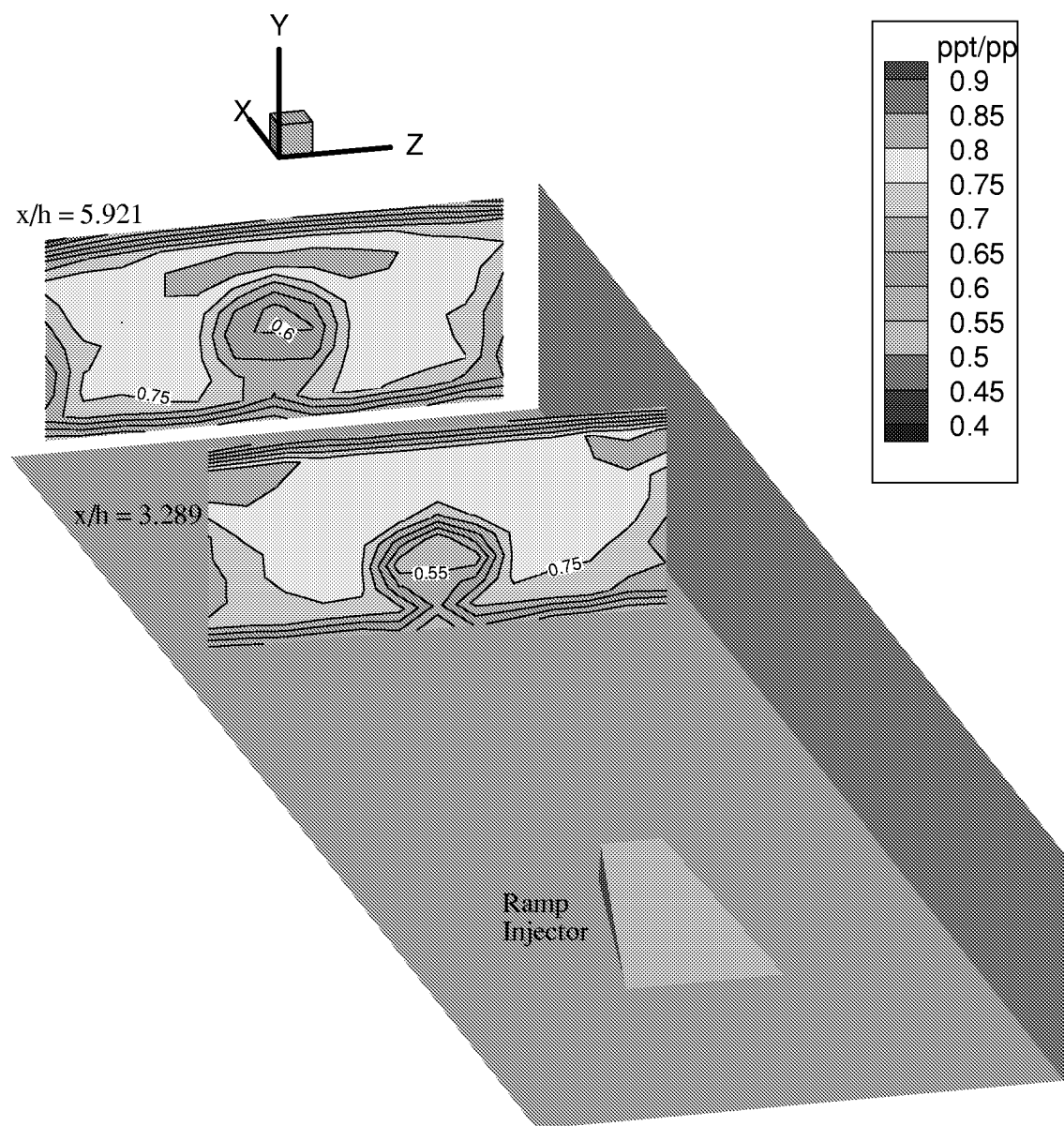
Figure 4-10.   Pitot pressures for no injection, 0° skew, swept ramp injector (N0S).
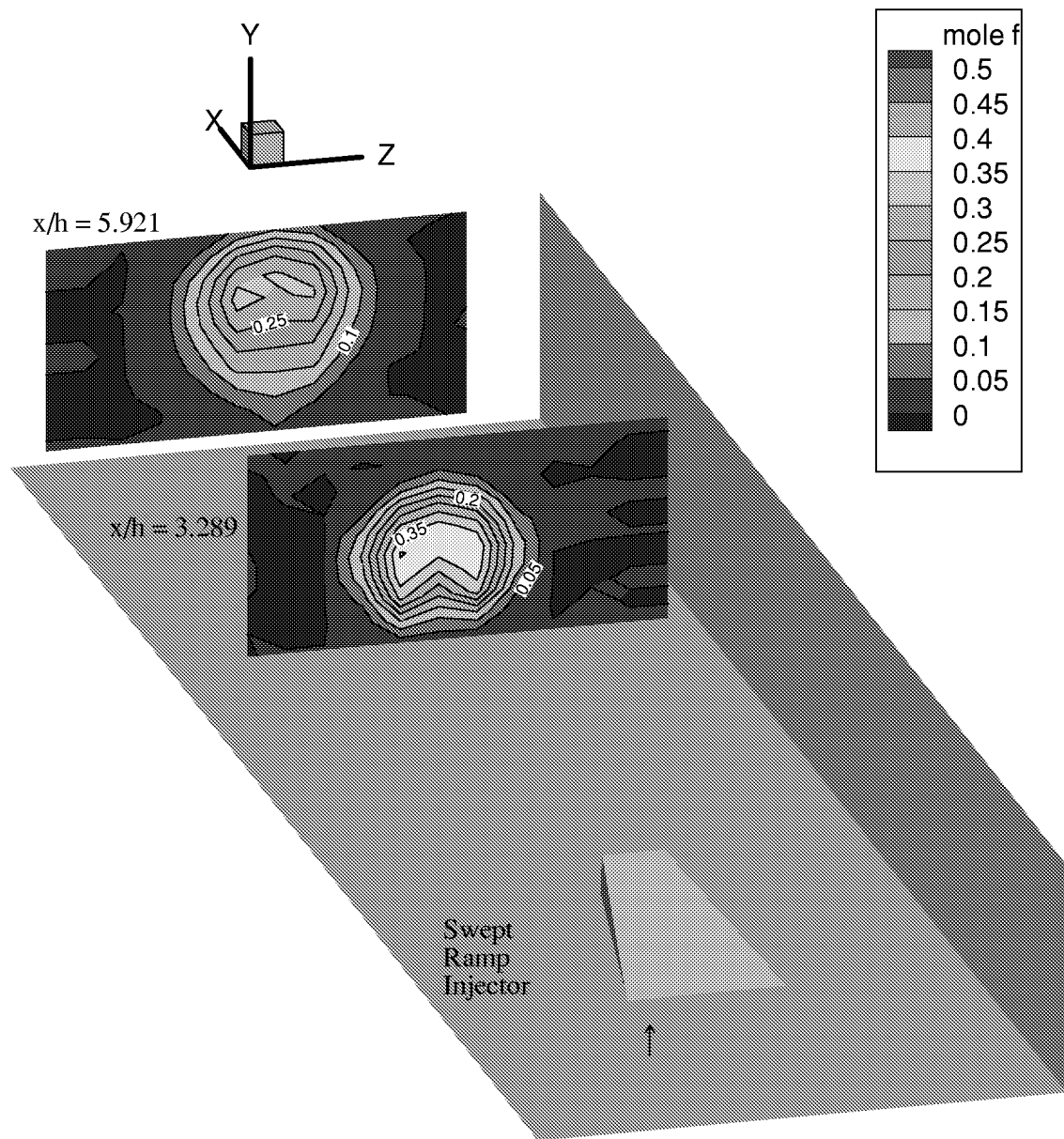
Figure 4-11(a). He/O$_2$ mole fractions for nonswirl, 0° skew, swept ramp injector (N0S).
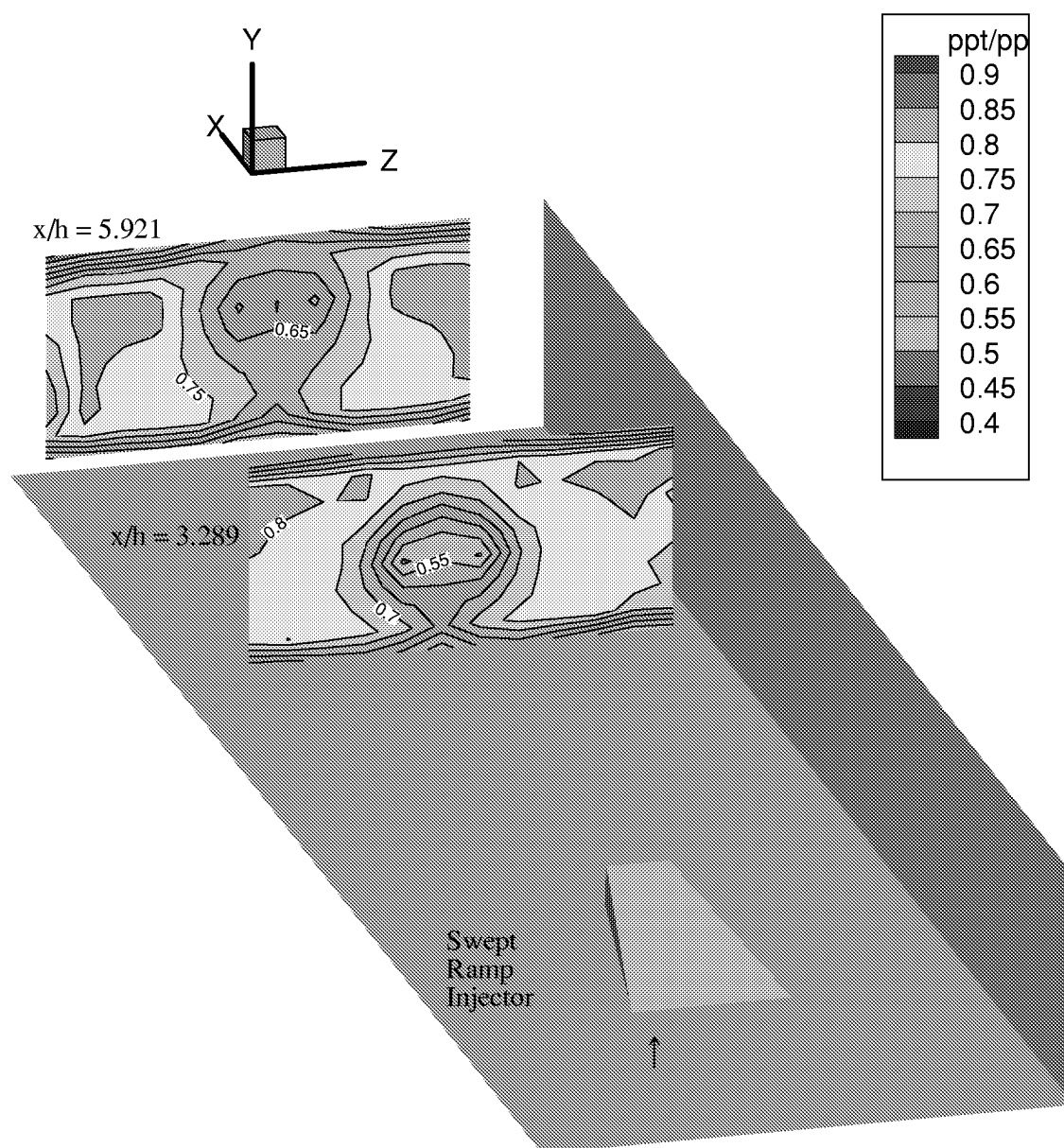
Figure 4-11(b). Pitot pressures for nonswirl, 0° skew, swept ramp injector (N0S).
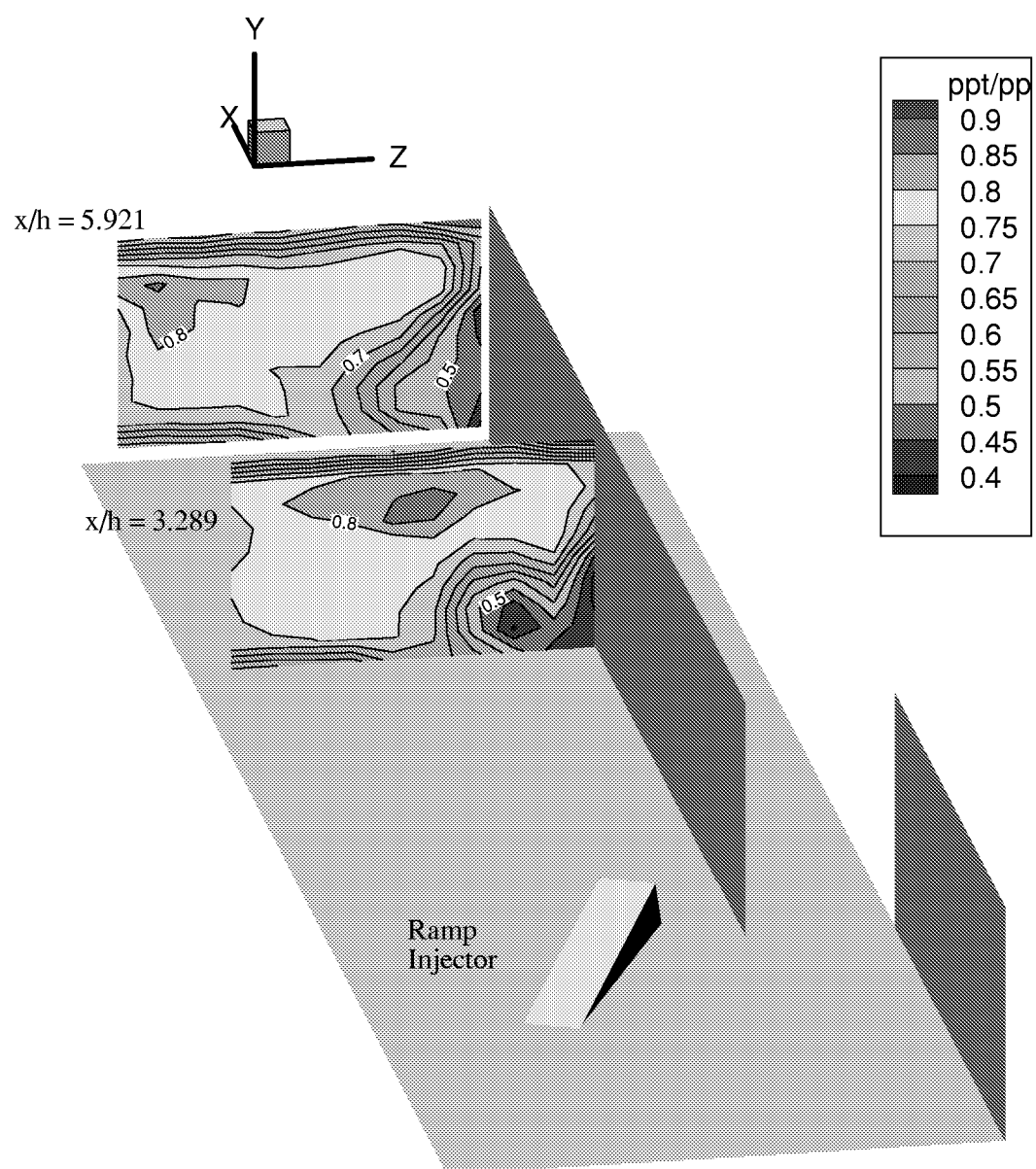
Figure 4-12.   Pitot pressures for no injection, -25° skew, ramp injector, offset wall (S-25R).
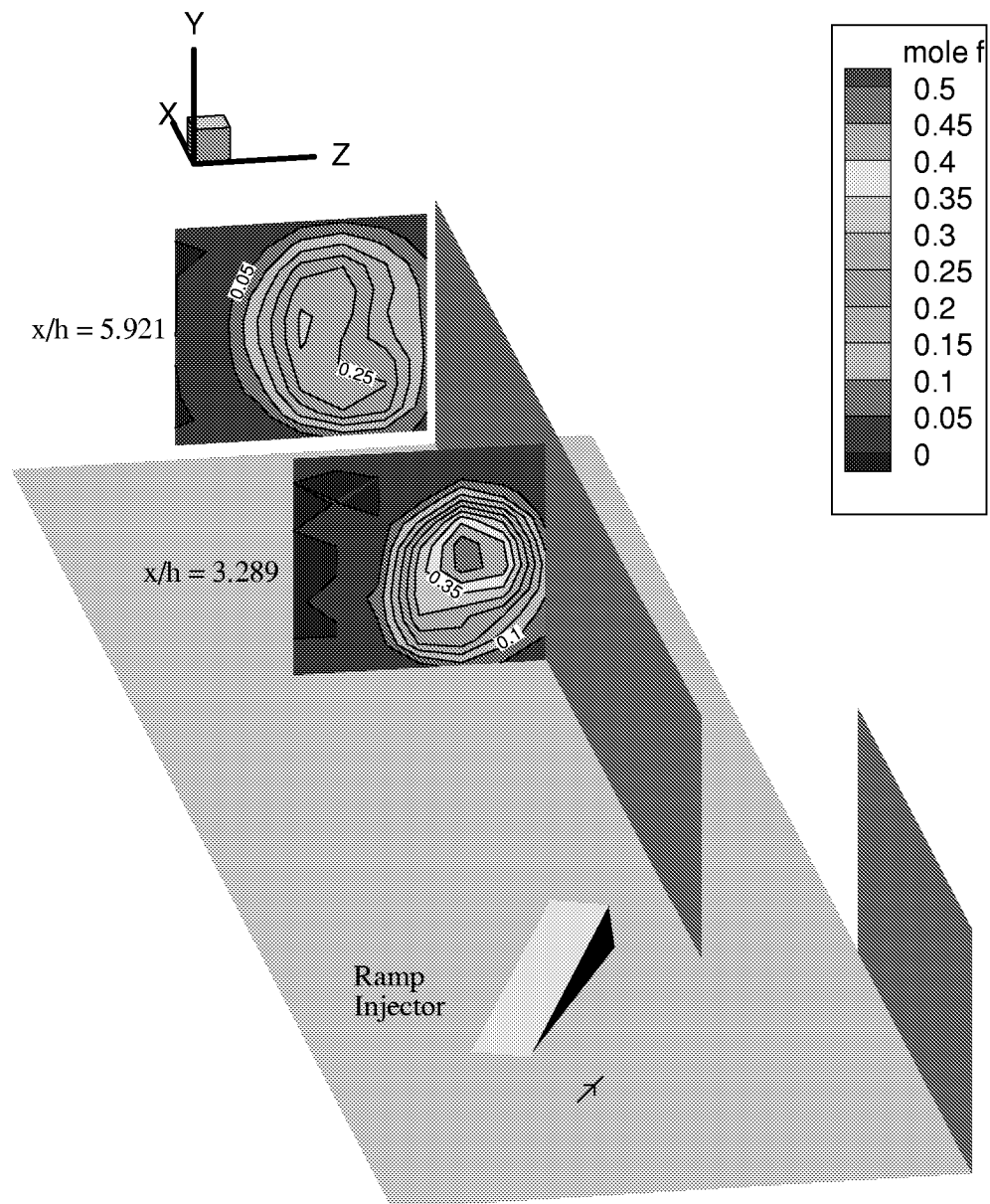
Figure 4-13(a). He/O_2 mole fractions for nonswirl, 25° skew, ramp injector, offset wall (N25R).
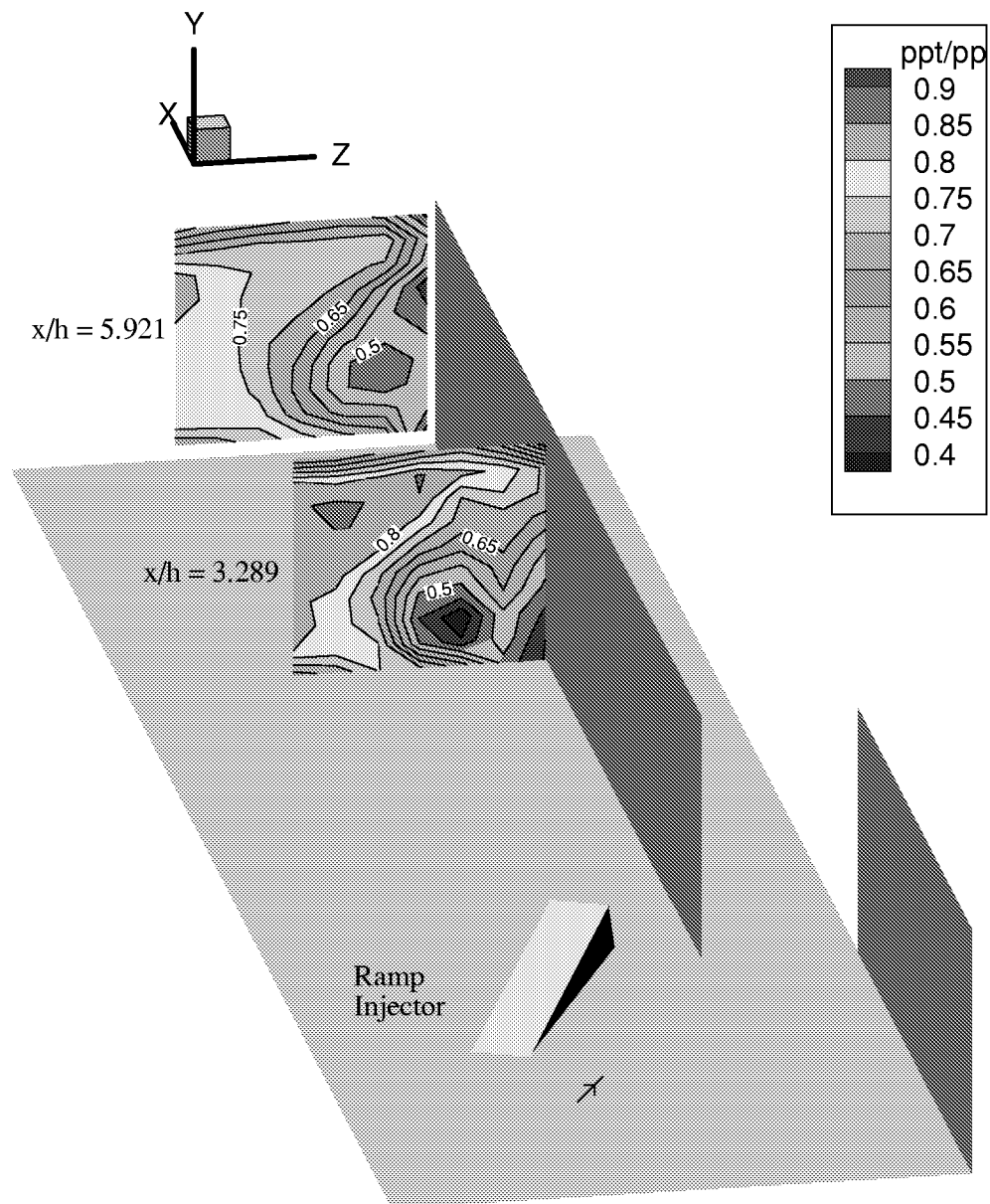
Figure 4-13(b).   Pitot pressures for nonswirl, 25° skew, ramp injector, offset wall (N25R).
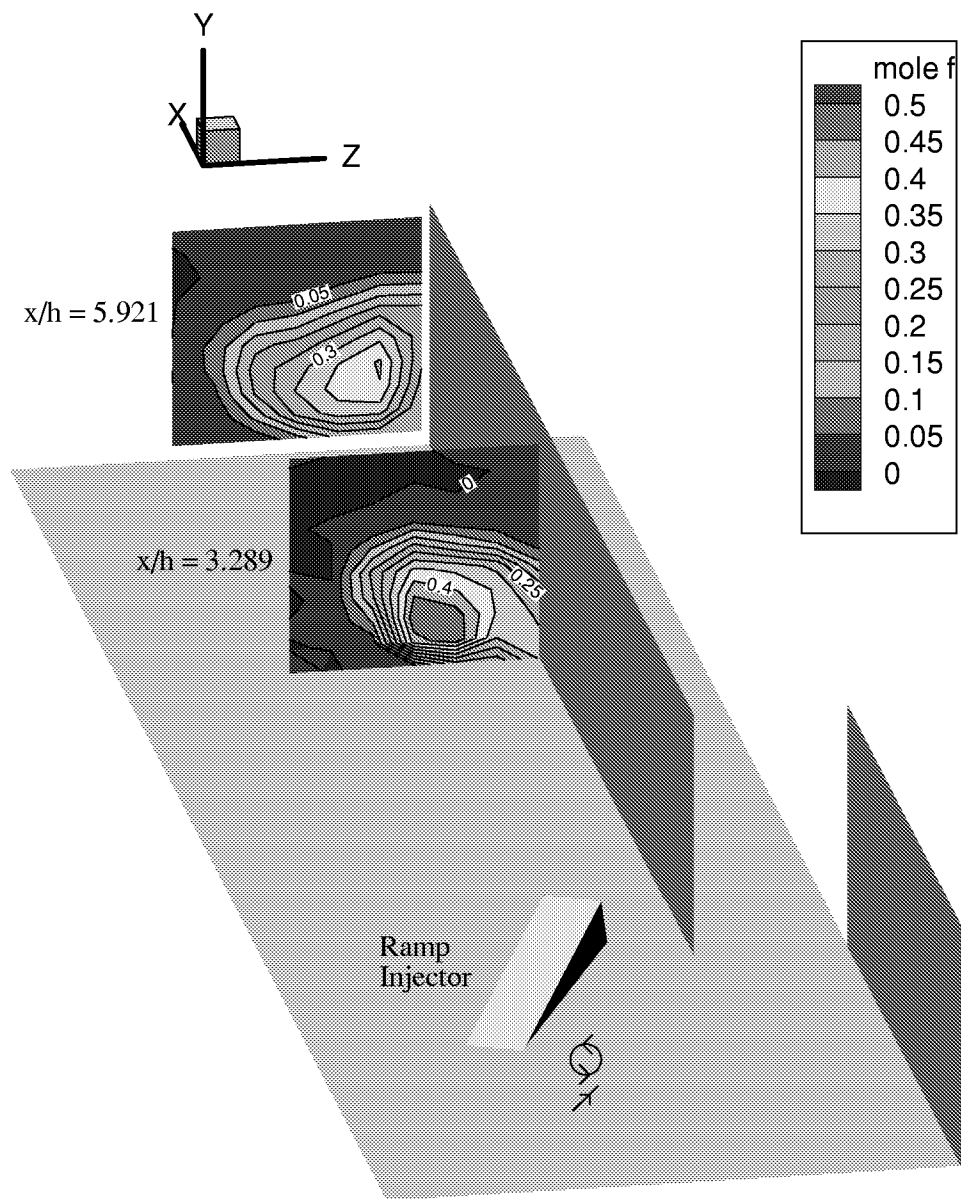
Figure 4-14(a). He/O_2 mole Fractions for swirl, 25° skew, ramp injector, offset wall (S25R).

Figure 4-14(b).   Pitot pressures for swirl, 25° skew, ramp injector, offset wall (S25R).

Figure 4-15(a).   He/O$_2$ mole fractions for swirl, -25° skew, ramp injector, offset wall (S-25R).
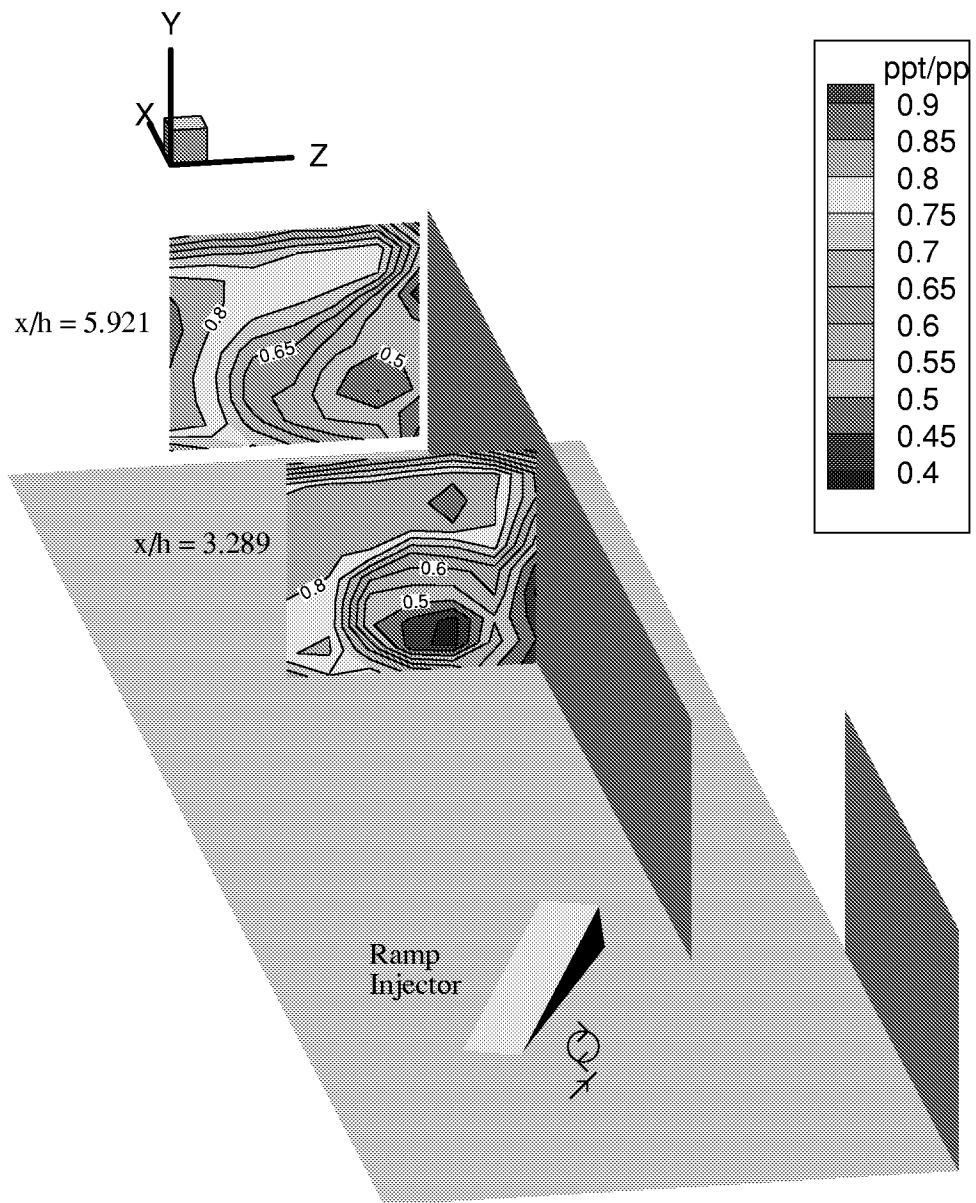
Figure 4-15(b).   Pitot pressures for swirl, -25° skew, ramp injector, offset wall (S-25R).
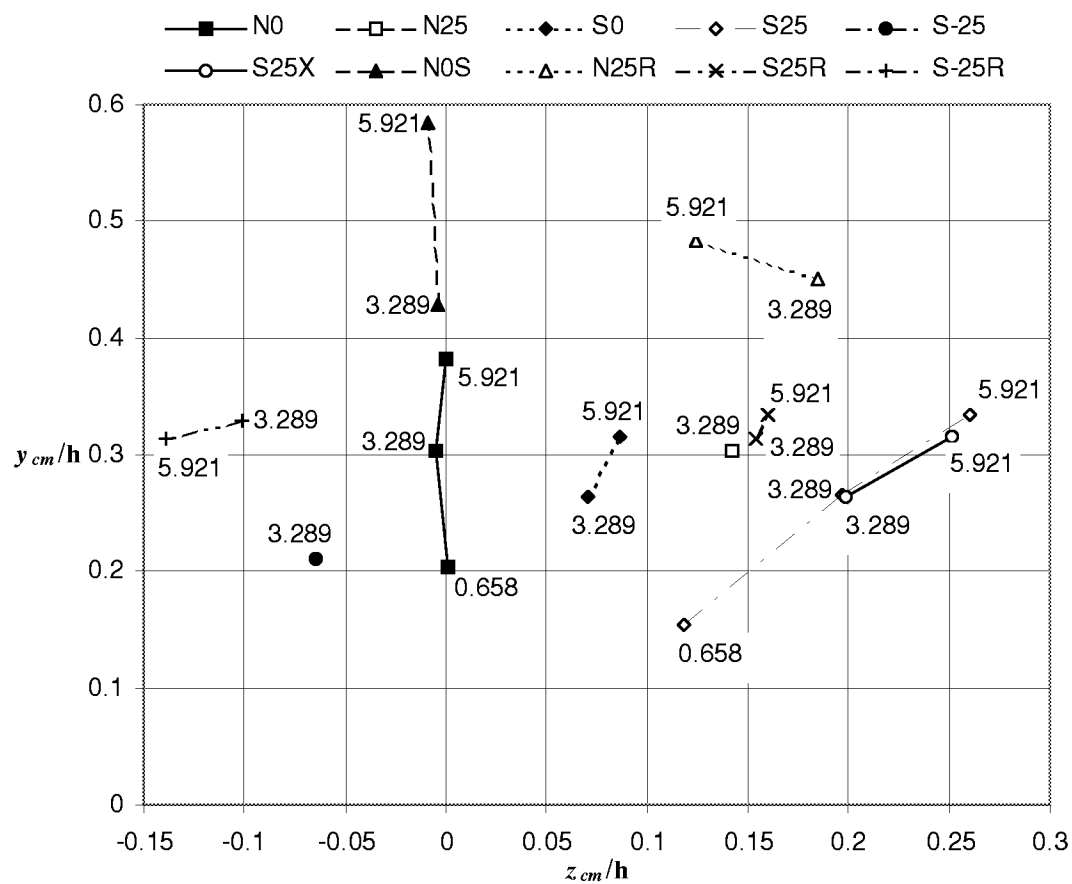
Figure 4-16.   Motion of plume center of mass (z_{cm}, y_{cm}).
(x/h location labeled for each point)
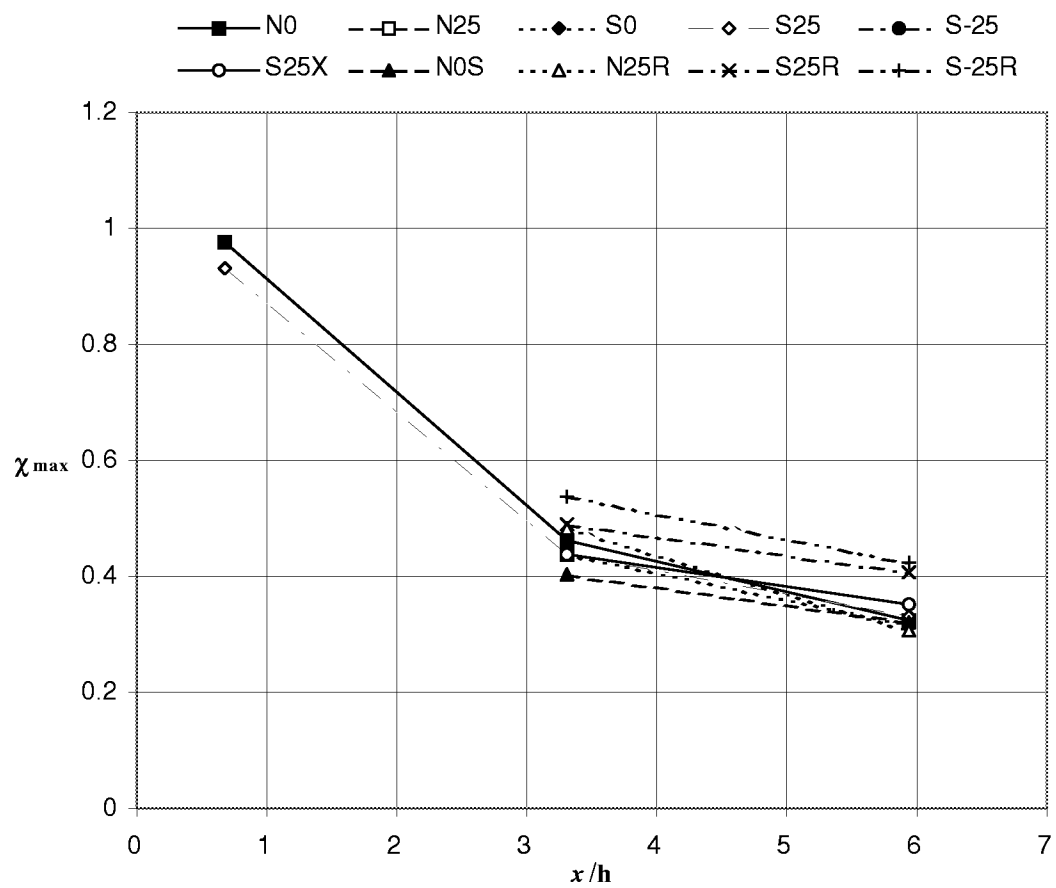
Figure 4-17.   Peak He/O_2 mole fractions.
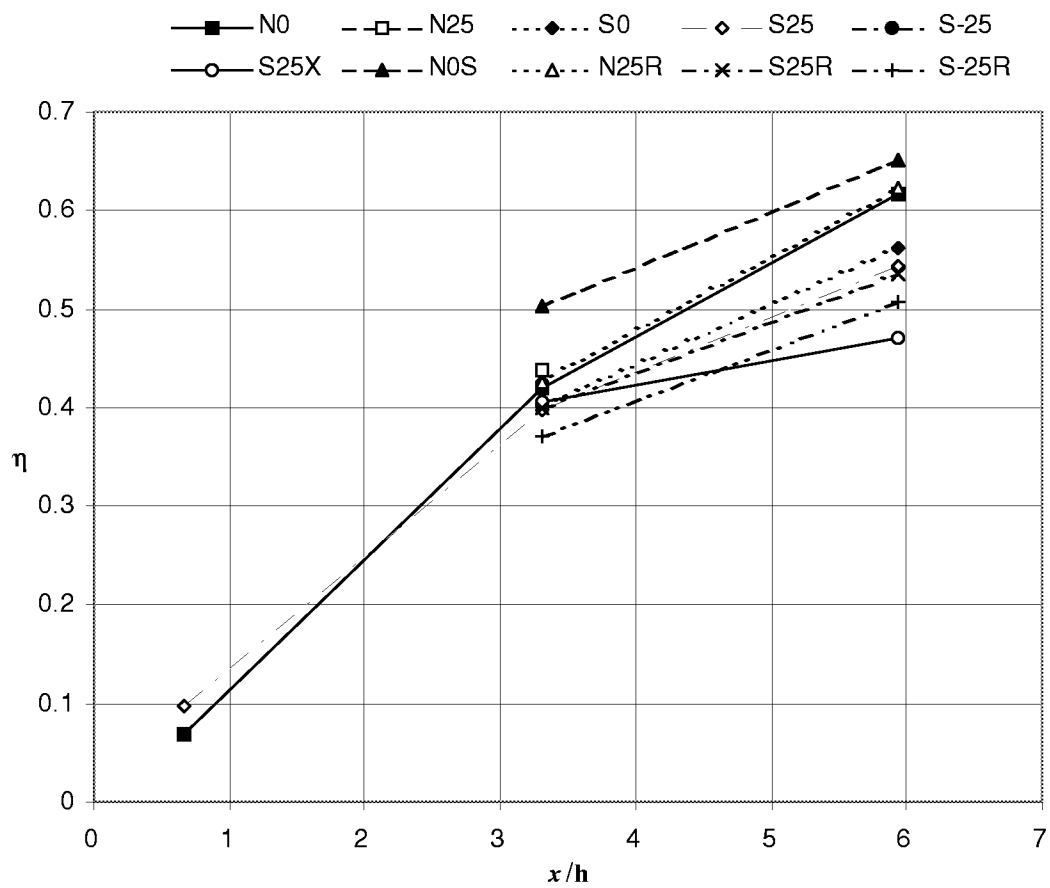
Figure 4-18.   Mixing efficiency.
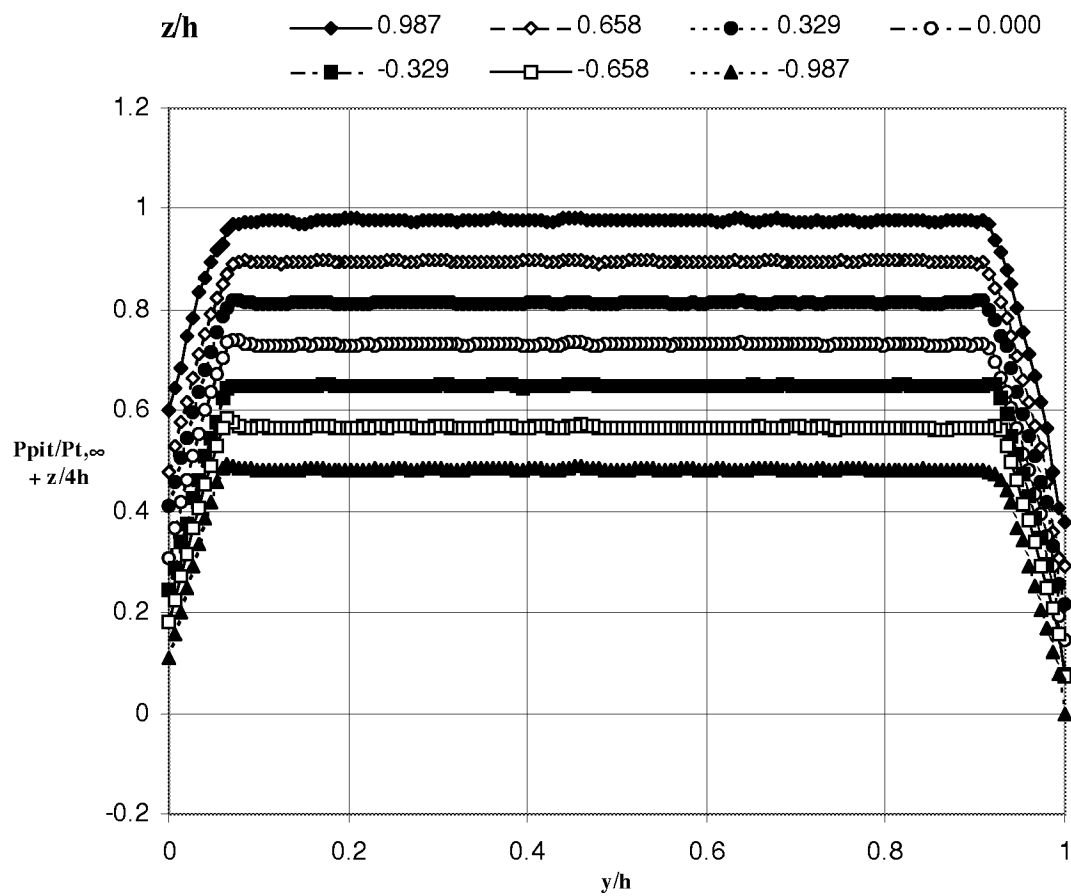
Figure A-1.   Exit survey Pitot pressure.
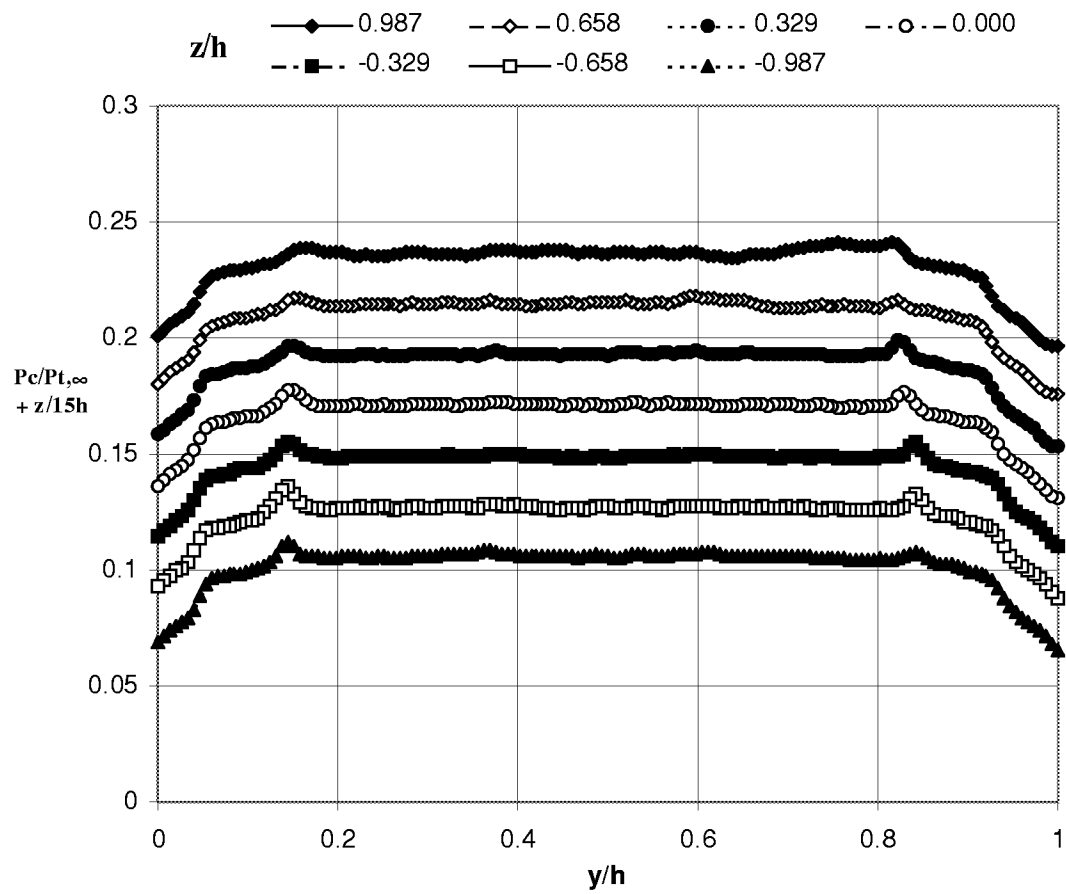
Figure A-2. Exit survey cone static pressure.

Injection Wall

Opposite Wall
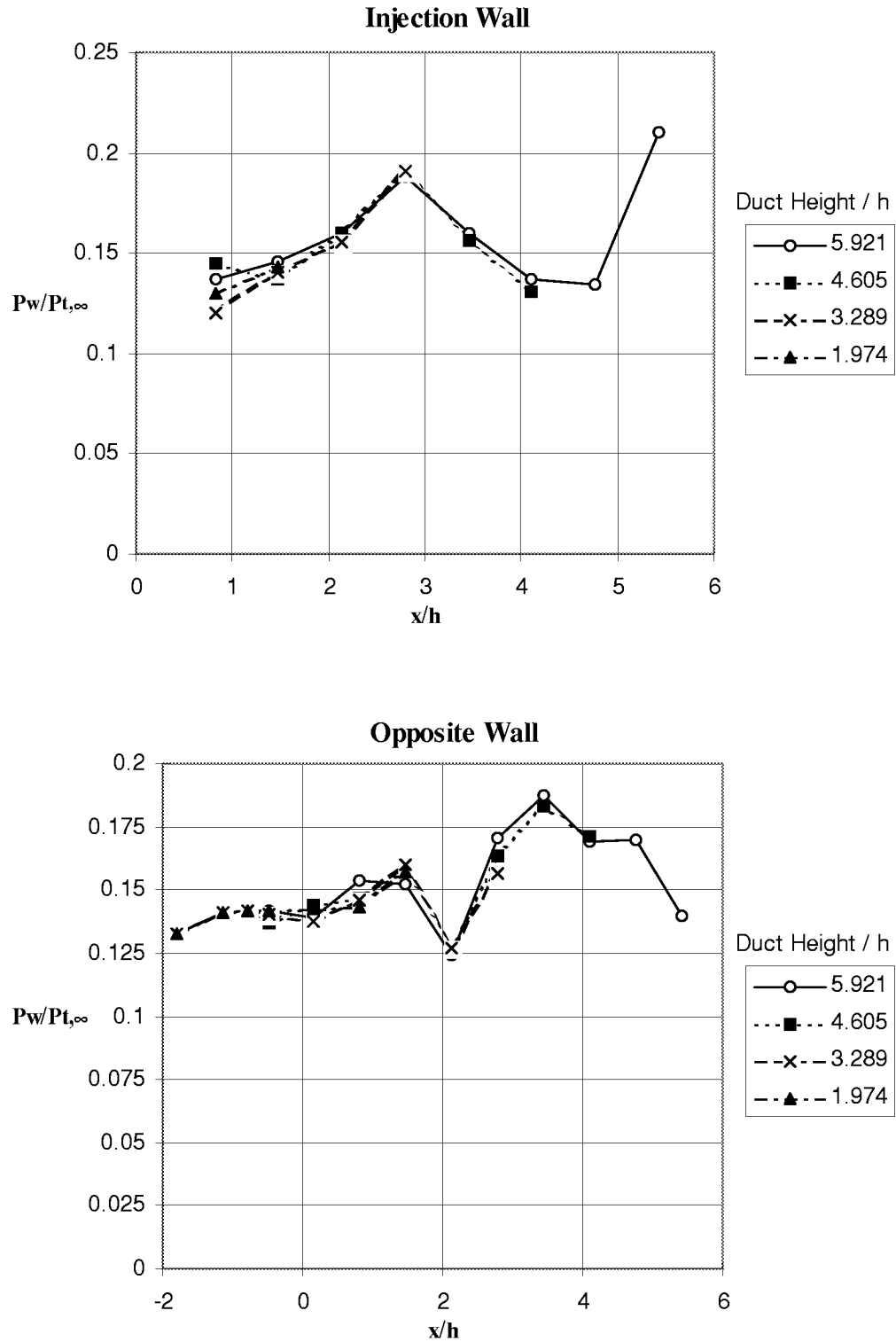
Figure C-1. Nonswirl, 0 deg. skew, flush wall injector wall pressures.

Injection Wall

Opposite Wall
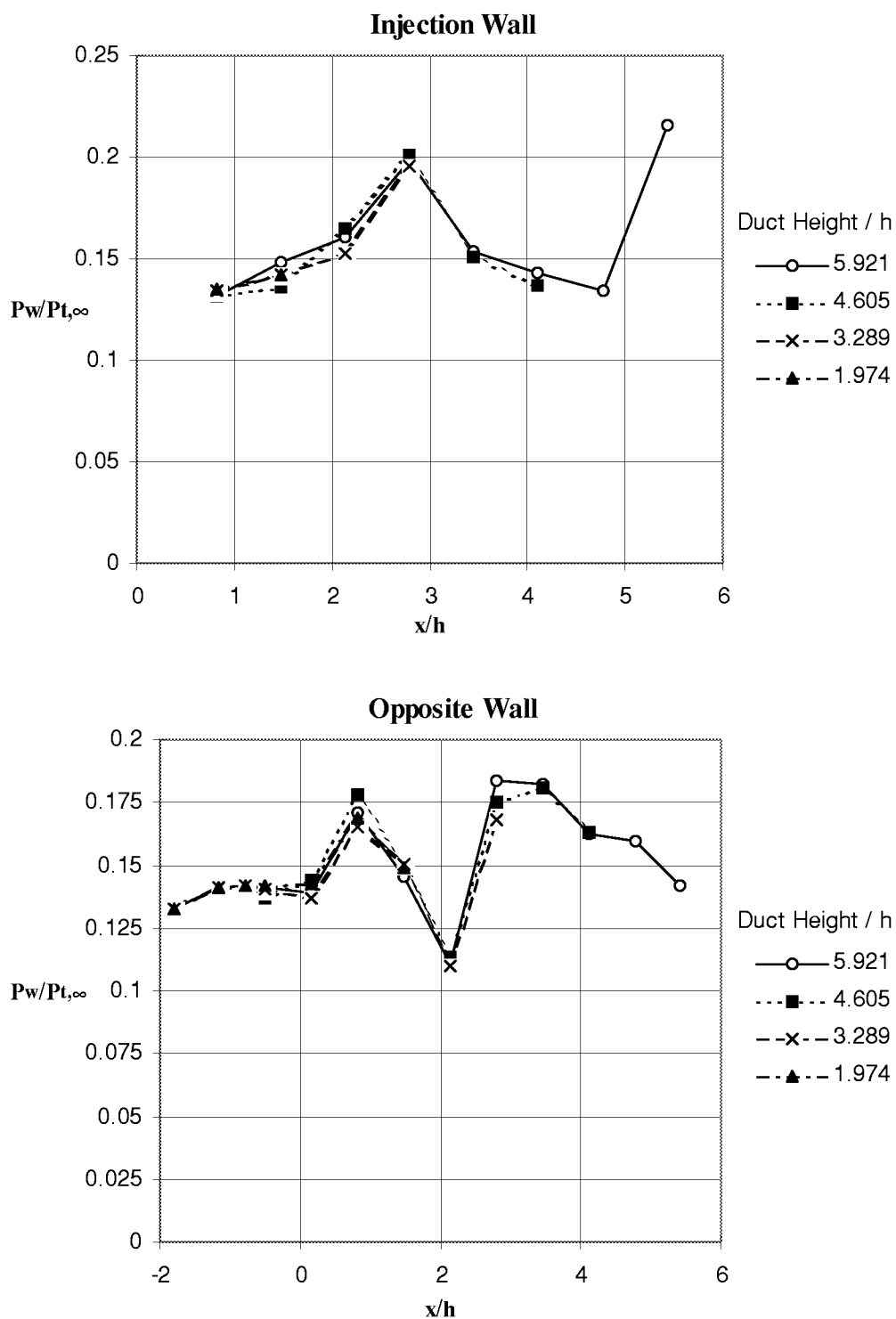
Figure C-2. Swirl, 25 deg. skew, flush wall injector wall pressures.
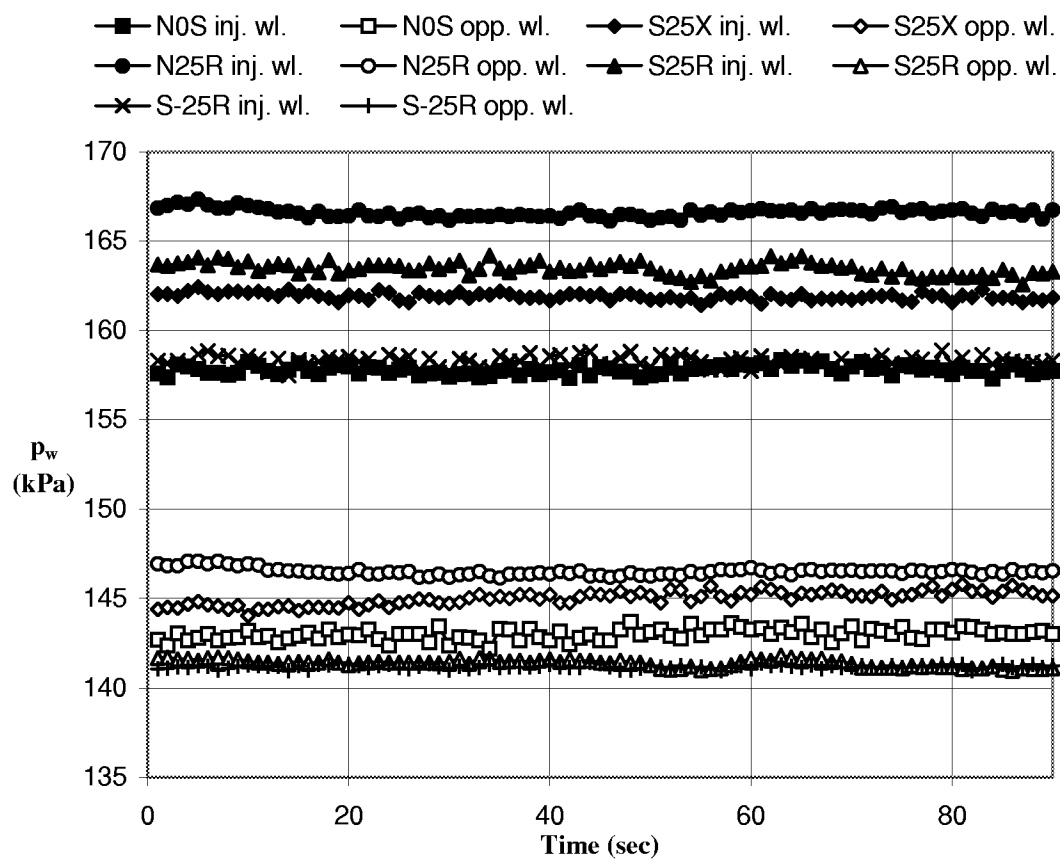
Figure C-3. Time plot of pressures at wall taps near end of duct.

REPORT DOCUMENTATION PAGE		Form Approved OMB No. 0704-0188

1. AGENCY USE ONLY (Leave blank)	2. REPORT DATE December 1999	3. REPORT TYPE AND DATES COVERED Contractor Report

4. TITLE AND SUBTITLE
Effects of Jet Swirl on Mixing of a Light Gas Jet in a Supersonic Airstream

5. FUNDING NUMBERS
NCC1-217
522-51-31-10

6. AUTHOR(S)
Steven E. Doerner
Andrew D. Cutler

7. PERFORMING ORGANIZATION NAME(S) AND ADDRESS(ES)
The George Washington University
Joint Institute for Advancement of Flight Sciences
NASA Langley Research Center
Hampton, VA 23681-2199

8. PERFORMING ORGANIZATION REPORT NUMBER

9. SPONSORING/MONITORING AGENCY NAME(S) AND ADDRESS(ES)

National Aeronautics and Space Administration
Langley Research Center
Hampton, VA 23681-2199

10. SPONSORING/MONITORING AGENCY REPORT NUMBER

NASA/CR-1999-209842

11. SUPPLEMENTARY NOTES
The information submitted in this report was offered as a thesis by the first author in partial fulfillment of the requirements for the Degree of Master of Science, The George Washington University, JIAFS. Langley Technical Monitor: Glenn S. Diskin

12a. DISTRIBUTION/AVAILABILITY STATEMENT
Unclassified-Unlimited
Subject Category 34   Distribution: Nonstandard
Availability: NASA CASI (301) 621-0390

12b. DISTRIBUTION CODE

13. ABSTRACT (Maximum 200 words)

A non reacting experiment was performed to investigate the effects of jet swirl on mixing of a light gas jet in a supersonic airstream. The experiment consisted of two parts. The first part was an investigation of the effects of jet swirl and skew on the mixing and penetration of a 25° supersonic jet injected from a flat surface (flush wall injection) into a supersonic ducted airflow. Specifically, the objective was to determine whether the jet would mix more rapidly if the jet were swirling, and whether swirl, with and without skew, causes the injectant-air plume to have a net circulation (i.e., a single or dominant vortex). The second part was a preliminary study of the mixing of swirling jets injected from the base of a skewed ramp. The hypothesis was that favorable interactions between vorticity generated by the swirling jet and vortices generated by the ramp could produce mixing enhancements. Both parts of the experiment were conducted at equal injectant mass flow rate and total pressure.

14. SUBJECT TERMS
Supersonic mixing, high-speed mixing, jet swirl, mixing enhancement

15. NUMBER OF PAGES
128

16. PRICE CODE
A07

17. SECURITY CLASSIFICATION OF REPORT	18. SECURITY CLASSIFICATION OF THIS PAGE	19. SECURITY CLASSIFICATION OF ABSTRACT	20. LIMITATION OF ABSTRACT
Unclassified	Unclassified	Unclassified	UL